In vivo approach to myelin turnover and oligodendrocyte-dependent axonal integrity

Dissertation

for the award of the degree

"Doctor rerum naturalium" (Dr. rer. nat.)

of the Georg-August-Universität Göttingen

within the doctoral program Molecular Physiology of the Brain

of the Georg-August University School of Science (GAUSS)

submitted by

Katja Lüders

born in

Lüneburg, Germany

Göttingen, June 2018

Thesis committee

PD Dr. Hauke Werner (Reviewer)
Department of Neurogenetics
Max Planck Institute of Experimental Medicine

Prof. Dr. Nils Brose (Reviewer)
Department of Molecular Neurobiology
Max Planck Institute of Experimental Medicine

Prof. Dr. Alexander Flügel
Department of Neuroimmunology
University Medical Center Göttingen
Institute for Multiple Sclerosis Research

Further members of the examination board

Prof. Dr. Michael Hörner
Department of Cellular Neurobiology
Georg-August University, Göttingen

Prof. Dr. Martin Göpfert
Department of Cellular Neurobiology
Schwann-Schleiden Research Centre

Prof. Dr. med. Wolfgang Brück
Department of Neuropathology
University Medical Center Göttingen

Date of the oral examination: 21.08.2018

Declaration

I hereby declare that the Ph.D. thesis entitled "*In vivo* approach to myelin turnover and oligodendrocyte-dependent axonal integrity", has been written independently and with no other sources and aids than quoted.

Göttingen, June 2018

_____

Katja Lüders

Content

Acknowledgements

I would like to thank Prof. Klaus-Armin Nave Ph.D. for giving me the opportunity to work in his department, for scientific discussions and advice. I am deeply grateful to my first referee PD Dr. Hauke Werner for his supervision, for great scientific discussions, for the familial working atmosphere in the AG Werner and for always being there to discuss any kind of questions and ideas. I thank my thesis committee members Prof. Dr. Nils Brose and Prof. Dr. Alexander Flügel for helpful scientific discussions during my thesis committee meetings. I also thank my extended thesis advisory board members, Prof. Dr. Martin Göpfert, Prof. Dr. med. Wolfgang Brück and Prof. Dr. Michael Hörner for their interest in my project and for taking the time to evaluate my thesis. I am aditionally thankful to Prof. Dr. Michael Hörner for coordinating the CMPB doctoral program and for always being approachable for any kind of questions. Likewise, I thank Kirsten Pöhlker, Mandy Fricke, Christin Schröter and Susane Kracke of the GGNB office for their support. I thank Dr. Julia Patzig, who initiated this project together with PD Dr. Hauke Werner and introduced me to a wide array of laboratory techniques as well as theoretical background during my phase as a Master's student. I am very grateful to Ramona Jung, Michelle Erwig, Maria Eichel, Sophie Siems and Tobias Buscham for their support and for making the lab such a joyful place. I am thankful that I had the opportunity to supervise Maria Eichel and Kilian Hinze during their lab rotations and for the work they contributed to this project. I also thank Annette Fahrenholz for doing immunohistochemical stainings. I thank Dr. Kathrin Kusch for scientific discussions, technical advice and for giving me feedback on this manuscript. Likewise, I thank Maria Eichel and Nehal Johri for reading parts of my thesis. My thank also goes to Ursula Kutzke for performing qRT-PCR experiments for my project. I am also very grateful to Dr. Wiebke Möbius, Torben Ruhwedel, Bogusha Sadowski and Martin Meschkat for their fantastic help and support with the electron microscopy facility and especially Dr. Wiebke Möbius for scientific input. I am thankful to the entire department of Neurogenetics for the helpful and inspiring working atmosphere. I also thank Dr. Dilja Krüger-Burg for introducing me to the detection of immunoblotted proteins with the Odyssey system and for sharing antibodies. I am also very thankful to our collaborator Dr. Stefan Nessler from the UMG Göttingen for performing FACS analysis of our mice. All of this research would not have been possible without the animal caretakers, especially Sarah Schulze and Astrid Kanbach, who took care of my mice. I also want to thank Rolf Merker, Hans-Joachim Horn and Lothar Demel for their technical help regarding computer issues and Michaela Schmalstieg and Gabriele Endo for administrative help. I am especially grateful to my parents for supporting me in pursuing the studies and career of my choice. And I thank my husband Stefan Lüders for his love and encouragement, for his sometimes very different and refreshing view on my work and I thank our son Max Konstantin for making the last two years of my life special in a way I could have never imagined and reminding me of the greatest possible gift in life with his smile in the morning, even though this is usually very early.

List of Figures

List of Tables

Abbreviations

APP	Amyloid beta precursor protein
APS	Ammonium persulfate
ATP	Adenosine triphosphate
bp	Base pairs
BSA	Bovine serum albumin
°C	Degrees celsius (centrigrades)
CD	Cluster of differentiation
cDNA	Complementary single stranded DNA
cm	Centimeter
CNP	2'3'-cyclic nucleotide 3' phosphodiesterase
CNS	Central nervous system
Ctrl	Control ($Plp^{flox}*Plp^{CreERT2}$ mice pti)
d	Days
DAB	3,3'-Diaminobenzidine
DAPI	4',6-Diamidin-2-phenylindole
ddH2O	Double distilled (or miliQ) water
DDT	Dithiothreitol
DMEM	Dulbecco's modified eagle's medium
DNA	Deoxyribonucleic acid
dNTP	2'-Desoxyribonucleosid-5'-triphosphate
DPSS	Diode-pumped solid-state
ECL	Enhanced chemiluminescence
EDTA	Ethylenediaminetetraacetic acid
e.g.	Exempli gratia
EM	Electron microscopy
Epon	Epoxy resin
ES cell	Embryonic stem cell
EUCOMM	European conditional mouse mutagenesis program
FA2H	Fatty acid 2-hydroxylase
FACS	Fluorescence-activated cell sorting
FCS	Fetal calf serum
FPKM	Fragments per kilobase of exon per million fragments mapped
g	Standard gravity
GFAP	Glial fibrillary acidic protein
GLUT1	Gluose transporter 1
GJC2	Connexin 47 (CX47)
HBSS	Hank's balanced salt solution
HCl	Hydrochloric acid
HRP	Horseradish peroxidase
HSP	Hereditary spastic paraplegia
IBA1	Allograft-inflammatory factor (AIF1)
i.e.	Id est

Abbreviations

IHC	Immunohistochemistry
iKO	Induced conditional knockout ($Plp^{flox}*Plp^{CreERT2}$ mice pti)
int	Intermediate
i.p.	Intraperitoneal
IPL	Intraperiod line
ISH	*In situ* hybridization
kb	Kilobase
kDa	Kilodalton
M	Molar
MAC3	Lysosomal-associated membrane protein 2 (LAMP2/MAC3)
MBP	Myelin basic protein
MDL	Major dense line
MGB	Modified gitschier buffer
MCT1	monocarboxylate transporter 1
MCT2	monocarboxylate transporter 2
µg	Microgram
µl	Microliter
µm	Micrometer
mg	Milligram
ml	Milliliter
mm	Millimeter
mM	Millimolar
min	Minutes
mo	Months
mRNA	Messenger RNA
NaCl	Sodium chloride
n	Number
ns	Non-significant
nm	Nanometer
NO	Nitric oxide
OL	Oligodentrocyte
o/n	Overnight
OPC	Oligodendrocyte progenitor cell
OsO_4	Osmiumtetroxyde
OSP	Oligodendrocyte-specific protein (CLDN11)
p	P-value
P	Primer
PAGE	Polyacrylamide gel electrophoresis
PBS	Phosphate buffered saline
PCR	Polymerase chain reaction
Pd1	Programmed cell death protein 1 gene
PFA	Paraformaldehyde
pH	Potentia hydrogenii
PLP	Proteolipid protein

PMD	Pelizaeus-Merzbacher disease
pmol	Picomol
PNS	Peripheral nervous system
PVP	Polyvenylpyridilone
pti	Post tamoxifen injection
qRT-PCR	Quantitative real-time PCR
Rag1	Recombination activating protein 1 gene
RIPA	Radioimmunoprecipitation assay buffer
RNA	Ribonucleic acid
ROS	Reactive oxygen species
Rplp0	60S acidic ribosomal protein P0
PVDF	Polyvinylidene difluoride
rpm	Revolutions per minute
Rps13	Ribosomal protein S13
RT	Room temperature
SDS	Sodium dodecyl sulfate
sec	Seconds
SEM	Standard error of the mean
SPG2	Spastic paraplegia type 2
SPG35	Spastic paraplegia type 35
SPG44	Spastic paraplegia type 44
TAE	Trisacetate EDTA buffer
TBS	Tris buffered saline
TBST	Tris buffered saline with Tween-20
TEMED	Tetramethylendiamin
T_{reg}	Regulatory T cell
Ube2l3	Ubiquitin-conjugating enzyme E2 like L3
WT	Wild type
w/v	Weight per volume
UMG	University Medical Center Göttingen
UV	Ultraviolet
V	Volt
v/v	Volume per volume
W	Watt

1. Abstract

Deletion of the most abundant protein of CNS myelin, proteolipid protein (PLP) causes type 2-spastic paraplegia (SPG2) in humans, which is characterized by axonal degeneration. The assumption that the primary cause of SPG2 is the lack of PLP from oligodendrocytes has been challenged by studies reporting *Plp* gene products (official gene name *Plp1*) also in a subset of neurons. To clarify the cellular origin of SPG2, we established mice with a floxed *Plp* allele to selectively delete *Plp* in neurons or oligodendrocytes. Recombination of *Plp* in excitatory projection neurons did not cause neuropathology, whereas oligodendroglial deletion of *Plp* caused the complete neurodegenerative spectrum observed in $Plp^{null/Y}$ mice including axonopathy, gliosis and elevated numbers of T cells in the brain and thus provide a novel model of SPG2. We conclude that the primary cause of SPG2 is the lack of PLP in oligodendrocytes. To better understand the interplay of PLP-deficient oligodendrocytes, axons and T cells, we analyzed the emergence of neuropathological events upon *Plp*-deletion over time in tamoxifen-inducible *Plp* knockout mice. Importantly, axonal spheroids were observed prior to elevated numbers of T cells, implying that axonopathy occurs independent from T cells in this model, at least initially. Together, by analyzing novel mouse models of SPG2 this work provides relevant information about the cellular neuropathology caused by PLP-deficiency.

2. Introduction

The nervous system facilitates complex motor and sensory as well as cognitive functions, it is tightly interconnected with the blood and digestive system and also regulates processes within our body. The nervous system of vertebrates consists of the central nervous system (CNS) comprised of the brain and the spinal cord and the peripheral nervous system (PNS) making up all other nerves in the body. Both CNS and PNS are mainly comprised of neurons, which convey information via electric signals, i.e. action potentials, and glial cells serving diverse functions. Important structural insights into the complex nervous system date back to a bit over 100 years ago. In 1906 Santiago Ramón y Cajal and Camillo Golgi received the Nobel Prize "in recognition of their work on the structure of the nervous system". Using the silver nitrate staining method, developed by Camillo Golgi, Ramón y Cajal observed and illustrated nerve cells as individual entities and proposed that they transmit some sort of information from one to another. Even though it took another approximately 50 years until electron microscopes were developed and could finally prove that neurons are individual cells, as opposed to a continuous mesh as proposed by Golgi and others, this was an essential cornerstone of neuroscience (Lopez-Munoz et al., 2006). Ramón y Cajal's famous drawings of neurons from human and animal brains (**Figure 1**) are of remarkable detail, as demonstrated by comparison with data acquired by more advanced techniques (Garcia-Lopez et al., 2010; Garcia-Marin et al., 2007; Navarrete and Araque, 2014). Using different staining techniques, he also depicted in great detail glial cells of the brain (**Figure 1 b**), which were discovered earlier by Rudolf Virchow in 1846 as reviewed by (Garcia-Marin et al., 2007). Rudolf Virchow initially described "neuroglia" as a connective tissue that binds nervous elements together in 1858 (Parpura et al., 2012) and called in "Nervenkitt" (nerve glue) which gave rise to the name "neuroglia", adapted from the Greek word glia for "glue".
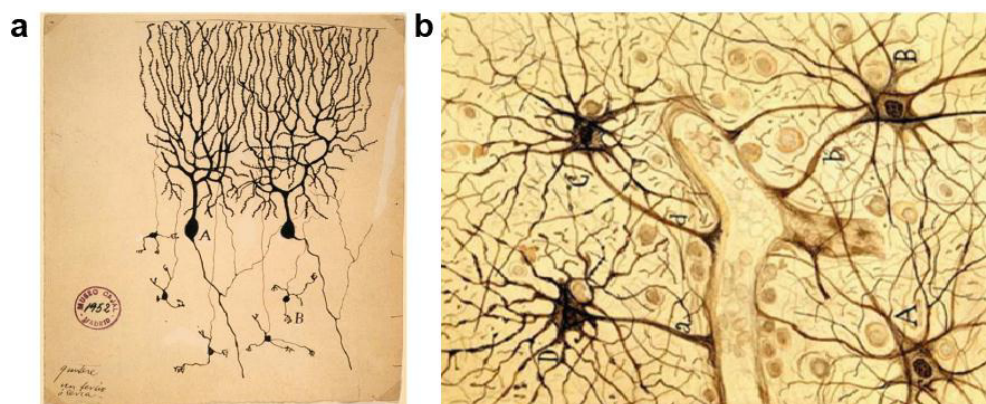
Figure 1: Neurons and glial cells illustrated by Ramón y Cajal
(a) Drawing of Purkinje cells (A) and granule cells (B) from pigeon cerebellum, 1899. Instituto Santiago Ramón y Cajal, Madrid, Spain. **(b)** Drawing of fibrous astrocytes of human cerebral cortex contacting a blood vessel. Instituto Santiago Ramón y Cajal, Madrid, Spain. Figure adapted from (Navarrete and Araque, 2014).

Cajal and others proposed already in the late 19th century that this glia as well is composed of individual cells and that these cells serve functions such as supplying nutrients, regulating transmission of information or making contacts to blood vessels (reviewed by (Garcia-Marin et al., 2007; Navarrete and Araque, 2014)). However, it was only with the advancement of techniques that the complex structures and functions of glial cells could be further elucidated. Today we know that glial cells are not just functioning as a "glue" but serve very diverse functions and are essential for normal performance and modulation of the nervous system. Different kinds of glial cells in the CNS will be introduced in the next paragraph.

2.1. Glial cells in the central nervous system

To properly perform all its complex motor, sensory and cognitive functions, the nervous system of vertebrates requires precise interaction between neurons and glial cells. The long-held belief that glial cells by far outnumber neurons is under current debate (von Bartheld et al., 2016), however it is undoubtable that they are crucial master regulators for normal functioning of the nervous system (Zuchero and Barres, 2015). The three main types of glial cells in the CNS are astrocytes, oligodendrocytes and microglia.

2.1.1. Microglia

Microglia are the resident immune cells in the CNS. They are developed from hematopoetic stem cells and reside in the brain parenchyma. During development, microglia help in sculpting synapses and modulating the strength of synaptic transmission (Colonna and Butovsky, 2017). In response to injury or pathogens they change rapidly in morphology from a ramified "surveillance state" to an amoeboid shaped "activated state". Activated microglia proliferate and migrate to the site of infection or injury, phagocytose and eliminate microbes, dead cells and protein aggregates (Colonna and Butovsky, 2017). Furthermore, microglia secrete pro-inflammatory or anti-inflammatory factors such as cytokines, growth factors and neurotrophic factors. Microglia are typically classified as pro-inflammatory or neurotoxic (M1) or anti-inflammatory (M2) microglia with distinct secretion profiles (Appel et al., 2011). In models of neurodegeneration they often express both neurotoxic and neuroprotective factors (Chiu et al., 2013; Wes et al., 2016). It remains debatable whether microglia have beneficial or protective functions in neurodegeneration and this probably also depends on the context (Colonna and Butovsky, 2017). Recently, activated microglia have also been shown to drive astrocyte reactivity (Liddelow et al., 2017).

2.1.2. Astrocytes

Astrocytes and oligodendrocytes are formed from neuroepithelial progenitor cells in the embryonic neural tube and forebrain during development (Rowitch and Kriegstein, 2010) and are also referred to as macroglia. Astrocytes are the most abundant glial cell type in the CNS and are classified as protoplasmic in the gray matter or fibrous in the white matter. They serve extremely diverse functions in the CNS ranging from promoting neuronal survival, contributing to synaptogenesis and synapse pruning to forming the blood-brain barrier and interacting with the vasculature to provide nutrients to axons (Zuchero and Barres, 2015). They can form a scar upon injury (Anderson et al., 2016), are involved in neurodegenerative diseases (Liddelow and Barres, 2017), have phagocytic potential and can clear debris and dead cells (Tasdemir-Yilmaz and Freeman, 2014). More recently, like microglia, astocytes have been suggested to form at least two types of "reactive" astrocytes upon different types of injury. A1 neuroinflammatory reactive astrocytes are suggested to have "harmful" functions, since they upregulate many genes that have previously been shown to be destructive for synapses; and Ischemia-induced A2 reactive astrocytes might have "helpful" or reparative functions, since neurotrophic factors promoting neuronal survival and growth are upregulated (Liddelow and Barres, 2017).

2.1.3. Oligodendrocytes

Oligodendrocytes are the myelinating cells of the CNS, enabling rapid propagation of action potentials along axons (Waxman, 1980). Oligodendrocytes form myelin by extending processes and wrapping their much extended plasma membrane around the corresponding axon to form a tight multilamellar sheath. At these myelin-ensheathed segments of an axon – the internodes – myelin electrically insulates the axon from the extracellular fluid (**Figure 2**). Thus, electrical currents between axon and extracellular fluid are limited to the nodes of Ranvier, the regions devoid of myelin between the internodes (Hodgkin and Huxley, 1952). Mature myelin may consists of up to 160 membrane layers and internodes in the CNS can extend up to 1.7 mm in length (Nave and Werner, 2014). The regions of the brain and spinal cord which contain a high amount of myelin appear white due to the high lipid content of myelin, and are therefore referred to as white matter. The regions where neuronal cell bodies reside contain less myelin and are referred to as grey matter. While in the CNS the myelin sheath is established by oligodendrocytes, which can form dozens of myelin internodes, myelination in the PNS is provided by Schwann cells, which only form one internode each (Quarles, 2002). Importantly, oligodendrocytes and Schwann cells are not only essential for rapid propagation of action potentials along axons, but also for axonal maintenance (Nave, 2010), further elucidated in chapter 2.3.

Introduction
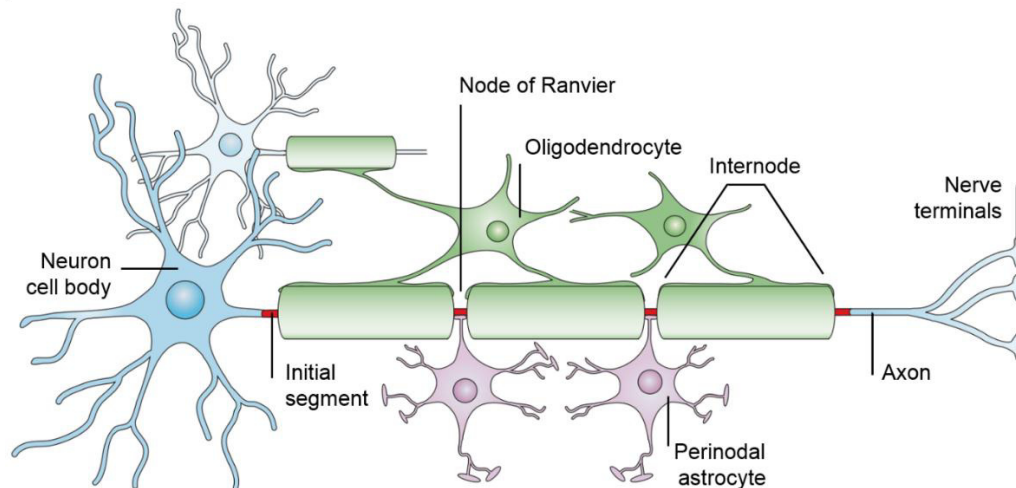
Figure 2: Schematic representation of myelinated axons in the CNS
In the CNS, oligodendrocytes form multiple myelin sheaths by wrapping their extended plasma membrane around internodal axonal segments. Perinodal astrocytes are associated with the nodes of Ranvier. Figure adapted from (Poliak and Peles, 2003).

2.2. Compact and non-compact myelin of oligodendrocytes

By wrapping their much extended plasmamembrane around axons oligodendrocytes form a tight compact multilamellar sheath. On the intracellular side the compacted plasmamembranes are held together by myelin basic protein (MBP) and form a highly electron-dense line, the major dense line (Barkovich, 2000). MBP is a positively-charged, extrinsic membrane protein, which accounts for about 8% of the total protein in CNS myelin (Jahn et al., 2009) and is thereby the second most abundant protein in compact CNS myelin. It exists in four splice isoforms (Boggs, 2006), is essential for the maintenance of compact myelin in the CNS (Weil et al., 2016) and holds the intracellular surfaces of myelin sheaths together by providing adhesion of the negatively-charged cytosolic surfaces with its positive charge (Aggarwal et al., 2013). A less electron dense line - the intraperiod line - represents proteolipid protein (PLP), a transmembrane protein extending into the extracellular space (Barkovich, 2000). PLP is the most abundant protein in CNS compact myelin (Jahn et al., 2009) and exists also in the smaller isoform DM20 (Nave et al., 1987). Since it is the subject of this thesis, it will be further described in chapter 2.4. The oligodendrocyte-specific protein (OSP/Claudin 11) forms strands of tight junctions and thereby the radial component, also providing adhesion in the compact myelin sheath (Gow et al., 1999; Mobius et al., 2008). Besides the compact myelin there are also non-compact compartments of myelin, consisting of adaxonal myelin towards the axon, abaxonal myelin on the outside of the myelin sheath and paranodal loops next to the node of Ranvier. Non-compact myelin is equipped with a partly overlapping, yet different set of proteins compared to compact myelin. Contrary to compact myelin, non-compact myelin domains contain cytoskeletal elements and cytoplasm (Arroyo and Scherer, 2000; Poliak and Peles, 2003).
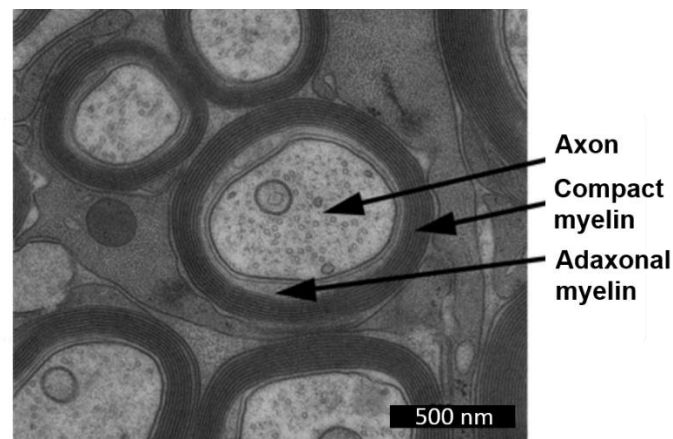
Figure 3: Optic nerve cross section illustrating compact and non-compact myelin in the CNS
Electron micrograph showing a cross section through a high pressure frozen optic nerve of a wild type mouse. Several cross-sectioned myelinated axons can be seen. Arrows indicate an axon, compact myelin and adaxonal non-compact myelin. Figure adapted from (de Monasterio-Schrader et al., 2012).
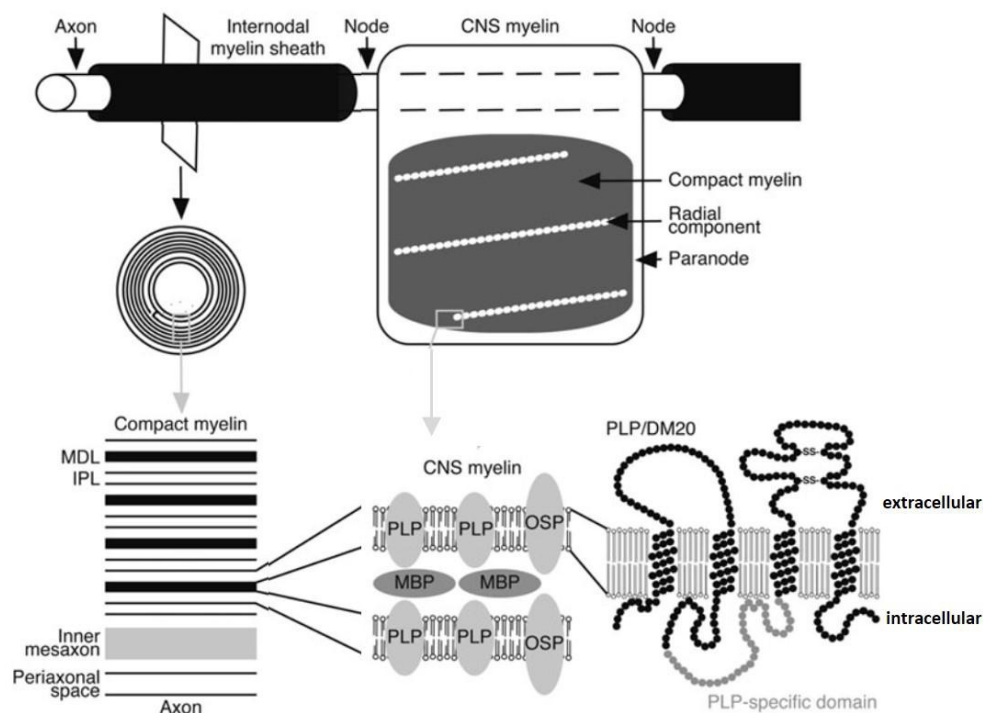
Figure 4: Schematic representation of PLP in compact CNS myelin
On the left, a myelinated axon, a cross section through a myelinated internode and myelin ultrastructure are schematically depicted. In the middle, a myelin internode is unwrapped and illustrates compact myelin in dark grey. Tight junction strands are organized as the radial component. Non-compact myelin, including paranodal non-compact myelin, is depicted in white. In the "enwrapped" state, these segments form paranodal loops. At the bottom, enlargement of the myelin ultrastructure illustrates the major dense line (MDL) and intraperiod lines (IPL). Within the MDL, myelin basic protein (MBP) is associated with the intracellular cytosolic surfaces of the plasma membrane. The intraperiod lines (IPL) are stabilized by the extracellular domains of proteolipid protein (PLP). PLP is composed of 276 amino acids and contains four transmembrane domains and two extracellular loops. Its smaller isoform DM20 lacks 35 amino acids in the intracellular loop, depicted in grey. Another major structural compact myelin protein is the oligodendrocyte-specific protein (OSP/CLDN11), which forms the radial component. Figure adapted from (Mobius et al., 2008).

2.3. Oligodendroglial support for axons

Oligodendrocytes support not only axonal function by forming myelin sheaths to increase the speed of action potential propagation, but they are also essential for axonal integrity. A number of myelin-related diseases, such as multiple sclerosis, or leukodystrophies illustrate that the lack of myelin is detrimental. But oligodendrocytes also provide axonal support in a myelin-independent manner. The first hint that oligodendrocytes may provide axonal support in a myelin-independent manner came from the $Plp^{null/Y}$ mouse (Klugmann et al., 1997), a model for spastic paraplegia type 2 (SPG2) (Garbern et al., 2002). Surprisingly at that time, $Plp^{null/Y}$ mice form relatively normal appearing compact myelin, despite lacking the most abundant compact myelin protein in the CNS. However, they do display progressive axonopathy, i.e. axonal spheroids, also referred to as axonal swellings, and axonal loss (Griffiths et al., 1998) and develop impaired motor capacity by 15-16 months of age (Griffiths et al., 1998; Groh et al., 2016), indicating that oligodendrocytes exert a myelin-independent function for axonal integrity. Further support for this concept comes from a mouse model lacking the non-compact myelin protein 2',3' cyclic nucleotide 3'-phosphodiesterase (CNP). Also Cnp^{null} mice display axonal spheroids, despite the formation of compact myelin (Lappe-Siefke et al., 2003) and are even more affected than $Plp^{null/Y}$ mice. They display axonal spheroids in the optic nerve as early as postnatal day 15, whereas they are observed at around postnatal day 40 in $Plp^{null/Y}$ mice (Edgar et al., 2004b). In Cnp^{null} mice the progressive axonopathy results in premature death at around 7 to 11 months of age (Lappe-Siefke et al., 2003) whereas life expectancy of $Plp^{null/Y}$ mice is not impaired up to at least 1 year of age (Patzig et al., 2016b) and $Plp^{null/Y}$ mice have even been analyzed with an the age of 22 months (Griffiths et al., 1998). Importantly, PLP and CNP are not essential for the formation of compact myelin but for axonal integrity. In contrast, a mouse model devoid of compact myelin due to the lack of the second most abundant compact myelin protein MBP displays no axonal degeneration. (Rosenbluth, 1980). In these so-called "shiverer" mice axons are however ensheathed by oligodendrocytes which do not form compact myelin sheaths, suggesting that the supportive role for axonal integrity comes from oligodendrocytes, independently of the formation of compact myelin sheaths. Up until now it is uncertain how exactly oligodendrocytes support axonal integrity. Current studies suggest a metabolic support of oligodendrocytes for axons (Funfschilling et al., 2012; Lee et al., 2012; Nave, 2010).

2.4. Proteolipid protein (PLP)

PLP is the most abundant protein in the compact myelin of the CNS. It accounts for about 17% of the total protein in CNS (Jahn et al., 2009) and is thereby the most abundant CNS myelin protein. PLP is a hydrophobic 30 kDa four-transmembrane domain spanning protein (tetra-span membrane protein) with its N and C terminal located in the cytoplasm (Popot et al., 1991). The highly basic regions of PLP

interacts with lipids (Weimbs and Stoffel, 1992), especially cholesterol and galactosylceramide-enriched membrane domains (Simons et al., 2000), which are major components of the myelin membrane. The *Plp* gene is localized on the long arm of the X chromosome. It spans a roughly 17-kb genomic interval, is comprised of 7 exons (Macklin et al., 1987) and generates two splice isoforms. The larger isoform PLP is comprised of 276 amino acids and has a molecular weight of 30 kDa (Nave et al., 1987). The smaller splice isoform DM20 (26.5 kDa) is formed due to an alternative splice site in exon 3 and lacks 35 amino acids in the intracellular loop (Nave et al., 1987). The sequences of PLP and DM20 are highly conserved across species and the amino acid sequences are identical in man, mouse and rat (Macklin et al., 1987; Woodward, 2008). PLP is synthesized in the rough endoplasmic reticulum and then transported via the secretory pathway through the Golgi. In the Golgi, PLP associates and forms membrane "rafts" with myelin lipid constituents, such as cholesterol, galactocerebroside or sulfatide, which are then transported in vesicles into the myelin (Simons et al., 2000). *Plp* expression is already observed in oligodendrocyte progenitor cells (OPC) during embryonic development (Delaunay et al., 2008).

2.5. Human disorders caused by mutations affecting the *PLP* gene

Mutations in the *PLP* gene (official gene name *PLP1*) lead to the leukodystrophy Pelizaeus-Merzbacher disease (PMD) and the clinically distinct spastic paraplegia type 2 (SPG2) (Inoue, 2005; Mayer et al., 2015; Saugier-Veber et al., 1994; Seitelberger, 1995; Woodward, 2008). Both PMD and SPG2 are inherited in an X-linked recessive fashion and thus usually affect only men (Brender et al., 2015; Woodward, 2008). While axons degenerate without apparent impairment of myelin in SPG2 patients and corresponding models (Garbern et al., 2002; Klugmann et al., 1997), axonal degeneration in PMD is accompanied by dysmyelination (i.e. myelin is not formed properly during development), demyelination and oligodendrocyte death (Woodward, 2008).

2.5.1. Pelizaeus-Merzbacher disease (PMD)

At least 100 different mutations of the *PLP* gene can result in PMD (Woodward, 2008). The severity of symptoms is heterogenous. It correlates with the degree of myelination defects and depends on the type of mutation (Duncan, 2005). Based on the severity PMD is categorized into two forms. The *classic* form of PMD, which accounts for most cases of PMD, results from genomic duplications in chromosome Xq22 which contains the *PLP* gene (Woodward, 2008). Symptoms such as hypotonia (low muscle tone) or nystagmus (involuntary eye movements) usually appear within the first year of life. They are followed by motor disabilities such as spasticity of upper and lower limbs, ataxia, as well as spasticity and slow development, leading to death

around mid-adult life (Inoue, 2005; Marteyn and Baron-Van Evercooren, 2016). In contrast to the *classic* form, the more severe *connatal* form is mostly caused by point mutations of *PLP* (or triplications or quintuplications of the *PLP* gene). It usually presents shortly after birth, comes with severe neurological symptoms and more severe motor deficits, exemplified by feeding and breathing issues, spasticity and seizures and leads to death within the first decade of life (Marteyn and Baron-Van Evercooren, 2016; Woodward, 2008). Furthermore, *transitional* forms of PMD combine clinical features of the *classical* and *connatal* forms (Garbern, 2007). As investigated in mouse models, *Plp* overexpression results in accumulation of PLP in the late endosome/lysosome with cholesterol (Simons et al., 2002), which is believed to interfere with myelination and reduce viability of the oligodendrocyte. Missense mutations of *Plp* probably lead to misfolding and accumulation in the rough endoplasmic reticulum, resulting in failure of transport to the oligodendrocyte cell membrane and activation of the unfolded protein response (Duncan, 2005; Garbern, 2007; Inoue, 2017; McLaughlin et al., 2007; Woodward, 2008).

2.5.2. Spastic paraplegia type 2 (SPG2)

SPG2 is caused by deletion of *PLP* and presents milder symptoms than the *classic* and *connatal* PMD. It is often referred to as "mild form of PMD" or as an allelic disease to PMD (Woodward, 2008). In contrast to other PMD forms however SPG2 is clinically different. In SPG2 there is no hypomyelination and axons degenerate despite relatively normal myelin. With its clinical presentation – degeneration of upper motor neurons – SPG2 caused by deletion of *PLP* is a form of hereditary spastic paraplegia, which are described in the next paragraph.
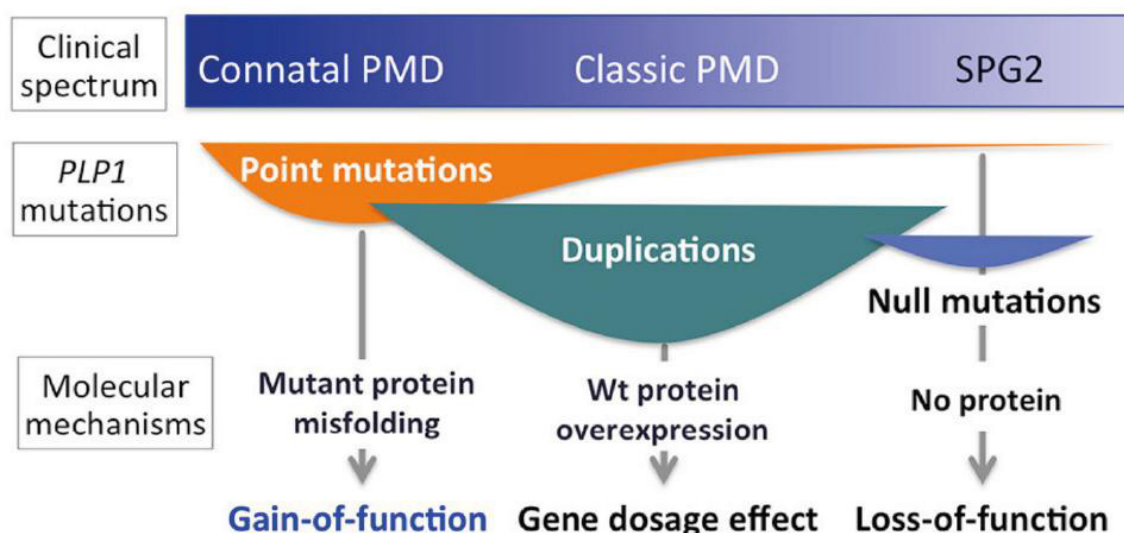
Figure 5: Classification of PLP-related inherited disorders
Clinically, PLP-related inherited disorders are classified into *connatal* PMD and *classic* PMD, which both display hypomyelination and a wide variety of clinical phenotypes, and the clinically more distinct SPG2. Each class of mutations results in a range of phenotypes. Point mutations leading to protein misfolding and toxic gain of function are the most prominent cause for the most severe *connatal* PMD. *PLP* duplications are the most frequent cause for *classic* PMD and lead to a toxic gene dosage effect. SPG2 is associated with the loss of PLP. Figure taken from (Inoue, 2017).

2.6. Hereditary spastic paraplegia (HSP)

Hereditary spastic paraplegia (HSP) is a heterogenous group of inherited neurological diseases characterized by lower extremity spasticity and weakness. The prevalence of HSP has been estimated to be between 3 and 10 cases per 100000 in Europe (Salinas et al., 2008). At least 41 different mutated genes (Fink, 2013) can cause different types of HSP. The unifying clinical feature is the length-dependent retrograde degeneration of the long descending axons of upper motor neurons in the cerebrospinal tract (Salinas et al., 2008). Their degeneration results in spasticity and weakness in the lower limbs, abnormal walking which may cause patients to become wheelchair-bound, often bladder dysfunction and sometimes sensory symptoms (such as reduced vibration sense) or pes cavus (Salinas et al., 2008). However, symptoms can vary in degree, onset and progression, depending on the underlying mutation and potentially also on environmental factors (Fink, 2013). Symptoms of HSP may begin at any age, from early childhood through senescence; life expectancy is normal in most cases (Fink, 2013). The pure form of HSP comprises the symptoms described above, complex HSP forms involves additional neurologic symptoms such as ataxia, epilepsy, deafness, mental retardation, cognitive decline and polyneuropathy (Fjermestad et al., 2016; Salinas et al., 2008). Besides dividing HSP types into pure and complex forms by their clinical representation, HSP are also divided according to the mode of inheritance. Most HSP cases (70%) are inherited in an autosomal dominant fashion and mostly these are pure cases. Complicated forms represent usually autosomal recessive or X-linked recessive forms of HSP. SPG2

caused by the lack of PLP is an X-linked recessive and complex form of HSP. Especially complicated and late-onset forms are often difficult to diagnose and easily mistaken for other conditions such as multiple sclerosis, motor neuron disease or vitamin deficiency to name a few (Salinas et al., 2008).

A health survey of HSP patients reported lower mental wellbeing, lower social support, poorer memory and sleep and overall lower life satisfaction (Fjermestad et al., 2016). To date there is no treatment to prevent, slow or reverse HSP including SPG2. Current treatments such as physiotherapy or prescription of muscle relaxants, such as Baclofen, only address the symptoms of the disease. Better understanding of the underlying disease mechanisms may help to find better treatment options.

2.7. The function of PLP is not understood

Different mutations of the *PLP* gene lead to forms of PMD or SPG2, however the exact roles of PLP are not yet understood. PLP is dispensable for development and survival of oligodendrocytes (Yool et al., 2001). It is also not essential for the formation of compact myelin (Klugmann et al., 1997). In the absence of PLP a proportion of small diameter axons are ensheathed but show no or delayed formation of myelin sheaths, suggesting that PLP may be involved in early stages of axon-oligodendrocyte interaction and wrapping of the axon. (Yool et al., 2001). The rate of myelin biogenesis was shown to be impaired due to depletion of PLP (de Monasterio-Schrader et al., 2013). Despite being largely dispensable for the formation of compact myelin sheaths, PLP has been suggested to harbor adhesive properties and be involved in stabilizing the myelin sheath (Klugmann et al., 1997). Ultrastructural abnormalities of myelin including changes of the intraperiod line and myelin outfoldings have been observed upon depletion of PLP (Duncan et al., 1987; Klugmann et al., 1997; Mobius et al., 2016; Patzig et al., 2016a) and it may be involved in organization of the radial component (Rosenbluth et al., 2006). In early stages of development PLP may play a role in the development of OPCs, since it is detectable long before myelin formation begins (Delaunay et al., 2008; Inoue, 2005). Indeed PLP-deficiency results in subtle changes in glutamate-dependent migration of oligodendrocyte progenitor cells (Harlow et al., 2015). Moreover, PLP is required for the incorporation of cholesterol (Werner et al., 2013) and the deacetylase sirtuin 2 (Werner et al., 2007) into the CNS myelin sheath. Yet it is unclear if and how any of these implications lead to axonopathy in $Plp^{null/Y}$ mice and SPG2 patients.

2.8. Axonopathy in $Plp^{null/Y}$ mice modeling SPG2

The most prominent neuropathological feature of PLP-deficient ($Plp^{null/Y}$) mice are axonal spheroids and progressive degeneration of axons particularly in long myelinated tracts (Griffiths et al., 1998), making them a genuine model of SPG2

caused by loss-of-function mutations (Garbern et al., 2002; Griffiths et al., 1998). Since myelin of $Plp^{null/Y}$ mice appeared surprisingly relatively normal (Klugmann et al., 1997) this model also suggested for the first time a myelin-independent role of oligodendrocytes for axonal support (chapter 2.3.). A similar mouse model with significant residual CNS myelination is the $Plp^{rumpshaker/Y}$ mouse (Edgar et al., 2004a; Schneider et al., 1992), defined by the same I186T missense mutation as the first human family diagnosed with SPG2 (Saugier-Veber et al., 1994). Axonal spheroids are apparent in optic nerves of $Plp^{null/Y}$ mice from about postnatal day 40 (Edgar et al., 2004a). They result from accumulations of membranous organelles and occur mainly in small caliber axons (Edgar et al., 2004a; Griffiths et al., 1998), preferentially at the distal juxtaparanode, the region between the internode and the node (Edgar et al., 2004a). Axonal spheroids are probably caused by an impaired retrograde axonal transport, described in $Plp^{null/Y}$ mice (Edgar et al., 2004a) and impairment of axonal transport is also considered a putative common factor in the pathogenesis of HSP (Crosby and Proukakis, 2002). Mechanistically, it is not yet clear how axonal pathology emerges in $Plp^{null/Y}$ mice and SPG2 patients. Besides the concept that metabolic support by oligodendrocytes (Funfschilling et al., 2012; Lee et al., 2012; Nave, 2010) may be disturbed, there are two alternative hypotheses how axonal degeneration might evolve in $Plp^{null/Y}$ mice and these provide the motivation for our study.

2.9. Does neuroinflammation cause axonal degeneration in $Plp^{null/Y}$ mice?

The full spectrum of neuroinflammation, including microgliosis, and astrogliosis and elevated numbers of T cells, is observed in models for PMD (Groh et al., 2016; Ip et al., 2006; Ip et al., 2012) and in the SPG2-modeling $Plp^{null/Y}$ mouse (de Monasterio-Schrader et al., 2013). T cells have recently been reported to aggravate neurodegeneration in the $Plp^{transgenic-overexpressor}$ mouse model of PMD and the $Plp^{null/Y}*PLP^{L30R}$ and $Plp^{null/Y}*PLP^{R137W}$ transgenic mouse models of PMD caused by missense mutations (Groh et al., 2016; Ip et al., 2006; Ip et al., 2012). Furthermore, it has been proposed that T cells perturb retrograde axonal transport in a PMD mouse model (Ip et al., 2012). The involvement of neuroinflammation has been considered to be underestimated in PMD pathology (Marteyn and Baron-Van Evercooren, 2016) and it has been proposed that "since at least some forms of HSP might be strongly driven by neuroinflammation, it is now tempting to consider immune modulation as a treatment option … for so far non-treatable, genetically-mediated disorders of the nervous system accompanied by pathogenic neuroinflammation" (Groh et al., 2016). Since oligodendrocytes can play an active part in pathological cascades and may modulate immune cells (Zeis et al., 2016), one may hypothesize that not a lack of oligodendroglial support, but oligodendrocyte-mediated recruitment of T cells may ultimately damage axons in $Plp^{null/Y}$ mice.

2.10. Does pathology in *Plp*^{null/Y} mice arise due to lack of PLP in oligodendrocytes or neurons?

For the vast majority of HSP types, neuronal dysfunction is thought to be the primary pathologic cause in patients and respective mouse models. Affected genes are thought to mainly impair transport of macromolecules and organelles, disturbance of mitochondrial function, or lead to abnormalities of the developing axon (Salinas et al., 2008). In this respect SPG2 is an exception, together with two other types of spastic paraplegia, SPG35 and SPG44, which are caused by mutations in the genes for fatty acid 2-hydroxylase (FA2H) and connexin 47 (GJC2/CX47), respectively (Dick et al., 2008; Orthmann-Murphy et al., 2009). The expression of these three genes is strongly enriched in oligodendrocytes compared to other neural cell types – see **Figure 9** (Zhang et al., 2014) – and it is unknown how exactly dysfunctional oligodendrocytes may lead to neurodegeneration. Given that neurodegeneration in all other types of HSP is likely caused by intrinsic defects within neurons – pathogenic mechanisms reviewed in (Blackstone et al., 2011; Salinas et al., 2008) – it is an intuitive question to ask if there is not at least some expression of these genes in neurons, so that actually impairment of neuronal expression may lead to neurodegeneration.

2.11. *Plp* expression in neurons

Due to its strong expression in oligodendrocytes it is generally assumed that neuropathological impairments in SPG2, including axonal pathology, are caused by the lack of PLP from oligodendrocytes. However, over the last two decades there has indeed been accumulating evidence that *Plp* is not only expressed in oligodendrocytes but also in neurons. *Plp* gene expression has first been observed in neuronal cell lines of mouse and rat (Ikenaka et al., 1992). Also in other studies neuronal activity of the *PLP*/*Plp* gene has been documented, for example by using reporter gene expression in transgenic mice, *Plp* mRNA *in situ* hybridization, PLP/DM20 immunolabeling and by transcriptional and translational profiling – examples in **Figure 6, 7, 8, 9**; see overview in **Table 1** from (Luders et al., 2017) and references therein. Direct proof that the lack of PLP in oligodendrocytes is responsible for neuropathological impairments in SPG2 and PMD is lacking, since all previous *in vivo* analyses were performed in mice lacking PLP from all cells. Together, the above-mentioned and other publications showing that *Plp* expression is not exclusive to oligodendrocytes (**Table 1**) have led to the alternative hypothesis that the absence of neuronal *Plp* expression causes the axonal degeneration phenotype in SPG2 patients and the respective mouse models (Fulton et al., 2011; Jacobs et al., 2003; Sarret et al., 2010). The hypothesis has been posed that "neuronal expression of the *hPLP1* gene might explain the neuronal dysfunctions in patients carrying *hPLP1* gene mutations" (Sarret et al., 2010). (*hPLP1* stands for human *PLP1* gene).
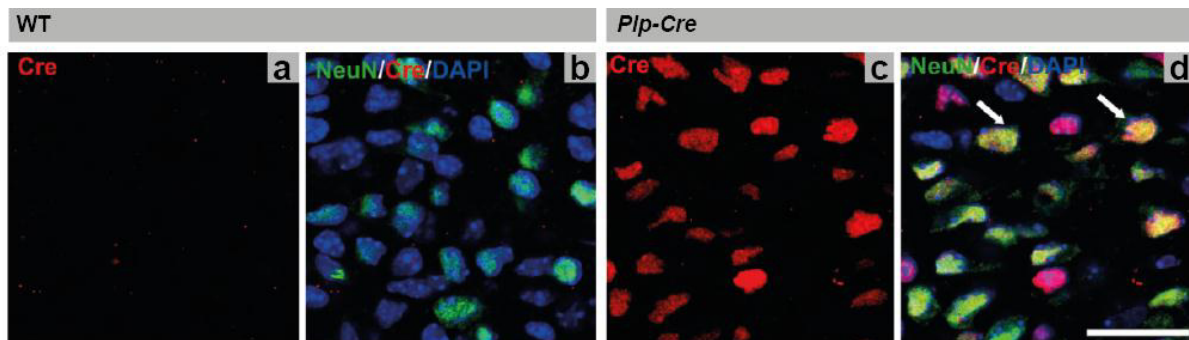
Figure 6: *Plp* promoter activity in neurons
Deep cerebellar white matter region from wild type mice **(a, b)** and *Plp-Cre* line 627 mice **(c, d)** at postnatal day 4 double stained with antibody for Cre (red) as a marker for *Plp* expression and NeuN (green) as a marker for neurons and counterstained with DAPI. Many Cre-positive cells co-stained for NeuN (indicated by white arrows). Scale bar 20 µm. Figure adapted from (Michalski et al., 2011).
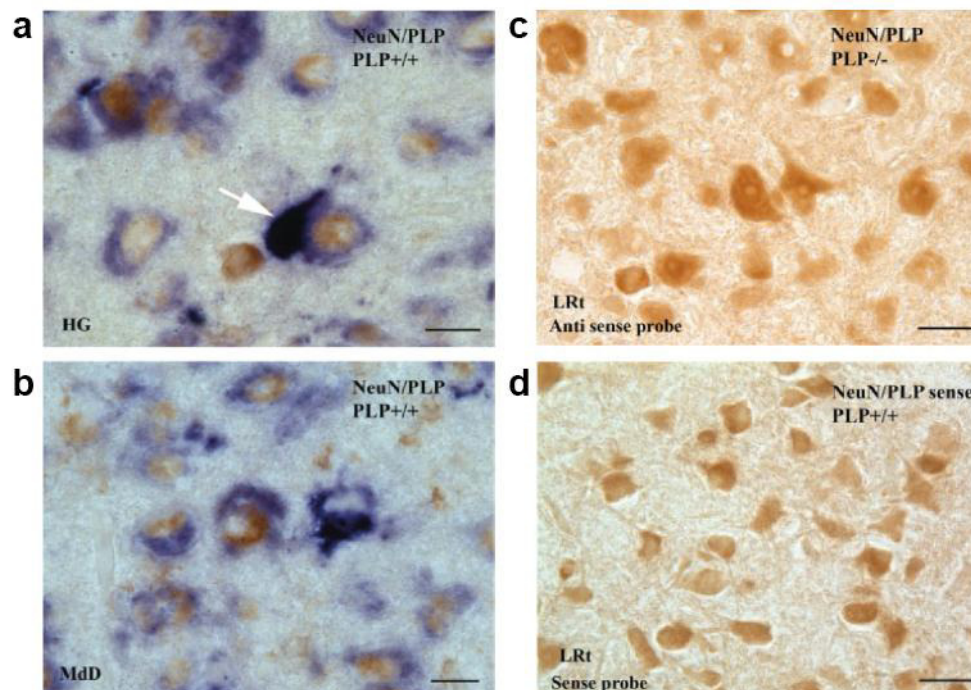
Figure 7: *In situ* hybridization of *Plp* mRNA
In situ hybridization for *Plp* mRNA (blue)-labeled neurons and oligodendrocytes in the caudal medulla of a mouse at postnatal day 5. Neurons are colabeled with NeuN (brown). **(a, b)** Examples from hypoglossal nucleus (HG) and medullary reticular nucleus, dorsal part (MdD). White arrow indicates an oligodendrocyte (dark blue) apposed to a neuron (light blue cytoplasm, NeuN-positive nucleus). No signal was detected in the $Plp^{null/Y}$ mouse **(c)** or by using a sense probe **(d)** in the lateral reticular tract (LRt). Scale bar=15 µm in a and b; Scale bar 24 µm in c and d. Figure adapted from (Miller et al., 2009).
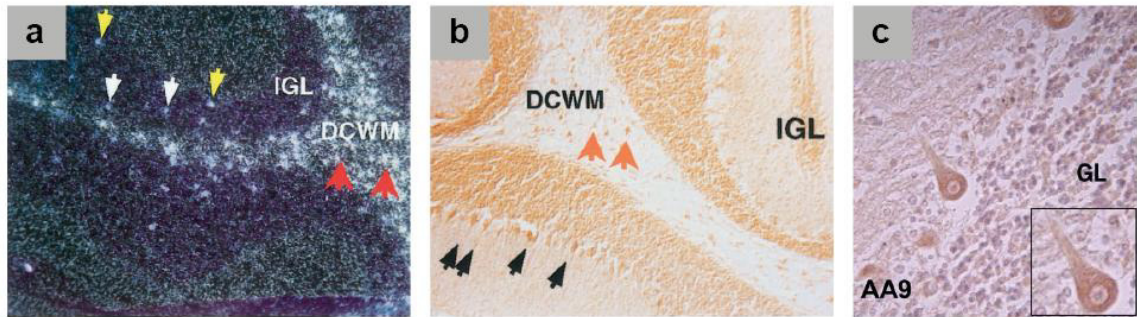
Figure 8: *In situ* hybridization of *Plp* mRNA and immunohistochemical detection of PLP protein
(a) *In situ* hybridization in the cerebellum of 14-days-old mice shows punctate labeling of the "sr" variants of *Plp* and *Dm20* mRNAs in cells throughout the white matter (red arrows) and the internal granular cell layer (neurons; white arrows) and Purkinje cells (neurons; yellow arrows). **(b)** Immunohistochemical detection of srPLP and srDM20 in a region of the cerebellum similar to that in **(a)**. Cell bodies of oligodendrocytes (red arrows) and Purkinje cells (black arrows) are indicated. Granule neurons located within the internal granular layer were also immunostained. **(c)** Neuronal expression of PLP protein in adult human CNS tissue. The box indicates a Purkinje cell. IGL=internal granular layer; DCWM=deep cerebellar white matter; GL=granular layer; AA9=Antibody used to detect PLP. Figure **8 a, b** adapted from (Bongarzone et al., 1999). Figure **8 c** adapted from (Sarret et al., 2010).

Table 1: Previous studies reporting the detection of *PLP/Plp* gene products in neurons

Detection level	Technique	Species	Reference
mRNA	PCR on neuronal cell lines	Rat, mouse	Ikenaka, Kagawa, & Mikoshiba (1992)
mRNA, protein	RPA, RT-PCR, ISH, IHC	Mouse	Bongarzone et al. (1999)
Protein, gene activity	IHC; Plp^{EGFP} reporter line	Myelin deficient (md) rat, mouse	Miller et al. (2003)
Protein	IHC	Mouse	Jacobs et al. (2003)
Gene activity	Plp^{EGFP} BAC (gensat.org)	Mouse	Gong et al., (2003)
Protein	IHC	Mouse	Jacobs, Bongarzone, Campagnoni, & Campagnoni (2004)
Protein	IHC ('PLP-like epitopes')	Mouse, cow, owl, frog, cichlid, shark	Greenfield et al. (2006)
mRNA	ISH (mouse.brain-map.org)	Mouse	Lein et al. (2007)
Translated mRNA	Various neuronal BAC tg lines, TRAP	Mouse	Doyle et al. (2008)
Enhancer activity	Plp$^{EGFP-lacZ}$ reporter line	Mouse	Tuason et al. (2008)
Gene activity, mRNA, protein	Plp^{EGFP} reporter line, ISH, IHC	Mouse	Miller, Kangas, & Macklin (2009)
mRNA, protein	ISH, IHC	Human	Sarret et al. (2010)
Gene activity, protein	Plp^{EGFP} reporter line, IHC, Patch clamp	Mouse	Fulton et al. (2011)
Gene activity	Plp^{Cre} crossed with reporter lines, IHC, X-Gal	Mouse	Michalski, Anderson, Beauvais, De Repentigny, & Kothary (2011)
mRNA	Immunopanning, RNA-Seq (web.stanford.edu/group/barres_lab/brain_rnaseq.html)	Mouse	Zhang et al. (2014)
mRNA	Single cell RNA-Seq (linnarssonlab.org/cortex)	Mouse	Zeisel et al. (2015)

Given are detection level, method and species. BAC, bacterial artificial chromosome; FACS, Fluorescence-activated cell sorting; IHC, immunohistochemistry; ISH, *in situ* hybridization; PCR, polymerase chain reaction; RT-PCR, reverse transcription PCR; RNA-Seq, whole-transcriptome shotgun sequencing; RPA, ribonuclease protection assay; TRAP, translating ribosome affinity purification. Table taken from (Luders et al., 2017).

References in **Table 1**: (Bongarzone et al., 1999; Doyle et al., 2008; Fulton et al., 2011; Gong et al., 2003; Greenfield et al., 2006; Ikenaka et al., 1992; Jacobs et al., 2004; Jacobs et al., 2003; Lein et al., 2007; Michalski et al., 2011; Miller et al., 2003; Miller et al., 2009; Sarret et al., 2010; Tuason et al., 2008; Zeisel et al., 2015; Zhang et al., 2014)

3. Aim of this thesis

It is generally assumed that neuropathology in SPG2 is caused by a lack of PLP from oligodendrocytes. Given that *Plp* gene activity, *Plp* mRNA and PLP protein have been detected in neurons, the hypothesis emerged that the pathology in SPG2 and respective mouse models might actually be caused by a lack of PLP in neurons. One aim of this thesis is to test this hypothesis by establishing mouse models allowing cell-type specific recombination of a floxed *Plp* allele in neurons or oligodendrocytes. The respective mutants will be subjected to neuropathological analysis to test whether neuropathology emerges as a consequence of neuronal or oligodendroglial *Plp*-deletion. Furthermore time-controlled deletion of *Plp* will be used in a tamoxifen-inducible model to analyze in which order axonal spheroids, gliosis and elevated number of T cells emerge. This shall help to elucidate whether infiltration of T cells is required for axonal damage in PLP-depleted mice or whether it is a secondary effect.

4. Material

4.1. Chemicals and kits

Chemicals and laboratory materials

All chemicals were purchased from Sigma-Aldrich GmbH (Munich, Germany), Merck KGaA (Darmstadt, Germany) and SERVA (Heidelberg, Germany) unless stated otherwise. General laboratory materials were from BD Falcon (Heidelberg, Germany), Bio-Rad (Munich, Germany), Brand (Radebeul, Germany), Gilson (Limburg-Offheim, Germany) and Eppendorf (Hamburg, Germany).

Kits

RNA purification 'RNeasy mini prep'	Qiagen (Portland, USA)
DC Protein Assay (Lowry et al.)	Bio-Rad (Munich, Germany)
LSAB$_2$ kit	Dako (Hamburg, Germany)
Vector Elite ABC kit	Vector Labs (Loerrach, Germany)
DAB Zytomed kit	Zytomed Systems GmbH (Berlin, Germany)
FoxP3 staining kit	eBioscience; Thermo Fisher Scientific (Frankfurt, Germany)

4.2. Molecular biology

Modified Gitschier buffer (MGB)

67 mM	Tris/HCl, pH 8.8
16.6 mM	$(NH_4)_2SO_4$
6.5 mM	$MgCl_2$
0.5% [v/v]	Triton X-100

Proteinase K (10 mg/ml)

Added to MGB buffer before use for tail digest
Final concentration 1 mg/ml

10 mM dNTP (50 x stock)

2.5 mM each nucleotide (dATP, dCTP, dGTP, dTTP) (Boehringer-Ingelheim, Germany)
200 µM final concentration in a PCR reaction (50 µM each nucleotide)

50 x Trisacetate EDTA (Towbin et al.) buffer

2.0 M	Tris/Acetate, pH 8.0
50 mM	EDTA
17.5% [v/v]	Glacial acetic acid

Material

Enzymes

Proteinase K	Boehringer GmbH (Mannheim, Germany)
GOTaq DNA polymerase	Promega (Mannheim, Germany)
Superscript III-reverse transcriptase	Invitrogen (Karlsruhe, Germany)

DNA marker

GeneRuler 100 bp DNA ladder	Thermo Fisher Scientific (St. Leon-rot, Germany)

4.3. Protein biochemistry buffers

10 x Phosphate buffered saline (PBS)

1.7 M	NaCl
34 mM	KCl
40 mM	$Na_2HPO_4 \times 2H_2O$
18 mM	K_2HPO_4
pH 7.2 with 1 N NaOH	

10 x Tris-buffered saline (TBS)

500 mM	Tris/HCl, pH 7.5
1.5 M	NaCl

2 x Modified RIPA buffer (Protein lysis buffer)

200 mM	Tris/HCl pH 7.5
600 mM	NaCl
2 mM	EDTA
2% [w/v]	Triton X-100
1% [v/v]	SDS

Complete Mini protease inhibitor (Roche Diagnostics GmbH, Mannheim, Germany) was freshly added to RIPA buffer before use (1 tablet/10 ml).

4.4. SDS PAGE and immunoblot

SDS separating gel

12% or 10% [v/v]	Acrylamid/Bisacrylamid 29:1
0.4 M	Tris/HCl pH 8.8
0.1% [v/v]	SDS
0.03% [v/v]	APS
0.08% [v/v]	TEMED

SDS stacking gel

4% [v/v]	Acrylamid/Bisacrylamid 29:1
125 mM	Tris/HCl pH 6.8
0.1% [v/v]	SDS
0.05% [v/v]	APS
0.1% [v/v]	TEMED

4 x SDS sample buffer

40% [v/v]	Glycerol
240 mM	Tris/HCl pH 6.8
8% [v/v]	SDS
0.04% [w/v]	Bromphenol blue

10 x SDS running buffer (Laemmli buffer)

250 mM	Tris base
1.92 M	Glycine
1% [v/v]	SDS

Transfer buffer

96 mM	Tris base
78 mM	Glycine
10% [v/v]	Methanol

20 x Tris buffered saline (TBS)

1 M	Tris/HCl, pH 7.5
3 M	NaCl

1 x TBS with Tween-20 (TBST)

50 mM	Tris/HCl, pH 7.5
150 mM	NaCl
0.05% [v/v]	Tween-20

Immunoblot blocking buffer for detection with Intas ChemoCam system
5% [w/v] non-fat dry Milk powder in 1 x TBST

Immunoblot blocking buffer for detection with Odyssey infrared imager
50% Odyssey®Blocking buffer (PBS) in TBST (LI-COR, Lincoln, NE)

Protein marker
PageRuler Plus Prestained Protein Ladder 10-250 K (Fermentas, St. Leon-Rot, Germany)

Material

Additional materials

Enhanced Chemiluminescence (ECL) Immunoblot detection kit Western Lightning™ Plus-ECL, Enhanced luminol reagent plus (Perkin Elmer Life Sciences, Inc., Rodgau, Germany)
ECL-Hyperfilms (Amersham Biosciences, Uppsala, Sweden)
PVDF membrane Hybond P pore size 0.45 µm (Amersham, Arlington Heights, IL)

4.5. Solutions for fixation

Avertin
2% [w/v]   2,2,2-Tribromethanol 99%
2% [v/v]   Amylalkohol
Mixed at 40°C for 30 min while stirring and subsequently filtered
Stored at -20°C

16% [w/v] Paraformaldehyde (PFA)
16% [w/v] Paraformaldehyde cooked at 65°C for 20 min while stirring.
5 N NaOH droplets added until solution was cleared, filled up to final volume of 500 ml with ddH$_2$O and then filtered.
Aliquoted and frozen at -20°C

0.2 M Phosphate buffer (fixation buffer)
0.36% [w/v]   Sodium dihydrogen phosphate (NaH$_2$PO$_4$)
3.1% [w/v]   di-Sodium hydrogen phosphate (Na$_2$HPO$_4$)
1% [w/v]   Sodium chloride

4% Paraformaldehye (PFA, immunohistochemistry)
4% [w/v]   PFA
0.1 M   Phosphate buffer

Immuno Karlsson-Schultz fixative (for immuno electron microscopy)
4% [w/v]   PFA
0.25% [w/v]   Glutaraldehyde
0.1 M   Phosphate buffer

4.6. Immunohistochemistry and staining solutions

Phosphate buffer (0.2 M, pH 7.4)
0.04 M   Sodium dihydrogen phosphate (NaH$_2$PO$_4$)
0.16 M   di-Sodium hydrogen phosphate (Na$_2$HPO4)
Always prepared freshly

Citrate buffer (0.01 M, pH 6.0)
1.8 mM	Citric acid ($C_6H_8O_7 \times H_2O$)
8.2 mM	Sodium citrate ($C_6H_5O_7Na_3 \times 2H_2O$)

Always prepared freshly

BSA/PBS
0.04 M	Sodium dihydrogen phosphate (NaH_2PO_4)
0.16 M	di-Sodium hydrogen phosphate (Na_2HPO_4)
1.8% [w/v]	Sodium chloride
1.0% [w/v]	Bovine serum albumin (BSA)

Tris buffer (pH 7.6)
50 mM	Tris/HCl, pH 7.6
0.9% [w/v]	Sodium chloride (NaCl)

Always prepared freshly

Mayer's haematoxylin solution
0.1% [w/v]	Haematoxylin
0.02% [w/v]	Sodium iodate
5% [w/v]	Potassium aluminium sulphate ($K_2Al_2(SO_4)_4 \times 24H_2O$)

Added under constant shaking, solution turned violet blue
5% [w/v]	Chloralhydrate
0.1% [w/v]	Citric acid added

Added and filtered before use

Eosin solution
0.1% [v/v]	Eosin

12 drops of glacial acetic acid in 250 ml

Scott's solution
0.2% [w/v]	Potassium hydrogen carbonate
2% [w/v]	Magnesium sulphate

HCl - alcohol
0.09% [v/v]	HCl
70% [v/v]	Ethanol

Blocking buffer for fluorescent stainings
20% [v/v]	Goat serum
0.5% [v/v]	Triton X-100

Dissolved in BSA/PBS

Material

Mounting media
Eukitt   Kindler (Freiburg, Germany)
Aqua-Poly/Mount   Polysciences (Eppelheim, Germany)

4.7. Electron microscopy

Formvar solution
625 mg Formvar (Plano, Wetzlar, Germany)
50 ml Chloroform
Stirred for at least 30 min
Stored at RT protected from light

Carbon-stabilized grids (100 lines/inch Hex.mesh; Science Services)

Colloidal gold conjugated to protein A (Cell Microscopy Center; Department of Cell Biology, University Medical Center at Utrecht, The Netherlands)

Epoxy resin (Epon)
171.3 g   Glycidether 100
                      (Serva, Heidelberg, Germany)
115 g   DDSA (Dodecenyl succinic anhydride)
                      (Serva, Heidelberg, Germany)
89 g   MNA (Methyl nadic anhydride)
                      (Serva, Heidelberg, Germany)
Mixed using magnet stirrer for 10 min and then added
6.5 ml   DMP-30 (2,4,6-Tris(di-methyl-aminomethyl-)-phenol)
                      (Electron Microscopy Sciences, Munich, Germany)
Mixed using magnet stirrer for 20 min

4.8. Antibodies

Table 2: Immunoblot - Primary antibodies

Probe	Antibody	Species	Company/ Source	Concen-tration	Protein loaded	Gel
Lysate	Actin	Monoclonal mouse	Millipore	1:5000	5 µg	15%
Lysate	PLP/DM20 (A431)	Polyclonal rabbit	Jung, Sommer, Schachner, & Nave, 1996	1:5000	5 µg	15%
Myelin	PLP/DM20 (A431)	Polyclonal rabbit	Jung, Sommer, Schachner, & Nave, 1996	1:5000	0.8 µg	15%
Myelin	SIRT2 (16 mo pti)	Polyclonal rabbit	Abcam	1:2500	10 µg	10%
Myelin	SIRT2 (10 mo pti)	Polyclonal rabbit	Abcam	1:2500	10 µg	10%
Myelin	SIRT2 (4 mo pti)	Polyclonal rabbit	Abcam	1:500	0.78 µg	15%
Myelin	ATP1a3	Monoclonal mouse	Abcam	1:1000	10 µg	10%
Myelin	MBP	Monoclonal mouse	Novocastra	1:500	2.5 µg	15%

Table 3: Immunoblot - Secondary antibodies

Probe	Antibody	Species	Company/ Source	Concentration
Lysate	α-rabbit-HRP	Goat	Dianova	1:10000
Lysate	α-mouse-HRP	Goat	Dianova	1:10000
Myelin	α-rabbit-IRDye800CW	Goat	LI-COR	1:2500
Myelin	α-mouse-IRDye680RD	Goat	LI-COR	1:2500

Material

Table 4: Histological analysis - Primary antibodies

Antibody	Species	Company/Source	Concentration	Kit used
APP	Monoclonal mouse	Chemicon	1:1000	LSAB2 kit (Dako)
IBA1	Polyclonal rabbit	Wako	1:1000	LSAB2 kit (Dako)
GFAP	Monoclonal mouse	Novo Castra	1:200	Vector Elite ABC kit (Vector Labs)
MAC3	Monoclonal rat	Pharmingen	1:400	Vector Elite ABC kit (Vector Labs)
CD3	Monoclonal rat	Serotec	1:150	Vector Elite ABC kit (Vector Labs)
CD3	Monoclonal rat	Abcam	1:250	Vector Elite ABC kit (Vector Labs)
PLP (aa3)	Monoclonal rat	Yamamura, Konola, Wekerle, & Lees, 1991	1:100	No kit
MBP	Polyclonal rabbit	Dako	1:1000	No kit

Table 5: Histological analysis - Secondary antibodies

Antibody	Species	Company/Source	Concentration
α-rat-Alexa488	Goat	Dianova	1:1000
α-mouse-Alexa555	Goat	Dianova	1:1000
α-rat-biotinylated	Rabbit	Vector	1:100

Table 6: Cryo-immuno electron microscopy - Primary antibody

Antibody	Species	Company/Source	Concentration
PLP/DM20 (A431)	Polyclonal rabbit	Jung, Sommer, Schachner, & Nave, 1996	1:300

Table 7: Cryo-immuno electron microscopy - Secondary antibody

Antibody	Company/Source	Concentration
Colloidal gold conjugates to protein A	Cell Microscopy Center, Department of Cell Biology, University Medical Center Utrecht, The Netherlands	1:50

4.9. PCR Primers

Primers were synthesized in-house by the service facility of the Max Planck Institute of Experimental Medicine.

Genotyping primers (internal numbers)

Primers for genotyping of the *Flp* allele

15300: 5'- CACTGATATTGTAAGTAGTTTGC -3'
15301: 5'- CTAGTGCGAAGTAGTGATCAGG -3'

Primers for genotyping of the *Plp$^{lacZ\text{-}neo}$* allele

24460: 5'- GACATAGCCCTCAGTGTTCAGG -3'
24461: 5'- GAATCCTGCATGGACAGACAG -3'
15048: 5'- CAACGGGTTCTTCTGTTAGTCC -3'

Primers for genotyping of the *Plp^{flox}* allele

24460: 5'- GACATAGCCCTCAGTGTTCAGG -3' (labeled P1 in **Figure 9 c**)
24461: 5'- GAATCCTGCATGGACAGACAG -3' (labeled P2 in **Figure 9 c**)
32796: 5'- CACACACATATTCAGACCCCC -3' (labeled P4 in **Figure 9 c**)

Primers for genotyping of the *Nex/NeuroD6* allele

3131: 5'- GAGTCCTGGAATCAGTCTTTTTC -3'
3132: 5'- AGAATGTGGAGTAGGGTGAC -3'
2409: 5'- CCGCATAACCAGTGAAACAG -3'

Primers for genotyping of the *Cnp* allele

2016: 5'- GCCTTCAAACTGTCCATCTC -3'
7315: 5'- CCCAGCCCTTTTATTACCAC -3'
4193: 5'- CCTGGAAAATGCTTCTGTCCG -3'
4192: 5'- CAGGGTGTTATAAGCAATCCC -3'

Primers for genotyping of the tamoxifen inducible *Plp^{CreERT2}* allele

10099: 5'- TGGACAGCTGGGACAAAGTAAGC -3'
7963: 5'- CGTTGCATCGACCGGTAATGCAGGC -3'

Primers for genotyping of the *Plp* allele

1864: 5'- TTGGCGGCGAATGGGCTGAC -3'
2729: 5'- GGAGAGGAGGAGGGAAACGAG -3'
2731: 5'- TCTGTTTTGCGGCTGACTTTG -3'

Material

4.10. Mixes for PCR reaction

Mix for PCR reaction for *Flp* allele

4.2 µl	Go-Taq buffer (5 x)
2.1 µl	dNTP (2 nM)
0.2 µl	Primer 15300
0.2 µl	Primer 15301
0.07 µl	GoTaq DNA polymerase
13.23 µl	ddH$_2$0

Mix for PCR reaction for *Plp$^{lacZ\text{-}neo}$* allele

4.2 µl	Go-Taq buffer (5 x)
2.1 µl	dNTP (2 nM)
0.5 µl	Primer 24460
0.5 µl	Primer 24460
0.25 µl	Primer 15048
0.07 µl	GoTaq DNA polymerase
12.38 µl	ddH$_2$0

Mix for PCR reaction for *Plp^{flox}* allele

4.2 µl	Go-Taq buffer (5 x)
2.1 µl	dNTP (2 nM)
0.5 µl	Primer 24460 (labeled P1 in **Figure 9c**)
0.5 µl	Primer 24461 (labeled P2 in **Figure 9c**)
0.3 µl	Primer 32796 (labeled P4 in **Figure 9c**)
0.07 µl	GoTaq DNA polymerase
12.33 µl	ddH$_2$0

Mix for PCR reaction for *Nex/NeuroD6* allele

4.2 µl	Go-Taq buffer (5 x)
2.1 µl	dNTP (2 nM)
0.2 µl	Primer 3131
0.2 µl	Primer 3132
0.2 µl	Primer 2409
0.07 µl	GoTaq DNA polymerase
13.03 µl	ddH$_2$0

Mix for PCR reaction for *Cnp* allele

4.2 µl	Go-Taq buffer (5 x)
2.1 µl	dNTP (2 nM)
0.3 µl	Primer 4192
0.3 µl	Primer 4193
1 µl	Primer 2016
1 µl	Primer 7315
0.07 µl	GoTaq DNA polymerase
11.03 µl	ddH$_2$0

Mix for PCR reaction for *Plp^{CreERT2}* allele

4.2 µl	Go-Taq buffer (5 x)
2.1 µl	dNTP (2 nM)
0.2 µl	Primer 10099
0.2 µl	Primer 7963
0.07 µl	GoTaq DNA polymerase
13.23 µl	ddH$_2$0

4.11. Quantitative real-time PCR primers

Plp
Forward: 5'- CTCCAAAAACTACCAGGACTATGAG -3'
Reverse: 5'- AGGGCCCCATAAAGGAAGA -3'

Mbp
Forward: 5'- GCCTGTCCCTCAGCAGATT -3'
Reverse: 5'- CCTAAACCGATGCCTCCG -3'

Ube2l3
Forward: 5'- CACATTTGCGGATCTCTTCA -3'
Reverse: 5'- AGCAGCACCAGATCCAAGAT -3'

Rplp0
Forward: 5'- GATGCCCAGGGAAGACAG -3'
Reverse: 5'- ACAATGAAGCATTTTGGATAATCA -3'

Rps13
Forward: 5'- CGAAAGCACCTTGAGAGGAA -3'
Reverse: 5'- TTCCAATTAGGTGGGAGCAC -3'

4.12. Mouse lines

Plp$^{null/Y}$ mice (Klugmann et al., 1997)

Plp^{flox} mice (Luders et al., 2017)

Cnp^{Cre} mice (Lappe-Siefke et al., 2003)

Nex^{Cre} mice (Goebbels et al., 2006)

Plp^{CreERT2} mice (Leone et al., 2003)

Mice expressing FLIP recombinase body-wide (Farley et al., 2000) (129S4/SvJaeSor-Gt(ROSA26Sortm1(FLP1)Dym/J; backcrossed into C57BL/6N)

5. Methods

5.1. Animals

All mice used for the experiments in this thesis were bred and kept in the animal facility of the Max Planck Institute of Experimental Medicine with a 12 hour light/dark cycle and 2-5 animals per cage. All experiments were performed in accordance with the German animal protection law. For immunohistochemical stainings and FACS analysis mice were perfused using anesthetics and for all other analyses mice were sacrificed by cervical dislocation.

5.1.1. Establishment of mice with floxed *Plp* allele

In order to generate Plp^{flox} mice, we acquired embryonic stem cells (ES) harboring an engineered allele of the *Plp* gene from the European Conditional Mouse Mutagenesis Program (EUCOMM). ES cells were grown in the department of Neurogenetics in the Max Planck Institute of Experimental Medicine by Ramona Jung. In the transgenic facility of the Max Planck Institute of Experimental Medicine ES cells were microinjected into blastocysts derived from FVB mice and embryos were transferred to pseudo-pregnant foster mothers, yielding 13 chimeric males. Upon breeding with C57BL/6N-females germline transmission was achieved for ES clone EPD0160-2-D10. The offspring harboring the complete $Plp^{lacZ-neo}$ allele was interbred with mice expressing FLIP recombinase (129S4/SvJaeSor-Gt(ROSA)26Sortm1(FLP1)Dym/J; backcrossed into C57BL/6N) in order to excise the lacZ-neomycin resistance cassette *in vivo*. This yielded mice carrying the Plp^{flox} allele in which exon 3 of the *Plp* gene is flanked by loxP sites, and thereby can be excised by recombination with Cre.

5.1.2. Mouse models

To inactivate expression of *Plp* in excitatory projection neurons, exon 3 was excised *in vivo* upon appropriate interbreedings of Plp^{flox} mice with mice expressing Cre recombinase under control of the *Nex/NeuroD6* promoter (Goebbels et al., 2006), yielding mice referred to as $Plp^{flox}*Nex^{Cre/WT}$ mice. To inactivate expression of *Plp* in myelinating cells, exon 3 was excised *in vivo* upon interbreeding Plp^{flox} mice with mice expressing Cre recombinase under control of the *Cnp* promoter (Lappe-Siefke et al., 2003), yielding mice referred to as $Plp^{flox}*Cnp^{Cre/WT}$ mice. To conditionally inactivate expression of *Plp* in oligodendrocytes upon tamoxifen injection, Plp^{flox} mice were interbred with mice expressing tamoxifen inducible Cre recombinase under control of the *Plp* promoter (Leone et al., 2003) and exon 3 was excised *in vivo* upon tamoxifen injection. After tamoxifen injection Plp^{flox} mice are referred to as control mice (Ctrl) and $Plp^{flox}*Plp^{CreERT2}$ mice harboring the tamoxifen inducible Cre are referred to as induced conditional knockout mice (iKO). Furthermore $Plp^{null/Y}$ mice

which lack expression of *Plp* in all cells were analyzed. These mice were described previously (Klugmann et al., 1997).

5.1.3. Tamoxifen administration

Tamoxifen (Sigma-Aldrich) was diluted in corn oil (Sigma-Aldrich) and mixed on a vortexer (Heidolph) in the dark for at least half an hour at RT. It was freshly prepared each time for the following five days of injections and kept in the dark at 4°C for those five days. Mice were injected with tamoxifen intraperitoneally (i.p.) at the age of 8 weeks (1 mg/100 µl corn oil per mouse per day) for 10 consecutive days with a 2 days break after the first 5 days of injection, by a protocol adapted from (Leone et al., 2003).

5.1.4. Genotyping of mice

At postnatal day 21 tail tips (0.5 cm long) or ear punches were taken and digested overnight (o/n) in 180 µl 1 x MGB with 20 µl Proteinase K (Boehringer GmbH) at 55°C with agitation. The next day tails were incubated at 95°C for 10 min to inactivate proteinase K. Polymerase chain reaction (PCR) (Mullis et al., 1986; Saiki et al., 1988) was used to amplify specific DNA segments. The amount of PCR-mix needed for the number of tail tips for the specific PCR reaction was calculated (see material). Each PCR reaction was performed with 20 µl PCR-mix and 1 µl DNA in a T3 or Gradient Thermocycler (Biometra). Primers were synthesized in house by the service facility of the Max Planck Institute of Experimental Medicine. After the PCR, 5 µl Gel Red Nucleic Acid Stain (BioTrend; 1:2500 in ddH$_2$O) was added to each PCR reaction to visualize DNA. PCR products were separated on 2% [w/v] agarose gels in TAE buffer for 30-60 min at 120 V along with the marker GeneRuler 100 bp DNA ladder (Thermo Fisher Scientific). Pictures for documentation were taken with the Intas UV system.

5.2. RNA isolation and analysis

5.2.1. RNA isolation

RNA extraction and purification was performed using the RNeasy Mini Kit (Qiagen). The kit's working principle is the selective binding of RNAs bigger than 200 bases to a silica-gel based membrane under high-salt conditions. Frozen (-80°C) half brains of mice were homogenized in 3 ml 0.32 M sucrose with protease inhibitor (Complete Mini, Roche) using an Ultraturrax homogenizer (IKA T10 Basic). 100 µl of the homogenate was directly transferred to 600 µl RLT buffer (RNeasy Miniprep kit; Qiagen) with beta-mercaptoethanol (Fluka, BioChemika). The rest of the homogenate was either used for myelin purification or saved at -80°C. Samples in RLT buffer were mixed at RT for 3 min and then stored at -80°C until RNA isolation. RNA isolation and qRT-PCR from Ctrl mice and iKO mice in **Figure 15 c, 15 d** was

done by Ursula Kutzke. Samples were thawed quickly and RNA isolation was performed using the RNeasy Mini Kit (Qiagen) following the manufacturer's protocol. Briefly, one volume of ethanol was added to the samples, mixed and applied to RNeasy columns. The columns were centrifuged for 1 min at 16000 × g, washed one time with the RW1 buffer (RNeasy Miniprep kit; Qiagen) and two times with the RPE buffer (RNeasy Miniprep kit; Qiagen) and RNA was eluted with 50 µl of RNAse-free ddH$_2$O.

5.2.2. RNA measurement

The quality of RNA was tested using the Agilent RNA 6000 Nano KIT and the Agilent 2100 Bioanalyzer following the company's instructions. The amount of RNA was measured using the NanoDrop 2000 Spectrophotometer (Thermo Fisher Scientific) and the RNA concentration for all samples was adjusted to 100 ng/µl.

5.2.3. cDNA synthesis

As a next step the isolated RNA was transcribed into a complementary single stranded DNA (cDNA) in a reverse transcription reaction catalyzed by RNA dependent DNA polymerase SuperScript III (Invitrogen). Per PCR tube 1 µl dT-mixprimer (0.6 pmol/µl) and 1 µl random nonamer primers (25 pmol/µl) as well as a total of 4 µl RNA and ddH$_2$O were pipetted (so that the same amount of RNA was in each tube, approximately 400 ng/4 µl according to the Nanodrop measurement). After shortly spinning the mixture down in a centrifuge, RNA and primers were denatured at 70°C for 1 min and then the PCR tubes with the mixture were put on ice. The mastermix was added (2 µl of 5 x first strand buffer, 0.5 µl dNTP (10 mM), 1 µl DDT (100 mM) and 1 µl SuperScript III reverse transcriptase (200 U/µl)) and the total reaction mixture was incubated in a T3 or Gradient Thermocycler (Biometra) with the following settings:

25°C   10 min
50°C   45 min
55°C   45 min

Synthesized cDNA was diluted 1:30 with ddH$_2$O and stored at -20°C.

5.2.4. Quantitative real-time PCR

The pipetting robot epMotion 5075 (Eppendorf) was used for pipetting and the qRT-PCR was performed using the Power SYBR Green PCR Master Mix (Applied Biosystems) and the Light Cycler 480II (Roche). The mixture for the gene expression analysis contained 5 µl of SYBR Green Master Mix, 2 µl of cDNA (2 ng/µl) and 0.1 µl of each primer (10 pmol/µl) and 2.8 µl ddH$_2$O. All reactions were performed in

quadruplicates. The qRT-PCR reaction was carried out using the following settings: 60°C for 1 min and 95°C for 15 sec [50 cycles]. mRNA abundance was analyzed in relation to the mean of the standards *Ube2l3*, *Rplp0* and *Rps13*, which did not differ between genotypes. Statistical analysis was performed using GraphPad Prism 6.0.

5.3. Biochemical protein analysis

5.3.1. Myelin purification

Myelin purification was performed after a protocol adapted from (Larocca and Norton, 2007; Norton and Poduslo, 1973). Mice were sacrificed by cervical dislocation and brains were dissected. After removal of optic nerves, brains were cut in half, frozen on dry ice and then stored at -80°C. For myelin purification half brains of mice were taken from -80°C and directly homogenized in 3 ml cold 0.32 M sucrose with protease inhibitor (Complete Mini, Roche) in centrifugation tubes (14 × 89 mm, Beckman) using an Ultraturrax homogenizer (IKA T10 Basic) on level 3. 100 µl of this homogenate was taken for RNA purification (chapter 5.2.) and afterwards 3 ml 0.32 M sucrose was added to the homogenate and briefly homogenized again. 400 µl of this homogenate was frozen at -80°C and the remaining homogenate was carefully layered on top of 3 ml 0.85 M sucrose in fresh centrifugation tubes (14 × 89 mm, Beckman). Probes were constantly kept on ice and all centrifugation steps were carried out at 4°C. All 6 samples of one time point were processed simultaneously (n=3 controls and 3 experimental samples) and were adjusted to the same weight before each centrifugation step. To accumulate the myelin fraction at the interphase between the two sucrose concentrations, samples were centrifuged with a Sorvall WX+ Ultra series centrifuge (Thermo Fisher Scientific) in a TH641 rotor (Thermo Fisher Scientific) at 75000 × g (24000 rpm) for 30 min with both acceleration and deceleration prolife set at 7. The interphase was taken out with a glass pipette and transferred to a fresh centrifugation tube. To wash the interphase the centrifugation tubes were filled up with ddH$_2$O and centrifuged for 15 min at 75000 × g (24000 rpm) with both acceleration and deceleration prolife set at 9 (maximum). The supernatant was discarded and the pellet was resuspended in a small volume of ice cold ddH$_2$O. Afterwards the tube was filled up with ddH$_2$O and incubated for 15 min on ice for the first osmotic shock. After 15 min centrifugation at 12000 × g (9800 rpm) with both acceleration and deceleration prolife set at 9 (maximum) the supernatant was discarded and a second osmotic shock was performed in the same way. The pellet was afterwards resuspended in a 3 ml 0.32 M sucrose and this re-homogenate was carefully layered on top of 3 ml 0.85 M sucrose to perform a second purification step with the same settings as above (75000 × g (24000 rpm) for 30 min with both acceleration and deceleration prolife set at 7). The interphase was washed again by resuspending it in ddH$_2$O and centrifugation for 15 min at 75000 × g (24000 rpm) with both acceleration and deceleration prolife set at 9 (maximum). The pellet was finally resuspended in 200 µl 1 x TBS (137 mM NaCl, 20 mM Tris/HCl pH 7.4) with protease

inhibitor and frozen at -80°C. The purified myelin was slowly thawed on ice and homogenized once again with a mortar before the protein concentration was measured.

5.3.2. Lysate preparation

For immunoblotting displayed in **Figure 9 g**, mice were sacrificed at postnatal day 21, brains were dissected, cut in half and frozen at -80°C. Frozen half brains were homogenized in 0.32 M sucrose with protease inhibitor (Complete Mini, Roche) using an Ultraturrax homogenizer (IKA T10 Basic). 200 µl of the lysate were directly transferred into 200 µl of 2 x RIPA buffer (200 mM Tris/Cl pH 7.5; 600 mM NaCl; 2 mM EDTA; 2% Triton X-100; 1% SDS with protease inhibitor) to obtain brain lysate in 1 x RIPA buffer. After 15 min on ice, samples were centrifuged at 13000 rpm for 10 min at 4°C. The protein concentration of the supernatant was measured.

5.3.3. Measurement of protein concentration

The protein concentration of purified myelin and lysate were measured with the Lowry assay (Lowry et al., 1951; Peterson, 1979) using the Bio-Rad DC Protein assay kit (Bio-Rad). The "microplate assay" protocol of the manufacturer was used and the optical density was measured at 650 nm using Eon™ High Performance Microplate Spectrophotometer (BioTek).

5.3.4. Protein separation using SDS PAGE

Sodium dodecyl sulfate-polyacrylamide gel electrophoresis (SDS PAGE) was performed after a protocol established by Laemmli (Laemmli, 1970). The Bio-Rad system was used to cast gels and separate proteins. Acrylamid gels (1.5 mm thick; 10% or 12% acrylamid) were casted between glass cover plates, overlaid with isopropanol and polymerized for 30 min. Isopropanol was rinsed off with ddH$_2$O, excess water was taken up with filter paper and the stacking gel was casted on top of the separating gel. Wells to load protein mix onto the gel were created using plastic combs from Bio-Rad. Gels were stored in moist paper towels at 4°C for no longer than a week or used directly. Myelin and lysate samples were adjusted to the desired protein concentration. 1 x SDS buffer and 5% [v/v] mercaptoethanol were added to denature the proteins, and the samples were heated for 10 min at 40°C. All samples used for one immunoblot were adjusted to the same protein concentration and processed in parallel. Gels were assembled in Bio-Rad chambers and the chambers were filled with 1 x Laemmli running buffer. Protein samples were carefully pipetted into the prepared gel-wells and separated using the Bio-Rad power supply at 170 V for 1 hour. Afterwards gels were removed from the cover plates and incubated in transfer buffer for 15 min before proteins were transferred to a polyvinylidene difluoride (PVDF) membrane.

5.3.5. Immunoblot

After separation, proteins were transferred to a PVDF membrane as described by Towbin and colleagues (Towbin et al., 1979). Therefore The PVDF membrane (Hybond; Amersham) was activated using 100% ethanol for 1 min, washed two times shortly with ddH$_2$O and kept in transfer buffer. The protein transfer was performed using the Novex® Semi-Dry Blotter (Invitrogen). Four Whatman filter papers soaked in cold transfer buffer were placed onto the anode plate and each filter paper was rolled with a blotting roller to remove any air bubbles. The activated PVDF membrane was placed on top of the filter papers, followed by the gel and four more Whatman papers (soaked in transfer buffer). Proteins were transferred at 20 V for 40 min using the Bio-Rad power supply. Up to four gels could be transferred simultaneously.

5.3.6. Immunodetection of blotted proteins with the Intas ChemoCam system

After the protein transfer, PVDF membranes were removed from the Semi-Dry Blotter and incubated in blocking buffer (was 5% [w/v] non-fat dry milk in TBST) at RT for 1 hour. The primary antibody was diluted in 5 ml blocking buffer and incubated in a 50 ml Falcon Tube on a rotor at 4°C o/n with the membrane. The next day, the membrane was washed 3 × 5 min in TBST and incubated with HRP-coupled secondary antibody (Dianova), diluted in 5 ml blocking buffer on a rotor for 1 hour at RT. Afterwards membranes were washed in TBST 3 × 5 min. Membranes were carefully picked up with forceps, excess liquid was removed by carefully holding one corner of a membrane against a paper towel and the membrane was placed onto a glass plate. Enhanced Chemiluminescence Detection (ECL) solution was added according to the manufacturer's recommendations (0.5 ml of each solution) (Western Lightning™, Western Blot Chemiluminescence Reagent Plus, PerkinElmer Life Sciences, Inc.). After 1 min of incubation, excess liquid was removed again and the membranes were placed between two plastic foils and chemiluminescence was scanned for 15 min using the Intas ChemoCam system (Intas).

5.3.7. Immunodetection of blotted proteins with the Odyssey infrared imager

The protocol for incubation with antibodies was the same as for detection with the Intas ChemoCam system. Instead of milk in TBST, blocking was done with 50% Odyssey®Blocking buffer (LI-COR) in TBST. Primary antibody was incubated in 50% Odyssey®Blocking buffer (LI-COR) in TBST with additional 0.1% Tween-20 (Promega). Fluorescently coupled secondary antibody was incubated in 50% Odyssey®Blocking Buffer (LI-COR) in TBST with additional 0.1% Tween-20 and 0.01% SDS. After incubation with the secondary antibody membranes were washed 3 × 5 min in with TBST and 2 times shortly with ddH$_2$O and fluorescent signal was detected using the Odyssey infrared imager (LI-COR). Relative intensity of

fluorescent bands was measured in relation to the background using Image Studio Ver 3.1. Graphs were plotted using GraphPad Prism 6.0 and an exponential curve with one phase decay was fitted in **Figure 16 b**, **16 c**. Statistical analysis was performed using a two-tailed unpaired t-test in GraphPad Prism 6.0. for each individual time point in **Figure 16 b**, **16 c** and for graphs e, f and h. Levels of significance were set as $p<0.05$ (*), $p<0.01$ (**) and $p<0.001$ (***).

5.4. Histological analysis

5.4.1. Perfusion fixation of mouse tissue

For histological analysis mice were perfused. After anesthetizing mice by i.p. injection of avertin (0.2 ml per 10 gram of body weight), and confirming successful anesthesia by pinching the hind paw, animals were stabilized with the ventral side up. The heart was exposed by opening the chest and diaphragm with three excisions. A butterfly (27G, Venofix) was injected into the left ventricle, while the right atrium was cut. The butterfly was connected to a peristaltic pump and the blood was flushed out with 37°C warm HBSS (Invitrogen) for 4 min. A tail biopsy for re-genotyping was taken during these 4 min. Afterwards mice were perfused with 37°C warm 4% [w/v] PFA for at 6-8 min (40-50 ml PFA) to fix the tissue. Brains and spinal cords (with vertebrae) were dissected, stored at 4°C in 4% [w/v] PFA o/n and then transferred to 1% [w/v] PFA and stored at 4°C.

5.4.2. Paraffin-embedding and sectioning

Brains were taken from 1% [w/v] PFA and cut into three pieces with two coronal sections. Vertebrae were removed from the spinal cords and spinal cords were cut into two pieces (cervical, thoracic and lumbar spinal cord). Brains and spinal cords were placed into plastic molds for embedding in Paraffin (Paraplast; Leica) using the Microm HMP110 tissue processor (MICROM) with the following program:

1 hour	50% Ethanol
2 × 2 hours	70% Ethanol
2 × 2 hours	96% Ethanol
2 × 2 hours	100% Ethanol
1 hour	Isopropanol
2 × 2 hours	Xylol
2 × 2 hours	Paraffin

Afterwards, the three brain slices and the spinal cord (again cut into six pieces: 2 cervical, 2 thoracic and 2 lumbal) per animal were placed in a metal form and casted with 60°C warm paraffin. Metal forms were removed after cooling down of the paraffin, labeled at stored at RT. 5 µm thick slices were cut using the HM400R Microtome (MICROM) partly by Annette Fahrenholz, dried at 37°C o/n and stored at RT.

5.4.3. DAB staining

DAB staining was performed by Annette Fahrenholz. For staining of neuropathological markers, sections were first deparaffinized in glass cuvettes by the following steps:

10 min	60°C
2 × 10 min	Xylol
10 min	Xylol/Isopropanol (1:1)
5 min	100% Ethanol
5 min	90% Ethanol
5 min	70% Ethanol
5 min	50% Ethanol
5 min	ddH$_2$O

To permeabilize the tissue, slides were incubated in citrate buffer for 5 min and then cooked for 10 min in boiling citrate buffer (650 W in microwave oven). After cooling for about 20 min, sections were rinsed with Tris buffer containing 2% [w/v] milk powder. To make sure that small volumes of the antibody-solutions were evenly distributed across the tissue, glass slides were placed into Shandon cover plates (Thermo Fisher Scientific) and rinsed again with Tris buffer containing 2% [w/v] milk powder. Since horse radish peroxidase (HRP) coupled secondary antibodies were used, it was necessary to inhibit the endogenous peroxidase activity by applying 3% [v/v] hydrogen peroxide for 5 min. Afterwards slides were washed with Tris buffer containing 2% [w/v] milk powder and incubated in blocking solution (20% [v/v] goat serum in BSA/PBS) for 30 min at RT. Primary antibodies were diluted in BSA/PBS and incubated o/n at 4°C. The next day, slides were washed with Tris buffer containing 2% [w/v] milk powder. Staining of amyloid beta precursor protein (APP), allograft-inflammatory factor (AIF1/IBA1) and glial fibrillary acidic protein (GFAP) was performed using the LSAB$_2$ kit (Dako). Using the kit, sections were incubated with 100 µl of bridging antibody i.e. a biotinylated secondary antibody for 10 min at RT. After rinsing with Tris buffer containing 2% [w/v] milk powder, the HRP complex bound antibody was incubated for 10 min at RT. For staining of lysosomal-associated

membrane protein 2 (LAMP2/MAC3) and the T cell marker cluster of differentiation 3 (CD3), sections were incubated with an α-rat-biotinylated antibody (Vector Labs) for 30 min. The two components of the Vector Elite ABC kit (Vector Labs) were mixed and incubated for 30 min. Afterwards the Shandon cover plates were removed and all sections (for APP, MAC3, IBA1, GFAP and CD3 staining) were rinsed with Tris buffer without milk-powder. The HRP substrate 3,3'-Diaminobenzidine was applied by using the DAB Zytomed Kit (Zytomed Systems GmbH). Slides were incubated with DAB for 10 min, so that brown labeling appeared where antibodies recognized their targets. After additional washing with ddH$_2$O, sections were incubated in 0.1% Haematoxylin for 5 min to label nuclei. Nuclei were stained blue due to the interaction of Haematoxylin with the basic nuclear compartment. After rinsing with ddH$_2$O sections were incubated with HCl-Alcohol for 5-10 sec and with Scott's solution for 5 min. After rinsing with ddH$_2$O again, slides were stained with 0.1% Eosin for 3-5 min to visualize cytoplasm and connective tissue. Slides were rinsed again with ddH$_2$O. Tissue was then dehydrated by an alcohol gradient (50%, 70%, 90%, and 100% for 5 min each), incubated with xylol/isopropanol (1:1) for 5 min, two times for 5 min in xylol and finally mounted using Eukitt (Kindler).

5.4.4. Imaging and quantification of DAB stainings

Images were taken with an AxioImager Z1 bright-field light microscope (Zeiss) coupled to an AxioCam MRc camera (Zeiss) controlled by Zeiss ZEN 1.0 software. Images were captured at 10 × (CD3), 20 × (GFAP, IBA1, MAC3), 40 × (APP) or 100 × (representative images for the Figures) magnification and processed using Fiji. For quantification, the hippocampal fimbriae or the corpus callosum were selected and CD3-immunopositive (CD3+) T cells and APP-immunopositive (APP+) axonal spheroids were counted. To quantify white matter area immunopositive for IBA1, MAC3 or GFAP, the fimbriae were selected and analyzed using an ImageJ plug-in (de Monasterio-Schrader et al., 2013) for semi-automated analysis. For this analysis the color threshold was used to transform the colored picture to a black and white picture and brown signal was detected as positive black signal. Then, the area of the positive black signal was measured and related to the size of the analyzed area. For each animal the average of both fimbriae was calculated. CD3 in **Figure 21 a**, **21 c** was counted on 5 slides per animal at 4 months pti (n=6), 7 slides per animal at 6-8 months pti (n=5), 2-4 slides per animal at 10 months pti (n=5-6), 2 slides per animal at 16 months pti (n=5-7), and 1-2 slides per animal in 6-months-old wild type (n=3) and *Plp*$^{null/Y}$ (n=10) mice. All other markers and CD3 in **Figure 13** were analyzed on one slide per animal. For the time point depicted as 6-8 months tamoxifen, n=3 mice were collected 6 months pti and n=2 mice were collected 8 monhs pti. All quantifications were performed blinded to the genotype. Statistical analysis was performed using one-way ANOVA with Tukey's multiple comparison post-test in GraphPad Prism 6.0. Levels of significance were set as $p < 0.05$ (*), $p < 0.01$ (**) and $p < 0.001$ (***).

5.4.5. Fluorescent staining

Fluorescent immunolabeling was performed on 5 µm paraffin-embedded cross sections of mouse brains. Brain slices were depariffinized in xylol, rehydrated in a graded alcohol series and tissue was permeabilized with citrate buffer as described in chapter 5.4.3. Unspecific binding sites were blocked with blocking solution contained 10% goat serum and 1% BSA in PBS. Primary antibodies were diluted in blocking buffer and incubated at 4°C o/n. The next day, slides were washed in 1 x PBS three times 10 min. Secondary antibodies were incubated for 2 hours at RT. Slides were washed with 1 x PBS and then incubated with DAPI (1:10000) for 5 min. After additional washing, tissue was mounted using Aqua-Poly/Mount (Polysciences).

5.4.6. Imaging of fluorescent staining

Slides were imaged with the confocal microscope Leica SP5 (Leica) using the objective HCX PL APO CS 63.0 × 1.30 GLYC 21°C UV. An argon laser with the excitation of 488 nm was used to excite the Alexa 488 fluorophore, and the emission was set to 500-526 nm. The laser DPSS 561 was used to excite the Alexa 555 fluorophore, and the emission was set to 575-630 nm. LAS AF lite software was used to export the images as TIF files.

5.5. Cryo-immuno electron microscopy

5.5.1. Tissue preparation

Mice were sacrificed by cervical dislocation, optic nerves were carefully removed and fixed with Immuno-Karlsson-Schultz fixative o/n (25 hours) and then transferred to 1% [w/v] PFA. Fixed optic nerves were washed with PBS, immersed with 2.3 M sucrose in 0.1 M phosphate buffer o/n, mounted in 10% [w/v] gelatine for ultramicrotome cutting and frozen in liquid nitrogen.

5.5.2. Cryosections and immunogold labeling

Cutting of ultrathin cryosections and immunogold labeling was performed according to the "Tokuyashu technique" (Tokuyasu, 1973) similar to the protocol published in (Werner et al., 2007) by Ramona Jung. 50 nm thin cryosections were cut with a UC6 cryo-ultramicrotom (Leica) and picked up on formvar-filmed carbon-stabilized grids (100 lines/inch Hex.mesh; Science Services) in a 1:1 mixture of 2% [w/v] methylcellulose (Sigma-Aldrich) and 2.3 M sucrose (Liou et al., 1996). After washing with PBS and PBS with 0.1% glycine [w/v], sections were blocked with 1% [w/v] BSA in PBS for 3 min. The primary antibody (PLPA431) was diluted 1:300 in 1% [w/v] BSA in PBS and incubated for 30 min. After washing with 0.1% [w/v] BSA in PBS tissue was incubated with protein A-gold (10 nm) in 1% [w/v] BSA in PBS. Colloidal

gold conjugated to protein A was obtained from the Cell Microscopy Center (Department of Cell Biology, University Medical Center at Utrecht, The Netherlands) and prepared as done previously (Roth et al., 1978; Slot and Geuze, 1985). Afterwards grids were incubated in 1% [v/v] glutaraldehyde in PBS for 5 min to fix gold and antibody and for denaturation of the FC domain. After washing with ddH$_2$O tissue was contrasted with neutral uranyl acetate (2% [w/v] in 0.15 M oxalic acid, pH adjusted to 7.0 with ammonium hydroxide) for 5 min. After further washing with PBS, grids were transferred to ice-cold droplets of 1.8% [w/v] methylcellulose containing 0.4% [w/v] uranyl acetate for 5 min, and picked up with a wire loop. Excess fluid was drained from the loop by gentle tapping to Whatman filter paper, and the sections were embedded in the remaining thin film by air-drying (Liou et al., 1996). Sections were analyzed with a LEO EM912 Omega (Zeiss) and digital micrographs were obtained with an on-axis 2048 × 2048-CCD camera (TRS, Moorenweis) with 10000 × magnification.

5.5.3. Analysis of immunogold labeling

Per animal 41-58 myelin profiles were analyzed on 6-9 images per animal (5.9 µm² per image → 35.4-53.1 µm² per animal) using Fiji. This corresponds to 3.4-8.4 µm² myelin area analyzed per animal. The inside and outside half area of myelin was measured and gold-particles were counted within these areas. Graphs display gold particles per µm² myelin normalized to mean of Ctrl mice. All quantifications were performed blinded to the genotype. Statistical analysis was performed using a two-tailed unpaired t-test in GraphPad Prism 6.0. Level of significance was set as $p < 0.05$ (*).

5.6. High pressure freezing, freeze substitution and electron microscopy

Samples for transmission electron microscopy by high pressure freezing and freeze substitution were prepared as described (Mobius et al., 2010) together with Dr. Wiebke Möbius, Torben Ruhwedel, Martin Meschkat and Boguslawa Sadowski. After sacrificing mice by cervical dislocation optic nerves were dissected and placed into aluminium specimen carriers with an indentation of 0.2 mm. The remaining space was covered with 20% [w/v] polyvenylpyridilone (PVP) (Sigma-Aldrich P2307-100G, molecular weight 10000) in PBS. The sample was cryofixed using a HPM100 high-pressure freezer (Leica) and freeze substitution was carried out in a Leica AFS (Leica) according to the following protocol: first, samples were kept in tannic acid (0.1% [w/v] in acetone) at -90°C for 100 hours, then washed with acetone (4 × 30 min, -90°C) and afterwards transferred into Osmiumtetroxyde (OsO$_4$) (Electron Microscopy Systems; 2% [w/v]) and uranyl acetate (SPI Chem, 0.1% [w/v]) in acetone at -90°C. The temperature was raised from -90 to -20°C in increments of 5°C/hour, then kept unaltered at -20°C for 16 hours, and then raised to +4°C in increments of 10°C/hour. After washing with acetone (3 × 30 min at 4°C), samples

were allowed to adjust to room temperature for 1 hour. Afterwards, optic nerves were transferred into Epon (Serva, Heidelberg) (25%, 50%, and 75% Epon in acetone for 1-2 hours each, 90% Epon in acetone for 18 hours, 100% Epon for 4 hours). Finally, the samples were placed in embedding molds for polymerization (60°C, 24 hours). Ultrathin sections (50 nm) were cut using a Leica Ultracut S ultramicrotome (Leica) and contrasted with an aqueous solution of 4% [w/v] uranyl acetate (SPI Chem) followed by lead citrate according to Reynolds (Reynolds, 1963). The samples were examined in a LEO 912AB Omega transmission electron microscope (Zeiss). Pictures were taken with an on-axis 2048 × 2048-CCD-camera (TRS, Moorenweis). For assessment of pathology, 3 Ctrl mice and 3 iKO mice were analyzed at 10 months pti. Randomly selected, non-overlapping images were taken at 7000 × magnification. Per animal 5 electron micrographs (1105 µm²) were analyzed using ImageJ (Fiji). Myelinated and non-myelinated axons were categorized into "normal appearing myelin", "myelin with channels or lamella-splitting" and "non-myelinated axons" and these three categories were expressed in percent of all axons counted (sum of the three categories). Furthermore we counted "axons with myelin comprising a swollen adaxonal compartment (inner tongue)", "outfoldings", "myelin profiles with degenerating and degenerated axons" and expressed the number of these events in percent of all axons counted (sum of the first three categories). The number of axons harboring additional small axonal profiles in association with the inner tongue ("axons with sproutings") was expressed as percentage of axons-myelin units which could be evaluated for this. To quantify "axonal spheroids" at least 20 images, taken at 3000 × magnification (at least 15800 µm²), were analyzed per animal. The number of axonal spheroids is normalized to the area analyzed of each individual animal and expressed as axonal spheroids/mm². All statistical analyses were performed using GraphPad Prism 6.0. All quantifications were performed blinded to the genotype. Levels of significance were set as $p < 0.05$ (*), $p < 0.01$ (**) and $p < 0.001$ (***).

5.7. Preparation of CNS mononuclear cells and flow cytometry

Fluorescence-activated cell sorting (FACS) analysis was essentially performed as described in (Lagumersindez-Denis et al., 2017) in collaboration with Dr. Stefan Nessler (Department of Neuropathology, UMG Göttingen). Mice were injected i.p. with Heparin (5IU/g body weight) and 15 min later they were transcardially perfused with HBSS and Heparin. Brains were dissected and after removal of meninges brains were digested in 2.5 ml DMEM containing 2.5 mg/ml Collagenase D (Roche) and 1 mg/ml DNAse I (Roche) for 5 min in a water bath at 37°C. After short mixing by turning the tube upside down by hand several times, the mixture was placed on a rotor at 37°C for 25 min. By pressing the mixture through a strain the tissue was separated into small pieces and the digestion was stopped as collagenase was diluted by rinsing the strain with DMEM. After short centrifugation in an Eppendorf 5810R centrifuge, cells were washed with DMEM and 2% [v/v] FCS (Sigma-Aldrich) to wash out the collagenase and DNAse. After short centrifugation, cells were taken

up in 5 ml 37% [v/v] PercolTM (GE Healthcare) in DMEM and layered over 5 ml 70% PercolTM in DMEM. Afterwards the mixture was centrifuged at 1600 rpm at 15°C with in an Eppendorf 5810R centrifuge to collect mononuclear cells at the interphase. The interphase with the cells was removed, washed with PBS with 2% [v/v] FCS (Sigma-Aldrich) and subsequently the cells were blocked with αCD16/32 (BioLegend, Clone 93) for 15 min.

Stainings were performed in a 96 well plate (Thermo Fisher Scientific). Antibodies were diluted in PBS with 2% [v/v] FCS (Sigma-Aldrich) and incubated on the cells on ice for 15 min. Afterwards the cells were washed using 200 µl PBS with 2% FCS [v/v] (Sigma-Aldrich) twice. To collect the cells at the bottom of the wells, they were centrifuged at 1200 rpm for 5 min with the Eppendorf 5810R centrifuge after each step. The following antibodies were used in the dilutions as indicated (all from BioLegend unless stated otherwise): αCD3 (145-2C11) 0.4 µl/ 50µl, αCD4 (RM4-5) 0.4 µl/50 µl, αCD8 (53-6.7) 0.4 µl/ 50 µl, αCD11b (M1/70) 0.4 µl/50 µl, αCD19 (eBio1D30, eBioscience) 4 µl/50 µl, αCD25 (PC61.5) 0.4 µl/50 µl, αCD45 (30-F11) 0.4 µl/50 µl, αFoxP3 (FJK-16S, eBioscience) 0.4 µl/50µl, αLy6C (HK1.4) 0.1 µl/50 µl, αLy6G (1A8) 0.4 µl/50 µl, αCCR2 (R&D 475301) 2.5 µl/50µl. For intracellular αFoxP3 staining, cells were fixed after surface staining for 45 min and permeabilized for 30 min using the eBioscience FoxP3 staining kit. All flow cytometry data were acquired on a FACS Canto^{Tm} II (BD Bioscience) device and analyzed with the FlowJo software (v. 7.6.1, Tree Star Inc).

Immune cell subsets were defined as following:
Microglial cells: CD45^{int} CD11b+ Ly6C- Ly6G-
T cells: CD45^{high} CD3+ CD19-
CD4+ T cells: CD45^{high} CD3+ CD4+
Regulatory T cells (T$_{reg}$ cells): CD45^{high} CD3+ CD4+ CD25+ FoxP3+
CD8+ T cells: CD45^{high} CD3+ CD8+
B cells: CD45^{high} CD19+ CD3-

5.8. Statistical analysis and figure assembly

All graphs and statistical analyses were done using the software GraphPad Prism 6.0. Levels of significance were set as $p<0.05$ (*), $p<0.01$ (**) and $p<0.001$ (***). For comparison of two groups an unpaired two-tailed student's t-test was performed. For comparison of more than two groups a one-way ANOVA with Tukey's multiple comparison test was performed. Scanned pictures were cut using Adobe Photoshop CS6 and arranged in Adobe Illustrator CS6.

6. Results

6.1. Genetic dissection of oligodendroglial and neuronal *Plp* function in a novel mouse model of SPG2

Plp expression has been viewed to be restricted to the oligodendrocyte lineage for a long time but recently it has been additionally reported in neurons (**Table 1**), leading to the assumption that lack of neuronal *Plp* expression may cause neuronal dysfunctions in SPG2 patients and respective mouse models (Fulton et al., 2011; Jacobs et al., 2003; Sarret et al., 2010). To test this hypothesis, we established a mouse model in which *Plp*-deletion can be controlled cell-type specifically and evaluated the neuropathological appearance of mice lacking PLP specifically in oligodendrocytes or neurons. All data in this part (6.1.) were published in (Luders et al., 2017).

6.1.1. *Plp* expression in neurons

To evaluate whether neuronal *Plp* expression is also reflected in an unbiased approach, we analyzed original data from and RNA-Seq database of brain cell types sorted from the cortex of mice (GEO dataset GSE52564). In the original publication (Zhang et al., 2014) FPKM (fragments per kilobase of exon per million fragments mapped)-values of 0.04 and 0.1 were chosen as minimum and conservative thresholds for a gene to be accepted as expressed in a particular cell type, respectively. Regarding the original data, an even more rigorous threshold FPKM-value of 0.8 was exceeded for *Plp* mRNA in cortical neurons, astrocytes and microglia, while *Fa2h* and *Gjc2/Cx47* mRNA did not reach this threshold (**Figure 9 a**). As expected, mRNAs of *Plp*, *Fa2h* and *Gjc2/Cx47* were strongly enriched in newly formed and mature oligodendrocytes (**Figure 9 b**). Together, *Plp* mRNA is enriched in but not exclusive to oligodendrocytes. Indeed, low-level expression of *Plp* is also seen in neurons.

6.1.2. Mice with oligodendroglial or neuronal deletion of *Plp*

To investigate the possible pathobiological relevance of neuronal *Plp* expression *in vivo*, we have established a novel mouse model that allows cell type-dependent Cre-mediated recombination of the *Plp*-gene. ES cells with a *Plp$^{lacZ-neo}$* allele were acquired from EUCOMM, microinjected into blastocysts and these were injected into pseudo-pregnant foster mothers. After germ-line transmission of the *Plp$^{lacZ-neo}$* allele, FRT-sites were reombined *in vivo* and we obtained mice harboring the *Plp^{flox}* allele in which exon 3 of the *Plp* gene is flanked by loxP sites (**Figure 9 c**). Male *Plp$^{flox/Y}$* and

female $Plp^{flox/flox}$ mice were born at expected frequencies. To recombine Plp in oligodendrocytes we used Cnp^{Cre} driver mice which express Cre in myelinating cells (Lappe-Siefke et al., 2003). Female $Plp^{flox/flox}$ and male $Plp^{flox/Y}*Cnp^{Cre/WT}$ mice were interbred, yielding males of the genotype $Plp^{flox/Y}*Cnp^{Cre/WT}$ and $Plp^{flox/Y}$ control mice. Genotyping PCR (**Figure 9 d**) shows efficient Cre-mediated recombination of the Plp^{flox} allele by Cnp^{Cre}. To model Plp-deletion only in neurons, we interbred female $Plp^{flox/flox}$ with male $Plp^{flox/Y}*Nex^{Cre/WT}$ mice (also termed $NeuroD6^{Cre}$ mice) (Goebbels et al., 2006). We obtained male mice of the genotype $Plp^{flox/Y}*Nex^{Cre/WT}$ and $Plp^{flox/Y}$ control mice. Nex/NeuroD6 is a member of the NeuroD family of bHLH transcription factors; in accordance with its cellular expression pattern the $Nex/NeuroD6$ promoter drives expression of Cre in most neocortical and hippocampal excitatory projection neurons and their immediate progenitors but not in glial cells (Belvindrah et al., 2007; Bormuth et al., 2013; Brinkmann et al., 2008; Goebbels et al., 2006; Li et al., 2013; Schwab et al., 1998; Wu et al., 2005). Importantly, genotyping PCR confirmed recombination of the Plp allele by Cre behind the Nex/NeuroD6 promoter **(Figure 9 e)**. We therefore have generated a model for oligodendrocyte-specific deletion of Plp ($Plp^{flox/Y}*Cnp^{Cre/WT}$) and a model for deletion of Plp in those neurons affected in SPG2 ($Plp^{flox/Y}*Nex^{Cre/WT}$). $Plp^{flox/Y}*Nex^{Cre/WT}$ and $Plp^{flox/Y}*Cnp^{Cre/WT}$ mice were born at expected frequencies. Visual surveillance of their cage behavior did not reveal spasticity or major impairment of motor capabilities up to an age of at least 6 months (not quantified) similar to previously reported $Plp^{null/Y}$ mice (Griffiths et al., 1998).

We note that Cnp heterozygosity in $Cnp^{Cre/WT}$ mice *per se* causes late-onset neuropathology (Hagemeyer et al., 2012) as in Cnp^{Cre} mice the integration of the open reading frame for Cre into the Cnp locus at the same time results in a Cnp-deficient allele. However, importantly, neuropathology is not yet measureable in $Cnp^{Cre/WT}$ mice at 8 months of age (Hagemeyer et al., 2012), i.e. 2 months older than the age analyzed in the present work. Besides $Plp^{null/Y}$ mice, we also included $Plp^{null/Y}*Cnp^{Cre/WT}$ mice as a more direct control group in the neuropathological analysis.
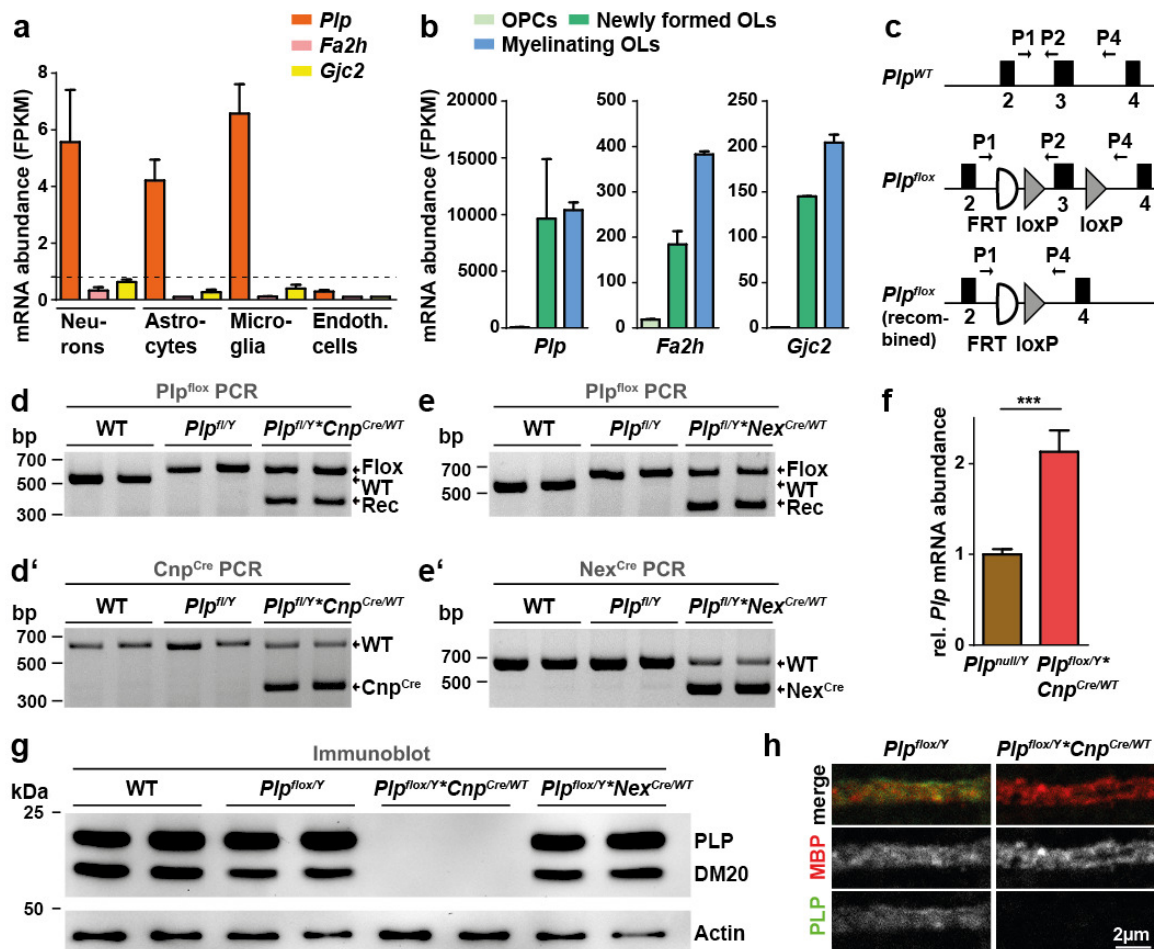
Figure 9: Detection of *Plp* mRNA in neurons imposes cell type-specific analysis

(a) By RNA-Seq of cells immunopanned from mouse cortex, *Plp* mRNA (the SPG2 disease gene) is detected in neurons at low but significant level. The cell-type specific abundance was extracted from (Zhang et al., 2014). Mean with SEM; n=2; stippled line indicates a threshold of 0.8 fragments per kilobase of exon per million fragments mapped (FPKM). For comparison mRNA-abundance of *Fa2h* and *Gjc* (mutated in SPG35 and SPG44, respectively) is below threshold. Note that neuronal *Plp* expression was previously reported in several publications (see **Table 1**). **(b)** Expectedly, the same dataset shows that *Plp*, *Fa2h* and *Gjc* mRNAs are highly abundant in oligodendrocytes. Mean with SEM; n=2. **(c)** Targeting scheme for the conditional inactivation of the *Plp* gene. Exon 3 of the *Plp*^flox allele is flanked by loxP sites for Cre-mediated recombination. Positions of PCR primers (P1, P2, P4) are indicated. **(d-e)** Genomic PCR of DNA isolated from mouse brains at postnatal day 21 detects the *Plp*^WT allele (591 bp product of P1 and P2), the non-recombined *Plp*^flox allele (683 bp product of P1 and P2) as well as the recombined *Plp*^flox allele (519 bp product of P1 and P4). Note that recombination of the *Plp*^flox allele is observed after expression of Cre under control of the oligodendroglial *Cnp* promoter **(d)** or the neuronal *Nex* promoter **(e)**. **(d'-e')** Genomic PCR of brain DNA detecting the *Cnp*^Cre **(d')** or *Nex*^Cre **(e')** allele. **(f)** qRT-PCR to determine the abundance of *Plp* transcripts in mouse brains at postnatal day 75. Note that *Plp* mRNA is more abundant in *Plp*^flox/Y*Cnp^Cre/WT compared to *Plp*^null/Y mice, probably reflecting non-oligodendroglial expression. Mean with SEM; n=4-6; two-tailed unpaired t-test; p<0.001 (***). **(g)** Immunoblot of mouse brains homogenized at postnatal day 21. PLP/DM20 was virtually undetectable in *Plp*^flox/Y*Cnp^Cre/WT brains. Actin was detected as a loading control. **(h)** Confocal microscopic analysis of mouse brains immunolabeled at age 26 weeks detects intense MBP labeling (red) as exemplified for a single internode in the cortex. PLP-immunolabeling (green) essentially co-distributed with MBP in *Plp*^flox/Y mice but was virtually undetectable in *Plp*^flox/Y*Cnp^Cre/WT mice. OL=Oligodendrocyte; OPC=Oligodendrocyte progenitor cell. Figure taken from (Luders et al., 2017).

6.1.3. PLP is abundant in oligodendrocytes

To test the abundance of *Plp* mRNA in *Plp*$^{flox/Y}$*Cnp*$^{Cre/WT}$ compared to *Plp*$^{null/Y}$ mice, we performed qRT-PCR of brain lysate from mice sacrified at postnatal day 21. We observed a higher abundance of *Plp* mRNA in the brains of *Plp*$^{flox/Y}$*Cnp*$^{Cre/WT}$ mice (**Figure 9 f**), which may reflect a low but significant non-oligodendroglial expression of the *Plp* gene. To test if the abundance of PLP in the brain is altered upon deletion of the *Plp* gene in neurons or oligodendrocytes, we subjected brain lysate from mice sacrified at postnatal day 21 to immunoblot analysis. By immunoblotting, PLP was virtually undetectable in the brains of *Plp*$^{flox/Y}$*Cnp*$^{Cre/WT}$ mice whereas it appeared unchanged in *Plp*$^{flox/Y}$*Nex*$^{Cre/WT}$ mice (**Figure 9 g**). By immunohistochemistry PLP co-labeled with MBP, a marker of compact myelin (Nawaz et al., 2013) in *Plp*$^{flox/Y}$ mice. In *Plp*$^{flox/Y}$*Cnp*$^{Cre/WT}$ mice, MBP labeling appeared unchanged, but PLP was virtually absent (**Figure 9 h**). Both experiments suggest that PLP is abundant in oligodendrocytes, and PLP expressed is either not detected with our method or overshadowed by the high abundance of PLP in oligodendrocytes.

6.1.4. Neuropathological analysis

To answer whether lack of PLP from oligodendrocytes or neurons is responsible for the pathology in SPG2, we evaluated the neuropathology in our newly established models. The neuropathology described in *Plp*$^{null/Y}$ mice, which represent a model of SPG2, includes axonal pathology i.e. axonal spheroids, microglial activation, astrogliosis and the presence of T cells (de Monasterio-Schrader et al., 2013) We thus analyzed all these features in the brains of *Plp*$^{flox/Y}$*Nex*$^{Cre/WT}$, *Plp*$^{flox/Y}$*Cnp*$^{Cre/WT}$ and control mice by immunohistochemistry. The hippocampal fimbria was used for quantification, as it is a relatively uniform white matter tract through which the long descending axons of Nex/NeuroD6-positive excitatory neurons project (Fernandez-Miranda et al., 2008; Goebbels et al., 2006; Li et al., 2013).

Axonal spheroids

To measure the extent of axonal pathology, we immunolabeled and quantified amyloid precursor protein-immunopositive (APP+) axonal spheroids in the fimbria at the age of 26 weeks (**Figure 10**). In agreement with previous reports, a significant number of axonal spheroids were present in *Plp*$^{null/Y}$ mice (Griffiths et al., 1998; Werner et al., 2013), and their density was further elevated by additional *Cnp* heterozygosity in *Plp*$^{null/Y}$*Cnp*$^{Cre/WT}$ mice (Edgar et al., 2009). When comparing *Plp*$^{null/Y}$*Cnp*$^{Cre/WT}$ and *Plp*$^{flox/Y}$*Cnp*$^{Cre/WT}$ mice the density of axonal spheroids was similar. Strikingly, only few APP+ axonal spheroids were found in *Plp*$^{flox/Y}$*Nex*$^{Cre/WT}$ mice, similarly to *Plp*$^{flox/Y}$ control mice. Together this implies that axonal pathology is entirely caused by oligodendroglial but not by neuronal recombination of *Plp*.
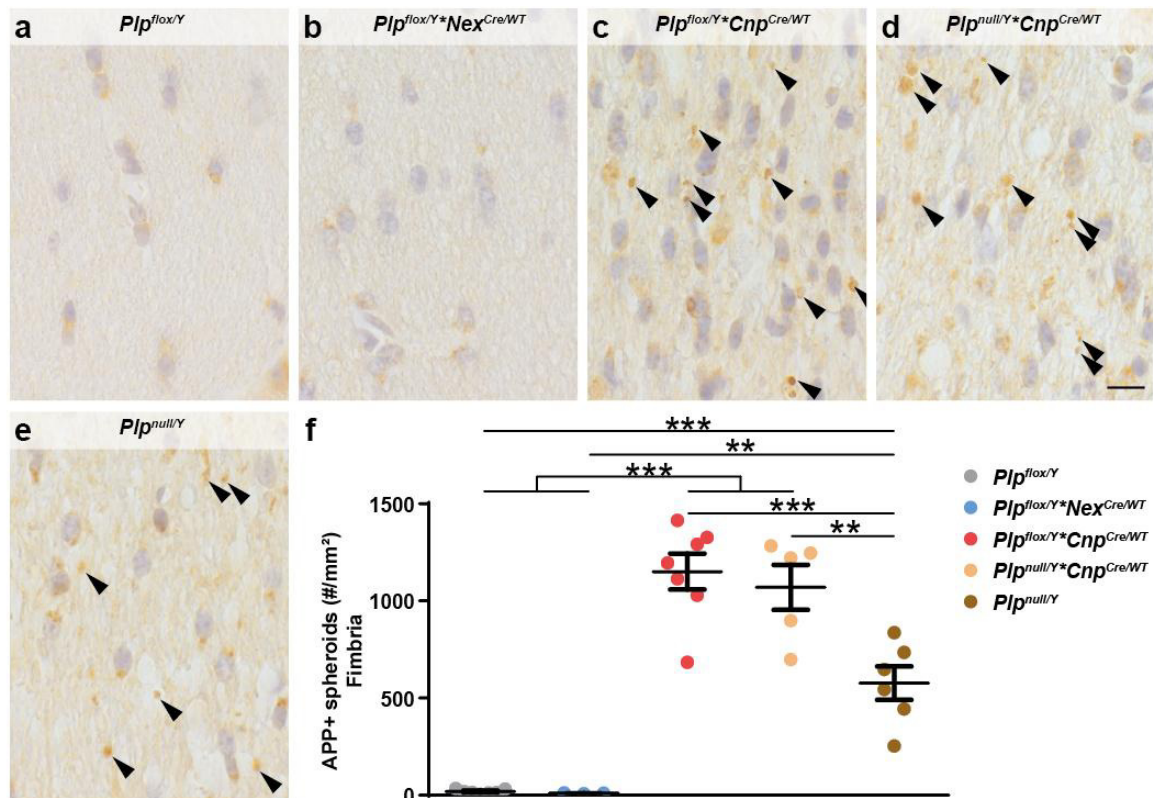
Figure 10: Axonal spheroids in the white matter caused by *Plp*-deletion in oligodendrocytes but not neurons

(a-e) Representative light microscopic images of the hippocampal fimbria of 26-weeks-old mice of the indicated genotypes immunolabeled for amyloid precursor protein (APP) to detect axonal spheroids (black arrowheads). Note that *Plp*^flox/Y^ **(a)** and *Plp*^flox/Y^*Nex^Cre/WT^ **(b)** brains do not display axonal spheroids while oligodendroglial **(c)** or systemic **(d, e)** deletion of *Plp* causes axonal pathology. Axonal impairment is enhanced in mice heterozygous for *Cnp* additional to oligodendroglial **(c)** or systemic **(d)** deletion of *Plp*. Scale bar 10 µm. **(f)** Genotype-dependent quantification of APP-immunopositive (APP+) axonal spheroids in the fimbria. Mean with SEM; n=3-7; one-way ANOVA with Tukey's multiple comparison test; p<0.01 (**) and p<0.001 (***). Figure taken from (Luders et al., 2017).

Microgliosis

As axonal damage is commonly associated with microgliosis, i.e. an increased density and 'activation' of microglial cells (Sasaki, 2016) and this has also been observed in $Plp^{null/Y}$ mice (de Monasterio-Schrader et al., 2013), we analyzed our mice at the age of 26 weeks for this feature. We used antibodies against allograft-inflammatory factor (AIF1/IBA1) (**Figure 11 a-e**) and lysosomal-associated membrane protein 2 (LAMP2/MAC3) (**Figure 11 g-k**) to label microglia and activated microglia, respectively. The relative area of the fimbria occupied by immunostaining was quantified (**Figure 11 f, l**). The signal for MAC3 and IBA1 was enhanced in $Plp^{null/Y}$ mice compared to $Plp^{flox/Y}$ control mice and further elevated by additional Cnp heterozygosity in $Plp^{null/Y}*Cnp^{Cre/WT}$ mice. Importantly, the area of immunopositivity was similar when comparing $Plp^{null/Y}*Cnp^{Cre/WT}$ and $Plp^{flox/Y}*Cnp^{Cre/WT}$ mice. Conversely, the area of immunopositivity was not increased in $Plp^{flox/Y}*Nex^{Cre/WT}$ compared to $Plp^{flox/Y}$ control mice. Thus, axonal damage and microglial activation correlate well as a consequence of oligodendroglial, but not neuronal recombination of Plp. Interestingly, there was a good correlation between IBA1 immunolabeling indicating microglial cell number and MAC3 immunolabeling reflecting microglial activation.

**Figure 11 (next page): Microglial activation after *Plp*-deletion in oligodendrocytes but not neurons**

Representative light microscopic images of the hippocampal fimbria of 26-weeks-old mice immunolabeled for the microglial markers allograft-inflammatory factor (AIF1/IBA1) **(a-e)** and lysosomal-associated membrane protein 2 (LAMP2/MAC3) **(g-k)** and genotype-dependent quantification **(f,l)**. Note that $Plp^{flox/Y}$ **(a)** and $Plp^{flox/Y}*Nex^{Cre/WT}$ **(b)** brains do not display activated microglia while oligodendroglial **(c, i)** or systemic **(d, e, j, k)** deletion of Plp causes microgliosis. Microgliosis is enhanced in mice heterozygous for Cnp additional to PLP-deficiency **(c, d, i, j)**. Scale bar 10 µm. **(f, l)** Genotype-dependent quantification of the relative size of area occupied by IBA1-immunopositive **(f)** or MAC3-immunopositive **(l)** microglia in the fimbria. Mean with SEM; n=3-7; one-way ANOVA with Tukey's multiple comparison test; $p<0.05$ (*), $p<0.01$ (**) and $p<0.001$ (***). Figure taken from (Luders et al., 2017).

Results
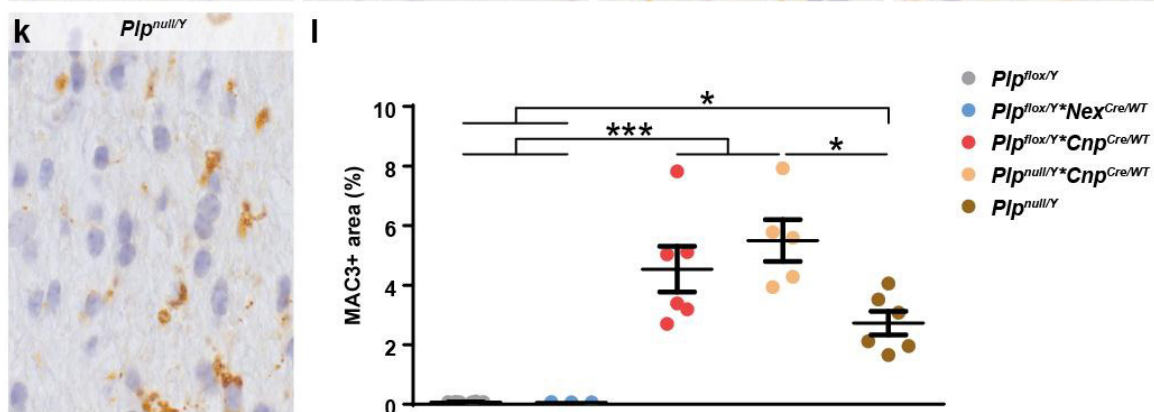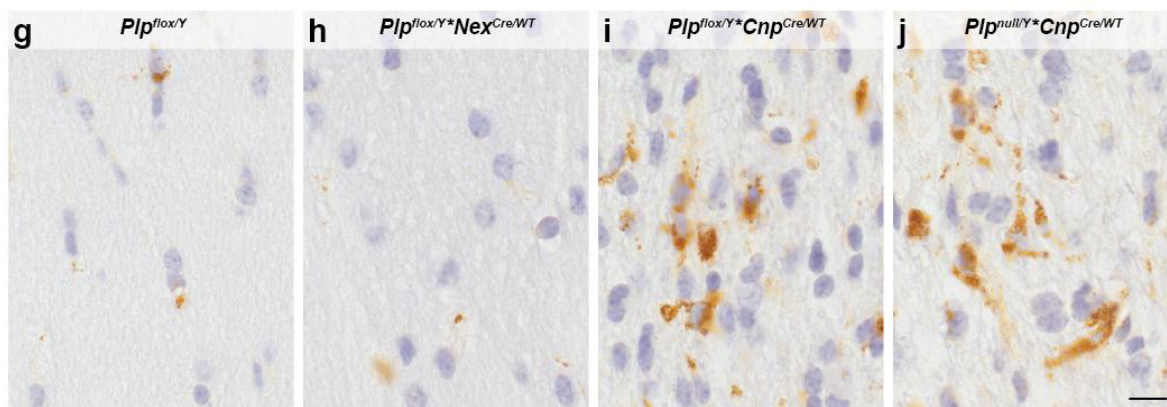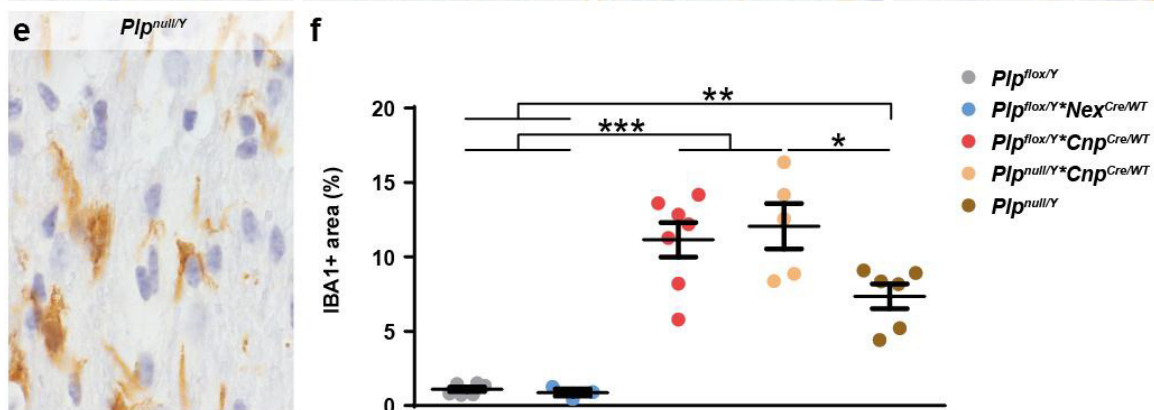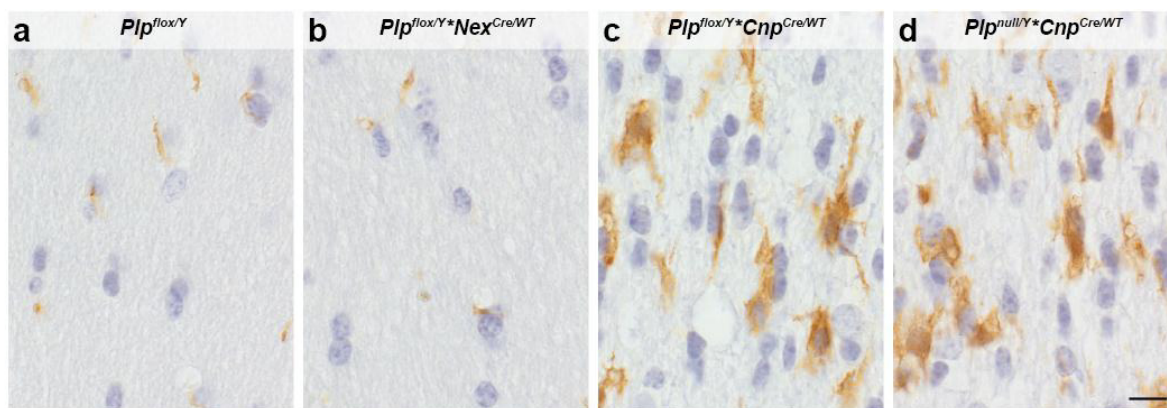
Astrogliosis

The intercellular crosstalk in the diseased brain may include microglia-dependent activation of astrocytes (Liddelow et al., 2017) as well as astrocyte-dependent recruitment or activation of microglia (Jo et al., 2017; Skripuletz et al., 2013). Indeed, both microgliosis and astrogliosis occur in various SPG/PMD patients and mouse models (overview in (Marteyn and Baron-Van Evercooren, 2016)) including the $Plp^{null/Y}$ mouse model of SPG2 (de Monasterio-Schrader et al., 2013). We thus analyzed the amount of astrogliosis by immunolabeling astrocytes using antibodies directed against glial fibrillary acidic protein (GFAP) and measured the relative area of immunopositivity (**Figure 12 a-f**). At the age of 26 weeks we found moderately but significantly enhanced GFAP-labeling in $Plp^{null/Y}$, $Plp^{null/Y}*Cnp^{Cre/WT}$ and $Plp^{flox/Y}*Cnp^{Cre/WT}$ compared to $Plp^{flox/Y}$ control mice, indicative of a mild astrogliosis. Notably, the relative GFAP-positive area was similar in in $Plp^{flox/Y}*Nex^{Cre/WT}$ and $Plp^{flox/Y}$ control mice, indicating that oligodendroglial but not neuronal recombination of Plp causes astrogliosis.

Figure 12: Astrogliosis after *Plp*-deletion in oligodendrocytes but not neurons
(a-e) Representative light microscopic images of the hippocampal fimbria of 26-weeks-old mice immunolabeled for glial fibrillary acidic protein (GFAP) to detect astrocytes. Note that oligodendroglial **(c)** or systemic **(d, e)** deletion of *Plp* causes astrogliosis compared to $Plp^{flox/Y}$ **(a)** and $Plp^{flox/Y}*Nex^{Cre/WT}$ **(b)** brains. Scale bar 10 μm. **(f)** Genotype-dependent quantification of the relative size of area occupied by GFAP-immunopositive astrocytes in the fimbria. Mean with SEM; n=3-7; one-way ANOVA with Tukey's multiple comparison test; $p<0.05$ (*) and $p<0.01$ (**). Figure taken from (Luders et al., 2017).

CD3-immunopositive T cells

Axonal damage and microglial activation are frequently but not always associated with an increased density of T cells (Ransohoff and Brown, 2012; Waisman et al., 2015). In brain tissue of the $Plp^{transgenic-overexpressor}$ mouse model of PMD (Ip et al., 2006; Ip et al., 2012), the $Plp^{null/Y}*PLP^{L30R}$ and $Plp^{null/Y}*PLP^{R137W}$ transgenic mouse models of PMD harboring missense mutations (Groh et al., 2016) and the $Plp^{null/Y}$ mouse model of SPG2 (de Monasterio-Schrader et al., 2013) T cells have been observed. For immunolabeling of T cells we used antibodies directed against CD3 and quantified the density of CD3+ cells in the fimbria at the age of 26 weeks (**Figure 13 a-f**). The increased density of CD3+ cells in $Plp^{null/Y}$ compared to $Plp^{flox/Y}$ control mice did not reach significance but was further elevated by additional Cnp heterozygosity in $Plp^{null/Y}*Cnp^{Cre/WT}$ mice. Importantly, the density of CD3+ T cells was similar when comparing $Plp^{null/Y}*Cnp^{Cre/WT}$ and $Plp^{flox/Y}*Cnp^{Cre/WT}$ mice. Conversely, the density of CD3+ T cells was not increased in $Plp^{flox/Y}*Nex^{Cre/WT}$ compared to $Plp^{flox/Y}$ control mice. Together, axonal damage and the density of T cells correlate in consequence of oligodendroglial but not neuronal recombination of Plp.
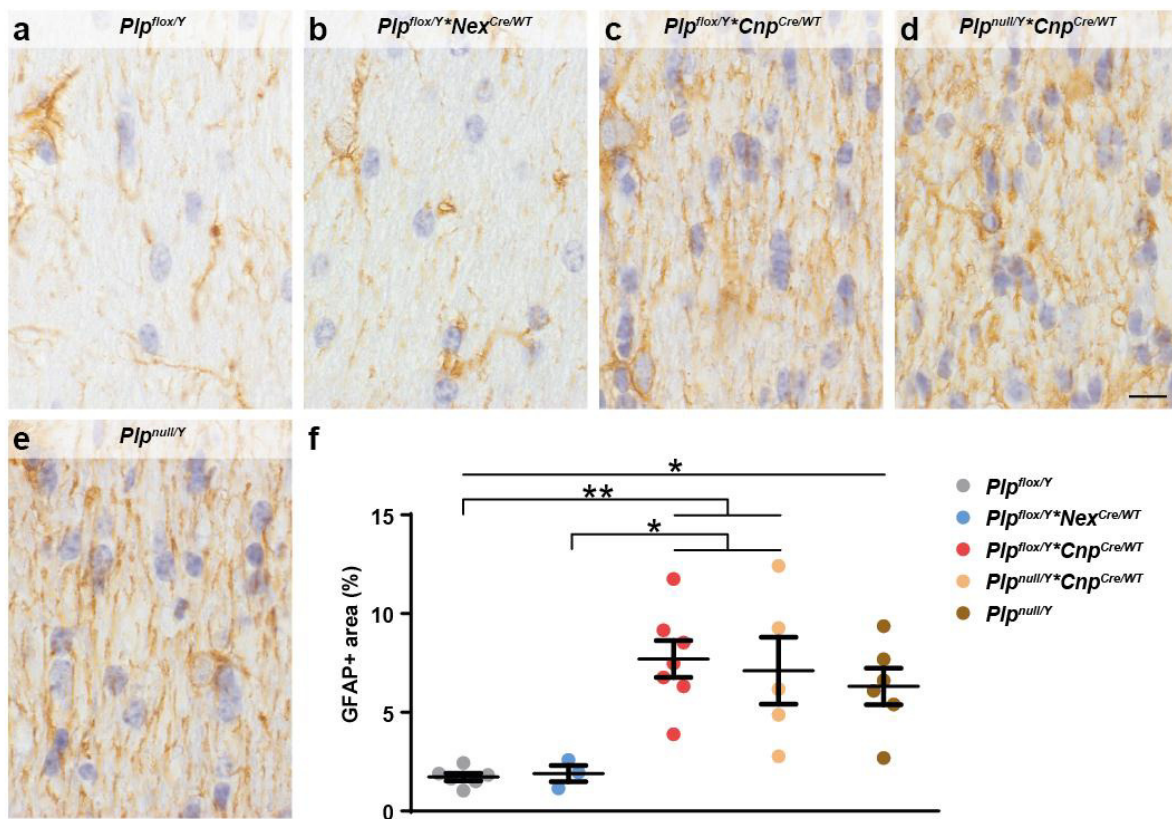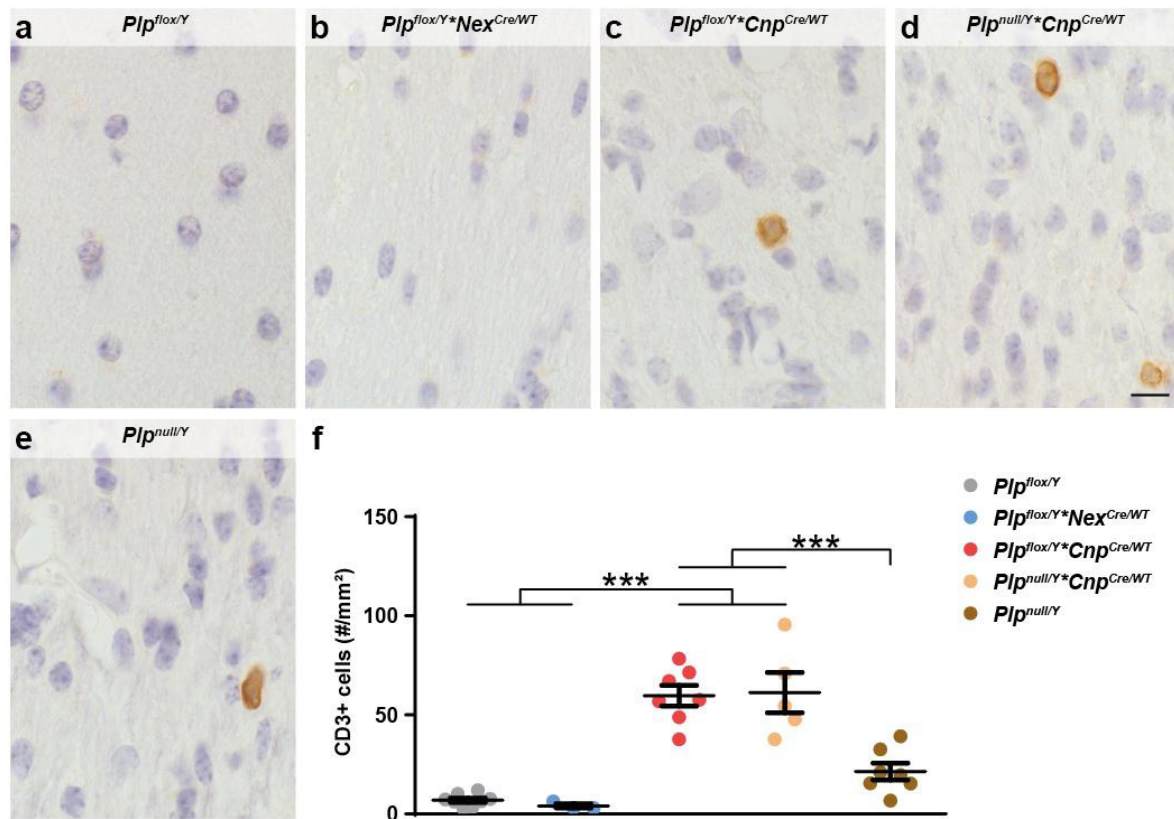
Figure 13: Increased density of T cells after *Plp*-deletion in oligodendrocytes but not neurons
(a-e) Representative light microscopic images of the hippocampal fimbria of 26-weeks-old mice immunolabeled for CD3 to detect T cells. Note that *Plp*^{flox/Y} **(a)** and *Plp*^{flox/Y}*Nex^{Cre/WT} **(b)** brains do not display T cells, while oligodendroglial **(c)** or systemic **(d, e)** deletion of *Plp* causes an increased density of CD3-immunopositive (CD3+) cells. The density of CD3+ cells is enhanced in mice heterozygous for *Cnp* additional to oligodendroglial **(c)** or systemic **(d)** deletion of *Plp*. The apparently increased density of T-cells in *Plp*^{null/Y} mice did not yield significance compared to *Plp*^{flox/Y} mice at the analyzed age. Scale bar 10 µm. **(f)** Genotype-dependent quantification of the number of CD3+ T cells in the fimbria. Mean with SEM; n=3-8; one-way ANOVA with Tukey's multiple comparison test; p<0.001 (***). Figure taken from (Luders et al., 2017).

Axonal spheroids in an independent white matter tract

The observed neuropathology is likely to affect all myelinated axons of long-projecting excitatory neurons in the CNS and to test this concept we evaluated the amount of axonal spheroids in an independent white matter tract. We therefore quantified APP+ axonal spheroids in the corpus callosum at the age of 26 weeks (**Figure 14**). Indeed, similar to the hippocampal fimbria (**Figure 10**) a significant number of axonal spheroids were observed in the corpus callosum of *Plp*^{null/Y} mice. The density of axonal spheroids was further elevated by additional *Cnp* heterozygosity in *Plp*^{null/Y}*Cnp^{Cre/WT} mice and similar between *Plp*^{null/Y}*Cnp^{Cre/WT} and *Plp*^{flox/Y}*Cnp^{Cre/WT} mice (**Figure 14**). Importantly, no APP+ axonal spheroids were found neither in *Plp*^{flox/Y}*Nex^{Cre/WT} mice, nor in *Plp*^{flox/Y} control mice.
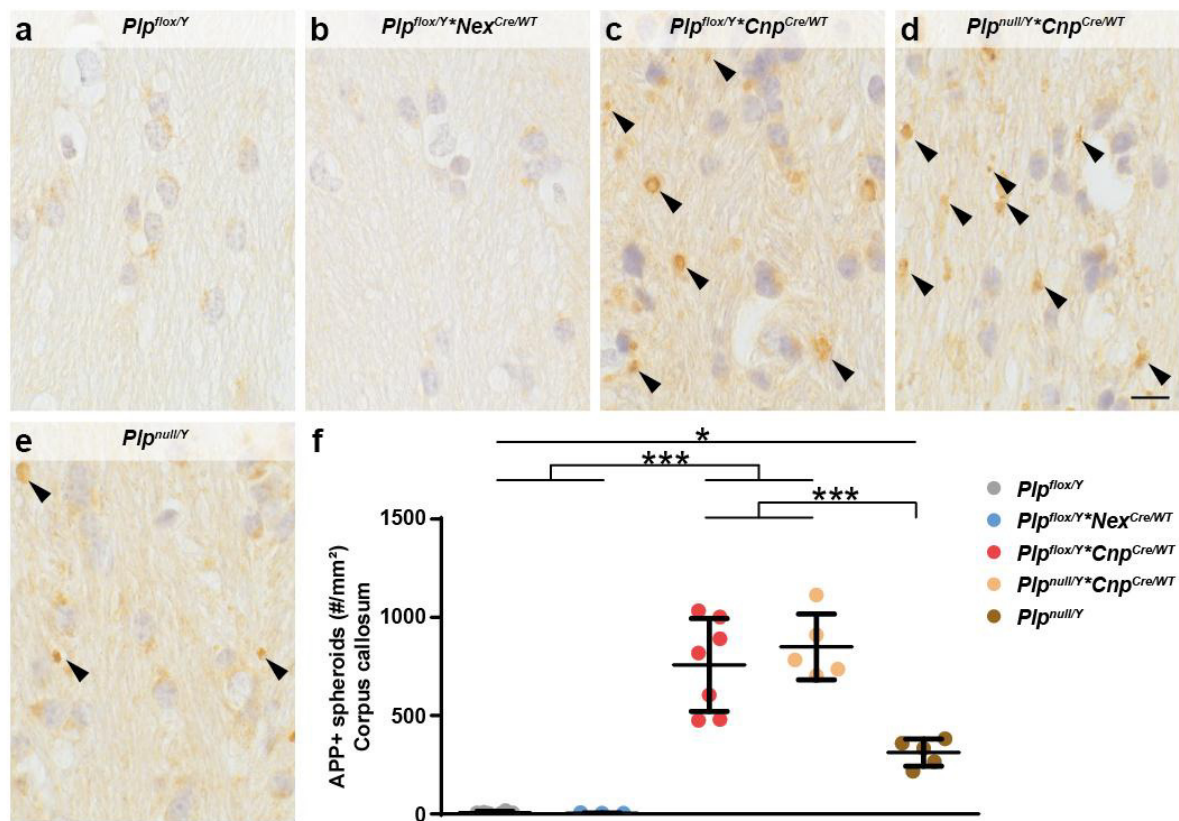
Figure 14: Axonal spheroids in the corpus callosum caused by *Plp*-deletion in oligodendrocytes but not neurons

(a-e) Representative light microscopic images of the corpus callosum of 26-weeks-old mice of the indicated genotypes immunolabeled for amyloid precursor protein (APP) to detect axonal spheroids (black arrowheads). Note that *Plp*$^{flox/Y}$ **(a)** and *Plp*$^{flox/Y}$*Nex$^{Cre/WT}$ **(b)** brains do not show axonal spheroids while oligodendroglial **(c)** or systemic **(d, e)** deletion of *Plp* causes axonal pathology. Axonal impairment is enhanced in mice heterozygous for *Cnp* additional to oligodendroglial **(c)** or systemic **(d)** deletion of *Plp*. Scale bar 10 µm. **(f)** Genotype-dependent quantification of APP-immunopositive (APP+) axonal spheroids in the corpus callosum. Mean with SEM; n=3-7; one-way ANOVA with Tukey's multiple comparison test; p<0.05 (*) and p<0.001 (***). Figure taken from (Luders et al., 2017).

Taken together, we observed increased numbers of axonal spheroids, astrogliosis, microgliosis and increased density of T cells upon deletion of *Plp* in oligodendrocytes, but not upon deletin of *Plp* in neurons. Thus, recombination of *Plp* in oligodendrocytes affects axonal integrity and causes a general neuropathological reaction whereas recombination in excitatory projection neurons does not.

6.2. Axonal pathology precedes T cells in tamoxifen-induced PLP-deficient mice

In the previous part (6.1.), published in (Luders et al., 2017), we have shown that lack of PLP specifically from oligodendrocytes leads to increased numbers of axonal spheroids, accompanied by increased gliosis and infiltration of T cells. Yet, it is unclear whether infiltration of T cells is required for axonal damage in this model or whether it is a secondary effect. We therefore applied tamoxifen-inducible deletion of *Plp* to analyze in which order axonal spheroids, gliosis and elevated number of T cells emerge upon PLP-depletion. This approach also allowed us to draw conclusions about the turnover of PLP within myelin.

6.2.1. *Plp* is successfully deleted by tamoxifen-inducible Cre^{ERT2}

In order to analyze in which order axonal spheroids, gliosis and elevated number of T cells emerge upon deletion of *Plp*, we used a model in which *Plp*-deletion can be induced by tamoxifen injection. Therefore mice harboring a floxed *Plp* allele, which were established as described in chapter 6.1.2. (Luders et al., 2017), were crossbred to mice harboring a tamoxifen inducible *Plp^{CreERT2}* allele (Leone et al., 2003), yielding *Plp$^{flox/Y}$* and *Plp$^{flox/Y}$* *Plp^{CreERT2}* mice. Only male mice wer used for analyses. Both *Plp$^{flox/Y}$* and *Plp$^{flox/Y}$* *Plp^{CreERT2}* males were injected intraperitoneally (i.p.) with tamoxifen dissolved in corn oil at the age of 8 weeks and then analyzed at 16 days, 2, 4, 6, 8, 10, 12 and 16 months post tamoxifen injection (pti) as illustrated in (**Figure 15 a**). In *Plp$^{flox/Y}$* *Plp^{CreERT2}* mice the floxed allele was recomibed after administration of tamoxifen, but not without tamoxifen administration, as tested by standard genotyping (**Figure 15 b**). From here on, *Plp$^{flox/Y}$* mice after tamoxifen injection will be referred to as control mice (Ctrl) and *Plp$^{flox/Y}$*Plp^{CreERT2}* mice after tamoxifen injection will be referred to as induced conditional knockout mice (iKO). To test for successful deletion of the *Plp* gene upon tamoxifen administration, we measured the relative abundance of *Plp* mRNA in Ctrl mice and iKO mice (**Figure 15 c**). *Plp* mRNA was significantly reduced at all three time points analyzed (16 days, 2 and 10 months pti) indicating that the deletion of *Plp* upon tamoxifen administration was successful. The relative mRNA abundance of the second most abundant compact myelin protein in the CNS, myelin basic protein (MBP) was tested as a reference, and was not significantly changed at any of the three tested time points (**Figure 15 d**).
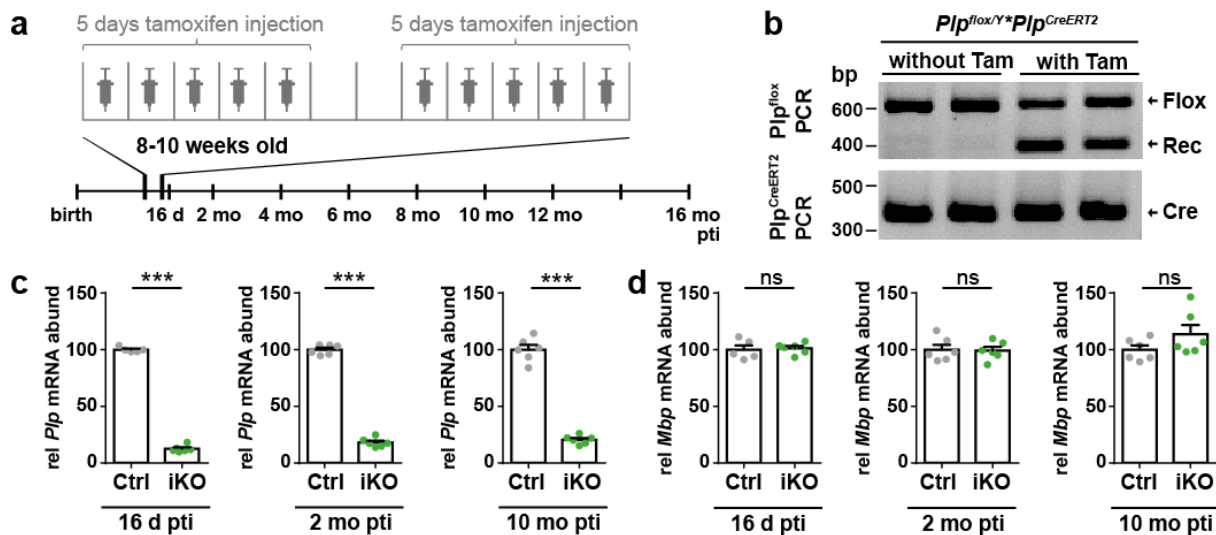
Figure 15: Tamoxifen-inducible *Plp* knockout mouse
(a) Tamoxifen injection scheme for inactivation of the *Plp* gene. *Plp*^flox/Y^ (Ctrl) and *Plp*^flox/Y^*Plp*^CreERT2^ (iKO) male mice were injected i.p. with tamoxifen and analyzed at the indicated time points (16 days, 2, 4, 6, 8, 10, 12 and 16 months pti). **(b)** Genotyping PCR of DNA detects the recombined *Plp*^flox^ allele (462 bp product) after tamoxifen injection, whereas only the non-recombined *Plp*^flox^ allele (683 bp product) is observed without tamoxifen injection. **(c, d)** qRT-PCR to determine the abundance of *Plp* and *Mbp* transcripts in mouse brains. **(c)** Note that *Plp* mRNA is less abundant in iKO mice compared to Ctrl mice at all investigated times points (16 days, 2 and 10 months pti). **(d)** Note that there is no significant difference in *Mbp* mRNA abundance between Ctrl mice and iKO mice at 16 days, 2 and 10 months pti. d=days; mo=months; pti=post tamoxifen injection; bp=base pairs; Tam=tamoxifen; Flox=floxed allele; Rec=Recombined allele; Cre=Cre allele; Ctrl=Control (*Plp*^flox/Y^ mice pti); iKO=induced conditional knockout (*Plp*^flox/Y^*Plp*^CreERT2^ mice pti); Mean with SEM; n=5-6; two-tailed unpaired t-test; p<.001 (***).

6.2.2. Decline of PLP/DM20 in biochemically purified myelin fraction

In order to analyze the decline of PLP and its smaller isoform DM20 from myelin, we biochemically purified a myelin fraction by sucrose-gradient centrifugation after a protocol adapted from Norton and Poduslo (Larocca and Norton, 2007; Norton and Poduslo, 1973) and measured the relative abundance of PLP and DM20 by immunoblotting. We observed the decline of PLP and its smaller isoform DM20 in myelin by an immunoblot series of this biochemically purified myelin fraction. The abundance of PLP and DM20 in iKO mice was compared to age-matched Ctrl mice at 16 days, 2, 4, 6, 8, 10, 12 and 16 months pti (**Figure 16 a**) and quantified (**Figure 16 b, 16 c**). PLP abundance (**Figure 16 b**) in iKO mice declined slowly over time and the decline in the graph resembles a fitted exponential curve. PLP abundance in iKO mice reached on average a non-significantly different 91% compared to Ctrl mice at 16 days pti and a non-significantly different 84% compared to Ctrl mice at 2 months pti. PLP abundance was first significantly different in iKO mice compared to Ctrl mice 4 months pti and at all time points after. PLP abundance reached on average 63% at 4 months, 62% at 6 months, 51% at 8 months, 53% at 10 months, 48% at 12 months and 43% at 16 months pti in iKO mice compared to Ctrl mice. DM20 abundance (**Figure 16 c**) in iKO mice declined slowly over time and the decline resembles a

fitted exponential curve just as for PLP. DM20 level in iKO mice reached on average a non-significantly different 91% compared to Ctrl mice at 16 days pti and a non-significantly different 80% compared to Ctrl mice at 2 months pti. DM20 level was first significantly different in iKO mice compared to Ctrl mice 4 months pti and at all time points after. DM20 abundance reached on average 51% at 4 months, 50% at 6 months, 36% at 8 months, 43% at 10 months, 35% at 12 months and 30% at 16 months pti in iKO mice compared to Ctrl mice. For comparison, we measured the abundance of myelin basic protein (MBP), the second most abundant CNS compact myelin and at ATPase subunit 1a3 (ATP1a3) (**Figure 16 d**). Both were not significantly altered between Ctrl mice and iKO mice at 16 months pti (**Figure 16 e, 16 f**), indicating that the amount of myelin is unaltered by the deletion of *Plp* and the reduction of PLP protein. In a gel-based myelin proteome analysis, a novel myelin protein, NAD+ dependent deacetylase SIRT2, was virtually absent from the myelin proteome of $Plp^{null/Y}$ mice (Werner et al., 2007). It was thus suggested that the supportive effect of PLP for axons, which lacks in SPG2-modeling $Plp^{null/Y}$ mice, may be transduced by SIRT2 by a yet unknown mechanism. We therefore quantified the abundance of SIRT2 in iKO and Ctrl mice by immunoblotting at 4, 8 and 16 months pti (**Figure 16 g, 16 h**). There was neither a significant difference in abundance of both isoforms together at 4 months pti, nor of isoform v2 at 8 months pti. There was a significant reduction of SIRT2 v2 at 16 months pti to 54% on average (**Figure 16 g, 16 h**) and also SIRT2 v1 appeared to be lower in abundance on the immunoblot (**Figure 16 g**; not quantified).

All in all, the abundance of PLP and DM20 in the purified myelin fraction decreased over time. Their decline was very slow and the decay of both proteins followed an exponential curve. The overall amount of myelin appeared to be unaltered, as indicated by the unchanged abundance of MBP at 16 months pti. The most striking effect of *Plp*-deletion on the abundance of other proteins, namely the virtual absence of SIRT2 (Werner et al., 2007), was also observed in iKO mice, however relatively late.
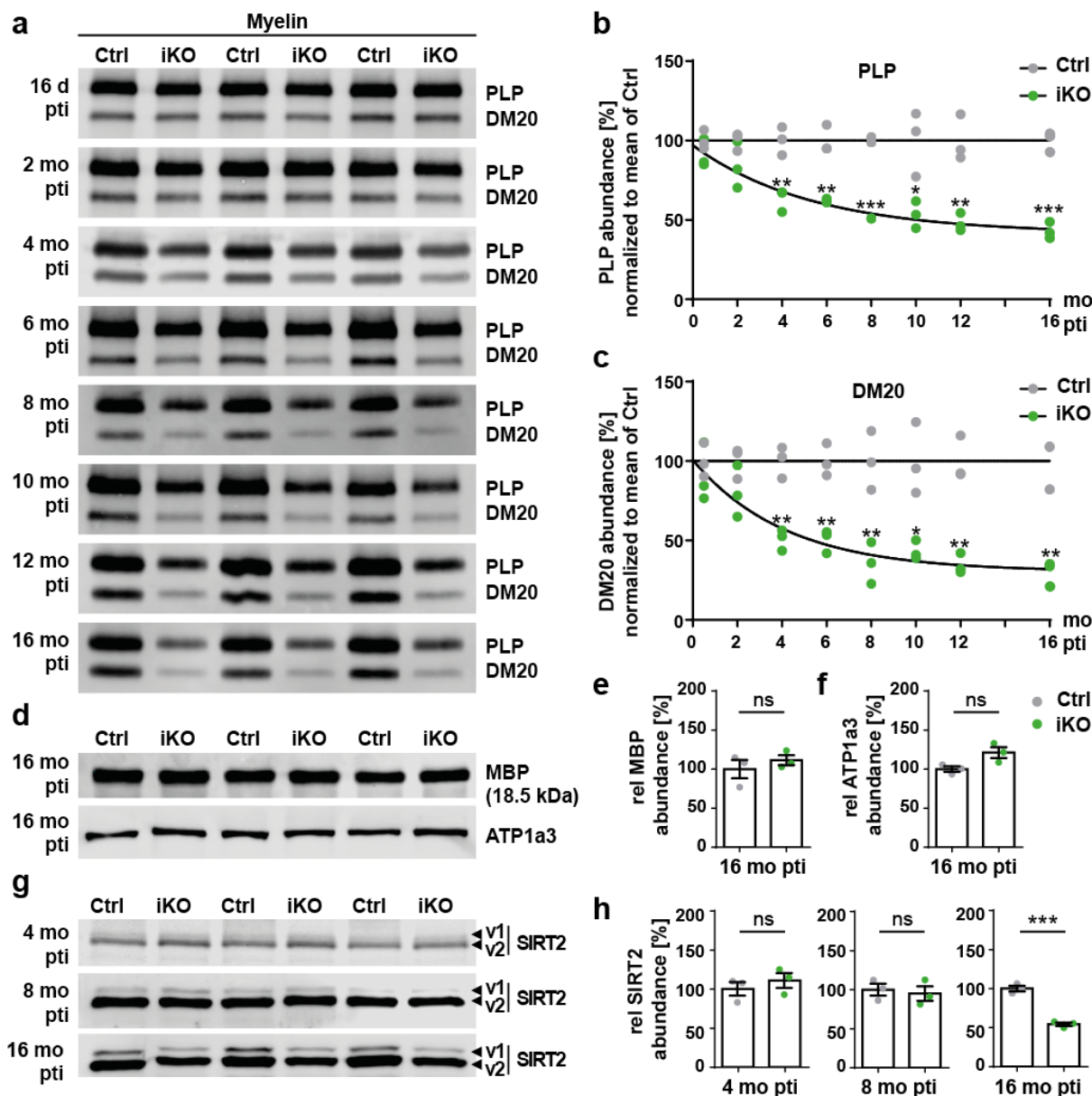
Figure 16: Turnover of PLP/DM20 in CNS myelin

(a) PLP and its smaller isoform DM20 detected by immunoblot in purified myelin of Ctrl and iKO mice at time points 16 days, 2, 4, 6, 8, 10, 12 and 16 months pti. The abundance of PLP **(b)** and DM20 **(c)** in iKO and Ctrl myelin is plotted for all time points (normalized to mean of respective age-matched Ctrl). The decrease over time of both PLP and DM20 resembles a fitted exponential curve with one-phase decay. T-test was performed for each time point individually between iKO mice and age-matched Ctrl mice. **(d)** MBP and ATP1a3 appear unchanged in abundance between Ctrl mice and iKO mice at 16 months pti. Quantification of **(e)** MBP and **(f)** ATP1a3 abundance detects no significant difference between Ctrl mice and iKO mice at 16 months pti. **(g, h)** Abundance of SIRT2 is not significantly altered at 4 and 8 months post tamoxifen injection, but SIRT2 v2 is significantly reduced in the iKO mice 16 months pti compared to Ctrl mice at the same age. d=days; mo=months; pti=post tamoxifen injection; Ctrl=Control ($Plp^{flox/Y}$); iKO=induced conditional knockout ($Plp^{flox/Y}*Plp^{CreERT2}$); Mean with SEM; n=3; two-tailed unpaired t-test; p<.05 (*), p<.01 (**) and p<.001 (***).

6.2.3. Even diminishment of PLP across the myelin sheath

We also investigated the decline of PLP within the myelin sheath by cryo-immuno electron microscopy (**Figure 17**). PLP was labeled with immunogold particles on optic nerve sections from Ctrl mice and iKO mice 4 months pti. The total number of immunogold labeling was reduced to an average of 50% in iKO mice compared to Ctrl mice. In an attempt to distinguish whether PLP is degraded towards the adaxonal or abaxonal side of the myelin sheath, we quantified the amount of immunogold labeling in the inner and outer half of the compact myelin sheath in iKO mice compared to Ctrl mice separately. There was a similar reduction of PLP labeling in the inner half (55% on average; close to significance, p=0.0589) and in the outer half (47% on average, *, p=0.0293) of compact myelin in iKO mice compared to Ctrl mice. Thus, we cannot distinguish whether it is degraded towards the outside or inside of the myelin sheath with this approach. However, we can conclude that PLP in myelin has a high lateral mobility and that upon tamoxifen injection in iKO mice PLP is diminished in the optic nerve myelin on average to about 50% 4 months pti. Thus, it appears to be reduced in the optic nerve to a similar level as in the brain (PLP 62%; DM20 51% in iKO mice compared to Ctrl mice in purified myelin at 4 months pti; **Figure 16 b**).
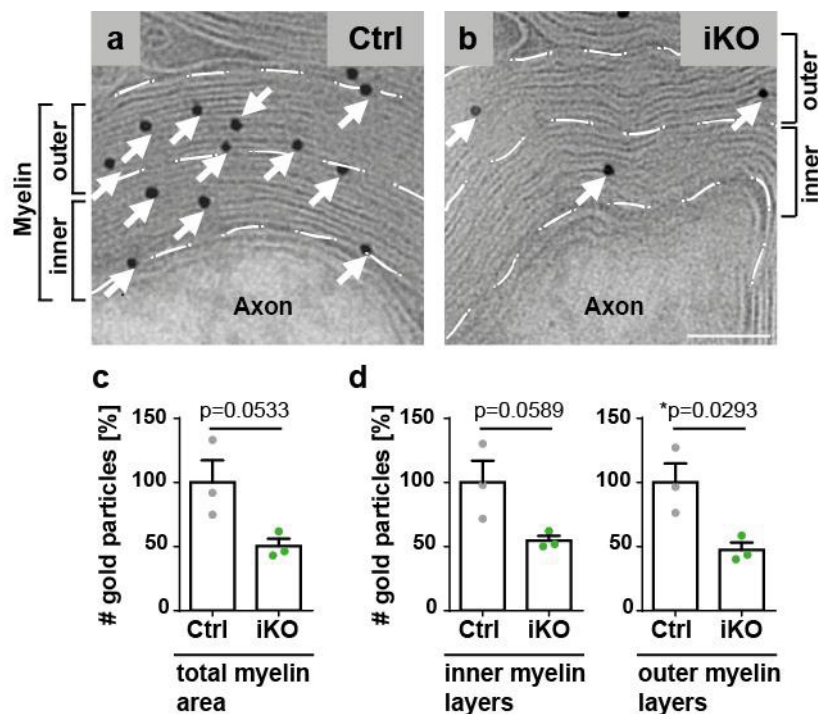
Figure 17: Turnover of PLP in the optic nerve by cryo-immuno electron microscopy
(a, b) Representative images of PLP immunogold labeling in Ctrl mouse **(a)** and iKO mouse **(b)** at 4 months pti. White arrows indicate immunogold particles. Scale bar 75 nm. **(c)** The number of immunogold particles in compact myelin in Ctrl mice and iKO mice normalized to the mean of Ctrl mice. **(d)** Same as in **(c)** but displayed separately for the inner and outer myelin layers. Note that in the inner and outer half myelin layers, immunogold labeling is reduced to a similar level. Ctrl=Control (*Plp*$^{flox/Y}$); iKO=induced conditional knockout (*Plp*$^{flox/Y}$**Plp*^{CreERT2}); Mean with SEM; n=3; two-tailed unpaired t-test; p<.05 (*).

6.2.4. Changes in myelin ultrastucture and axonal pathology upon adult deletion of *Plp*

In order to analyze the ultrastructure of myelin, we used high pressure freezing followed by freeze substitution of optic nerves from iKO and Ctrl mice 10 months pti and analyzed them by electron microscopy. Some ultrastructural abnormalities of myelin have been described in $Plp^{null/Y}$ mice (Duncan et al., 1987; Klugmann et al., 1997; Patzig et al., 2016a). Our tamoxifen-inducible model allowed us to investigate whether ultrastructural abnormalities of myelin and axonopathy also develop upon adult depletion of PLP.

Myelin pathology

Almost all axons (about 90% on average) in Ctrl mice were surrounded by normal appearing myelin, whereas this was only the case for less than 20% in iKO mice (**Figure 18 a**). In contrast, the proportion of non-myelinated axons in iKO mice was with more than 10% significantly higher than in Ctrl mice (**Figure 18 b**), which has been similarly observed in $Plp^{null/Y}$ mice (de Monasterio-Schrader et al., 2013; Yool et al., 2001). Furthermore myelin outfoldings (**Figure 18 c**), a feature of $Plp^{null/Y}$ mice (Patzig et al., 2016a), and swollen inner tongues (myelin comprising a swollen adaxonal compartment) (**Figure 18 d**) occurred significantly more often in iKO mice compared to Ctrl mice. It was furthermore striking, that myelin sheaths of iKO mice appeared looser compared to Ctrl mice. On average 70% of axons in iKO mice were ensheathed by myelin profiles with lamellae splitting and/or cytosolic myelin channels in iKO mice, whereas this is only seen for about 10% of the axons in Ctrl mice (**Figure 18 e**).

Axonal pathology

Interestingly, we found a remarkable number of additional small axonal profiles in association with the inner tongue both in Ctrl mice and iKO mice. There may be a trend to this feature, which we called "axonal sprouting" to being more abundant in iKO mice (**Figure 18 f**). The number of myelin profiles with degenerating and degenerated axons was unchanged in iKO mice (**Figure 18 g**), as also observed in $Plp^{null/Y}$ mice (Patzig et al., 2016a). Importantly, axonal spheroids, the most prominent feature of $Plp^{null/Y}$ mice and SPG2 patients (de Monasterio-Schrader et al., 2013; Garbern et al., 2002; Griffiths et al., 1998; Werner et al., 2013) also developed in iKO mice. Axonal spheroids are thought to form due to a transport defect in axons and presumably lead to Wallerian degeneration of axons (Edgar et al., 2004b). Axonal spheroids were significantly increased in the optic nerve of iKO mice 10 months pti, while they were virtually absent in the optic nerves of Ctrl mice (**Figure 18 h**), indicating that our iKO mice model axonopathy as observed in $Plp^{null/Y}$ mice (Griffiths et al., 1998), $Plp^{null/Y}*Cnp^{Cre/WT}$ mice described in chapter 6.1. (Luders et al., 2017) and SPG2 patients (Garbern et al., 2002).
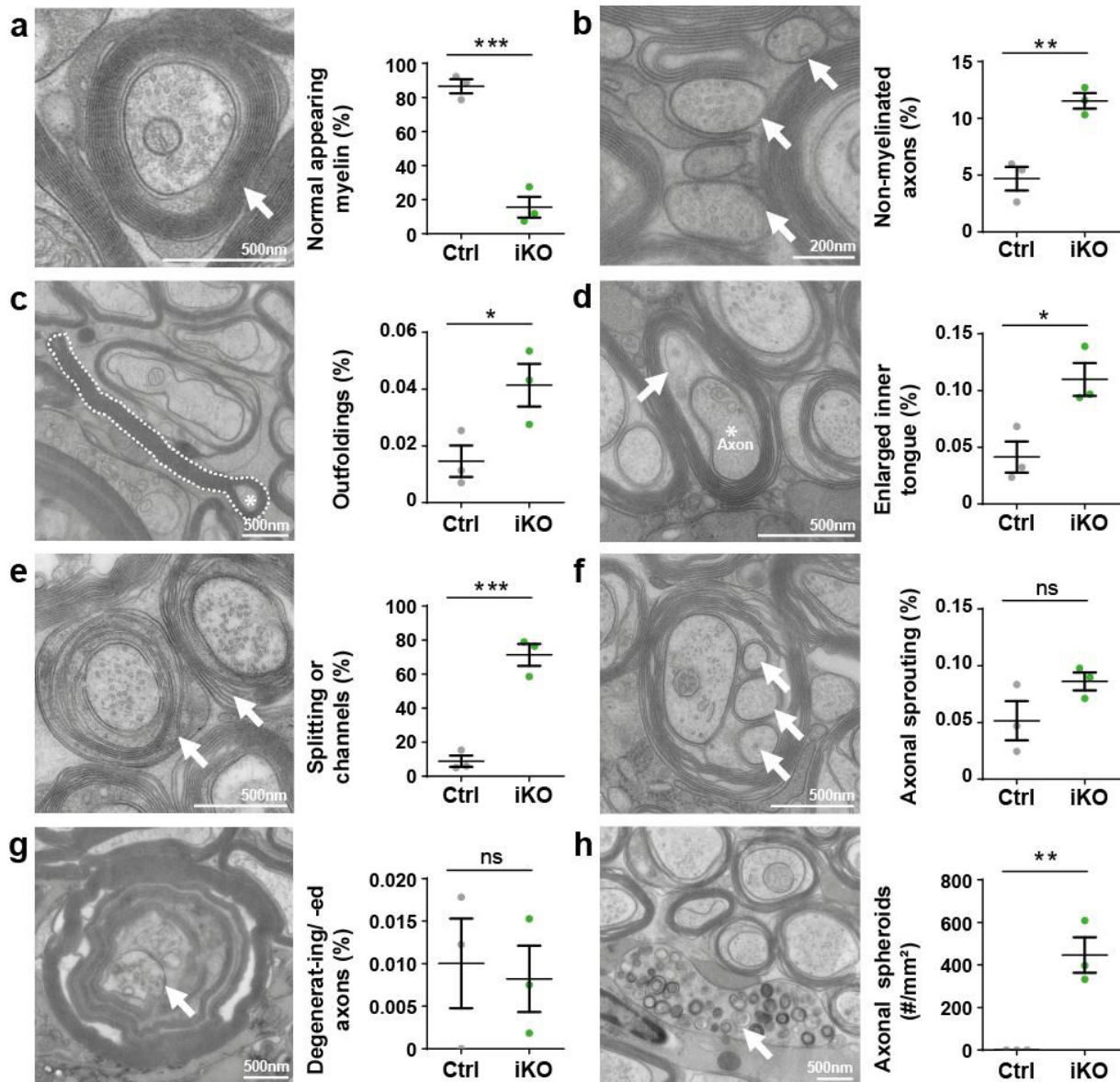
Figure 18: Neuropathological features in the optic nerve upon *Plp*-deletion
(a) Genotype-dependent quantification of axons with normal appearing myelin units. White arrow indicates an axon-myelin unit with normal appearing myelin. **(b)** Quantification of non-myelinated axons (indicated by white arrows). **(c)** Quantification of myelin outfoldings (indicated by white stippled line). Asterik indicates corresponding axon. **(d)** Quantification of enlarged inner tongues (myelin comprising a swollen adaxonal compartment - indicated by white arrow). Asterisk indicates axon. **(e)** Quantification of axons with myelin which displays lamellae splitting or myelinic channels (indicated by white arrow). Note that all features of myelin pathology **(b-e)** are significantly more frequent in iKO mice compared to Ctrl mice. **(f)** Axonal sproutings (indicated by white arrows) are present in both Ctrl mice and iKO mice. **(g)** The relative number of myelin profiles with degenerating and degenerated axons was unchanged between Ctrl mice and iKO mice. A degenerating axon within a myelin-profile is indicated by white arrow. **(h)** Axonal spheroids (marked by white arrow) are significantly more frequent in iKO mice than in Ctrl mice. None were observed in Ctrl mice. **(a-e, g)** Numbers of events are expressed as percent of the number of axons (myelinated and non-myelinated) counted on an 1105 µm² optic nerve area of the corresponding individual animal. **(f)** Numbers of axons with axonal sproutings are expressed in percent of myelinated axons which could be evaluated for this feature on an 1105 µm² optic nerve area. **(h)** Axonal spheroids were counted on at least 18000 µm² per animal and are expressed as number per mm². Ctrl=Control; iKO=induced conditional knockout; Mean with SEM; n=3; two-tailed unpaired t-test; p<.05 (*), p<.01 (**) and p<.001 (***).

6.2.5. Time course of neuropathological events

It has been suggested that the role of neuroinflammation for PMD has been underestimated (Marteyn and Baron-Van Evercooren, 2016) and T cells have been demonstrated to strongly influence axonopathy in PMD models (Groh et al., 2016; Ip et al., 2006; Ip et al., 2012). As we could observe axonal spheroids in the optic nerve at 10 months pti (chapter 6.2.4.), we concluded that neuropathology in iKO mice emerges with time and that iKO mice are a valuable model to better understand the cellular neuropathology in SPG2 by analyzing the time course of neuropathological events. We therefore analyzed Ctrl and iKO mice at several time points pti and quantified axonal spheroids, gliosis and the numbers of T cells in the brain; all of which have been described in SPG2-modeling $Plp^{null/Y}$ mice (de Monasterio-Schrader et al., 2013) and $Plp^{null/Y}*Cnp^{Cre/WT}$ mice described in chapter 6.1. (Luders et al., 2017).

Axonal spheroids

Amyloid precursor protein (APP) was used as a marker to detect axonal spheroids in Ctrl mice and iKO mice at 4, 6-8, 10 and 16 months pti (**Figure 19 a-c**). There was no difference at 4 months pti but at 6-8 months pti the number of APP+ axonal spheroids was significantly increased in iKO mice compared to age-matched Ctrl mice. At later time points the numbers of APP+ axonal spheroids increased further. At 10 and 16 months pti the numbers of APP spheroids were significantly increased on average by about 6-fold and 10-fold in iKO mice compared to age-matched Ctrl mice, respectively. Comparison of wild type and $Plp^{null/Y}$ mice at the age of 6 months (**Figure 19 c**), confirmed significant increase of axonal spheroids observed in $Plp^{null/Y}$ mice (Griffiths et al., 1998; Werner et al., 2013).

Results
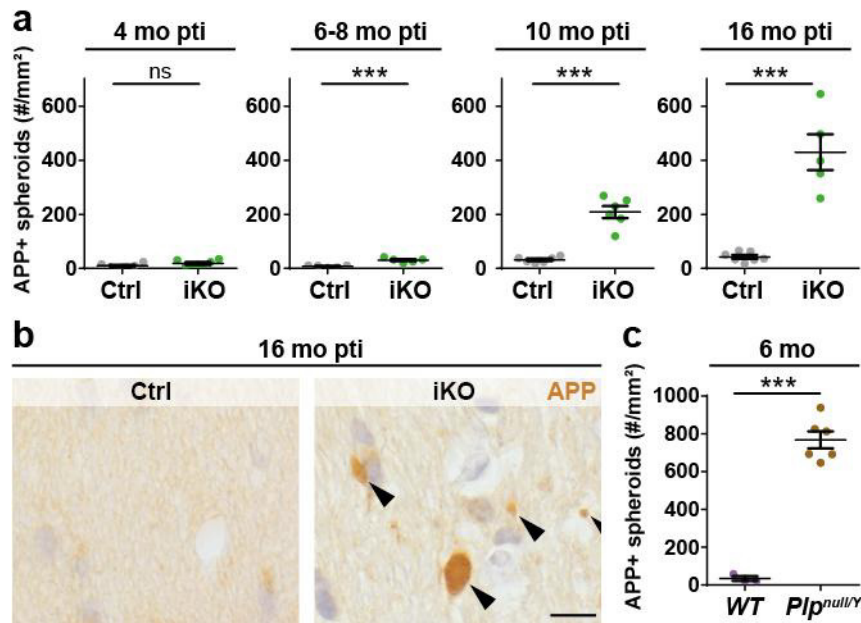
Figure 19: Axonal spheroids in the fimbria upon tamoxifen-induced *Plp*-deletion
(a) Genotype-dependent quantification of axonal spheroids immunopositive for APP in the fimbria at 4, 6-8, 10 and 16 months pti. Note that at 6-8 months pti the number of APP-immunopositive (APP+) axonal spheroids is increased in iKO mice compared to Ctrl mice and that their number further increases at later time points. **(b)** Representative light microscopic images immunolabeled for APP. Scale bar 10 µm. **(c)** For comparison, in fimbriae of 6-months-old $Plp^{null/Y}$ mice the number of APP+ axonal spheroids is significantly increased compared to age-matched wild type mice. mo=months; pti=post tamoxifen injection; Ctrl=Control ($Plp^{flox/Y}$); iKO=induced conditional knockout ($Plp^{flox/Y}*Plp^{CreERT2}$); APP=Amyloid precursor protein; Mean with SEM; n=3-7; two-tailed unpaired t-test; p<.001(***).

Microgliosis and astrogliosis

To test for activation of microglia and astrocytes, which is often observed together with axonal damage (Sasaki, 2016), we quantified the area of the fimbria positive for MAC3 (activated microglia), IBA1 (microglia) and GFAP (astrocytes) at 4, 10 and 16 months pti (**Figure 20**). At 4 months pti, before the onset of axonal spheroids (**Figure 19 a**), there was no significant difference in any of the three markers between the genotypes (**Figure 20 a, 20 d, 20 g**). At 6-8 months pti, when the numbers of axonal spheroids were significantly increased, all three markers were significantly increased in iKO mice compared to Ctrl mice (**Figure 20 a, 20 d, 20 g**). There was a non-significant trend towards increase of IBA1 and GFAP and a significant increase of MAC3 in iKO mice at 10 months pti and significant increase of all three markers at 16 months pti (**Figure 20 a, 20 d, 20 g**). Thus, microgliosis and astrogliosis were detectable at the same time as increased numbers of axonal spheroids in our model (6-8 months pti). We note that at this time (6-8 months pti) on average about 50% of the PLP from the brain was depleted (**Figure 16**; chapter 6.2.2).
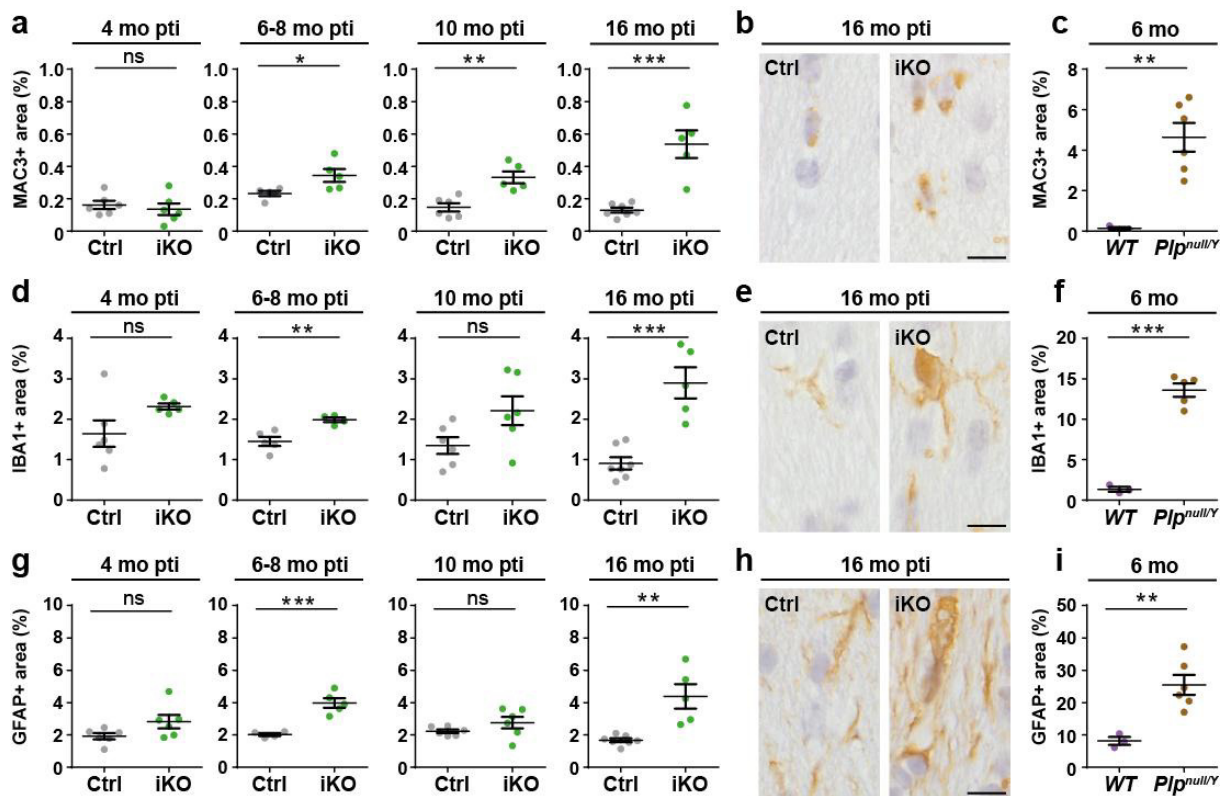
Figure 20: Microglial activation and astrogliosis upon tamoxifen-induced *Plp*-deletion
(a, d, g) Genotype-dependent quantification of the relative area of the hippocampal fimbria immunopositive for the microglial markers MAC3 **(a)** and IBA1 **(d)** and immunopositive for GFAP to detect astrocytes **(g)** at 4, 6-8, 10 and 16 months pti. **(b, e, h)** Representative light microscopic images of the hippocampal fimbria immunolabeled for IBA1 **(b)**, MAC3 **(e)** and GFAP **(h)** in Ctrl mice and iKO mice at 16 months pti. Scale bar 10 μm. **(c, f, i)** Quantification of the relative area of the hippocampal fimbria immunopositive for IBA1 **(c)**, MAC3 **(f)** and GFAP **(i)** in 6-months-old wild type and $Plp^{null/Y}$ mice. Note that the area immunopositive for all three markers is increased in $Plp^{null/Y}$ mice compared to wild type mice and in iKO mice compared to Ctrl mice at 6-8 mo and 16 mo pti. mo=months; pti=post tamoxifen injection; Ctrl=Control ($Plp^{flox/Y}$); iKO=induced conditional knockout ($Plp^{flox/Y}*Plp^{CreERT2}$); IBA1=allograft-inflammatory factor (AIF1/IBA1); MAC3=lysosomal-associated membrane protein 2 (LAMP2/MAC3); GFAP=glial fibrillary acidic protein; Mean with SEM; n=3-7; two-tailed unpaired t-test; p<.01(**) and p<.001(***).

CD3-immunopositive T cells

To better understand their potential contribution to the disease course in SPG2, we also analyzed the number of T cells in the fimbria at 4, 6-8, 10 and 16 months pti. As the role of the immune system has been proposed to be underestimated in PMD (Marteyn and Baron-Van Evercooren, 2016) and T cells have been shown to play a detrimental role for axonal pathology in the $Plp^{transgenic-overexpressor}$ mouse model of PMD (Ip et al., 2006; Ip et al., 2012) and the $Plp^{null/Y}*PLP^{L30R}$ and $Plp^{null/Y}*PLP^{R137W}$ transgenic mouse models of PMD caused by missense mutations (Groh et al., 2016) we wanted to test when and which type of T cells emerge in our iKO model for SPG2. Therefore, the T cell marker CD3 was used and CD3-immunopositive (CD3+) T cells in the fimbria were counted. There was no significant difference between Ctrl mice

and iKO mice at 4 and 6-8 months pti. At 10 months pti there was a significant increase and at 16 months pti a stronger significant increase in T cell number in iKO mice compared to Ctrl mice (**Figure 21 a**). Thus, by 16 months pti the full spectrum of neuropathology observed in *Plp*$^{null/Y}$ mice (de Monasterio-Schrader et al., 2013) including axonal spheroids (**Figure 19 a**), microglial (**Figure 20 a, 20 d**) and astroglial (**Figure 20 g**) activation and increased numbers of T cells (**Figure 21 a**) was observed in iKO mice. Importantly axonal spheroids, microgliosis and astrogliosis were apparent earlier than increased numbers of T cells were detectable, i.e. already at 6-8 months pti (**Figure 19 a, 20 a, 20 d, 20 g**).

6.2.6. Flow cytometric characterization of immune cells

In order to characterize inflammatory cells in more detail, we performed multicolor flow cytometry in collaboration with Dr. Stefan Nessler (Department of Neuropathology, UMG Göttingen). Cells from whole mouse brains (12-17 months pti) were isolated, immunolabeled and separated by FACS (Fluorescence-activated cell sorting). Density plots of cells positive for the markers CD45 or CD11b demonstrate that microglia/macrophages are visibly more numerous in iKO mice compared to Ctrl mice (**Figure 21 d**). Indeed, microglia (CD45^{int} CD11b+) are significantly more abundant in iKO mice (**Figure 21 f**), supporting the quantification of MAC3 staining in the fimbria (**Figure 20 a**). In addition, CD3+ T cells are significantly more numerous in iKO mice (**Figure 21 e**), supporting the quantification of immunohistochemical CD3+ T cell stainings in the fimbria (**Figure 21 a**). To analyze which kind of T cells are observed in our model, we qantified CD4+ and CD8+ T cells. CD8+ cells are the dominant T cell population in both Ctrl mice and iKO mice (**Figure 21 g**). Both CD4+ cells (upper left quadrant) and CD8+ T cells (lower right quadrant) are more numerous in iKO mice compared to Ctrl mice. Quantification shows that the increase in CD8+ T cell number in iKO mice is significant (**Figure 21 h**) whereas there is no significant difference in the number of CD4+ T cells (**Figure 21 i**). Therefore, it seems that CD8+ T cells play a more relevant role in the pathology of SPG2. Among the different subtypes of CD4+ T cells, we also regarded FoxP3-positive regulatory T cells (T$_{regs}$). T$_{regs}$ suppress the function and the proliferation of conventional CD4+ and CD8+ T cells/effector T cells (Mancusi et al., 2018) and thereby may exert a neuroprotective effect. The number of T$_{regs}$ was not significantly altered in iKO mice and overall their abundance is relatively low in both genotypes (**Figure 21 k**). There was no difference in the low abundance of B cells between iKO mice and Ctrl mice (**Figure 21 l**).
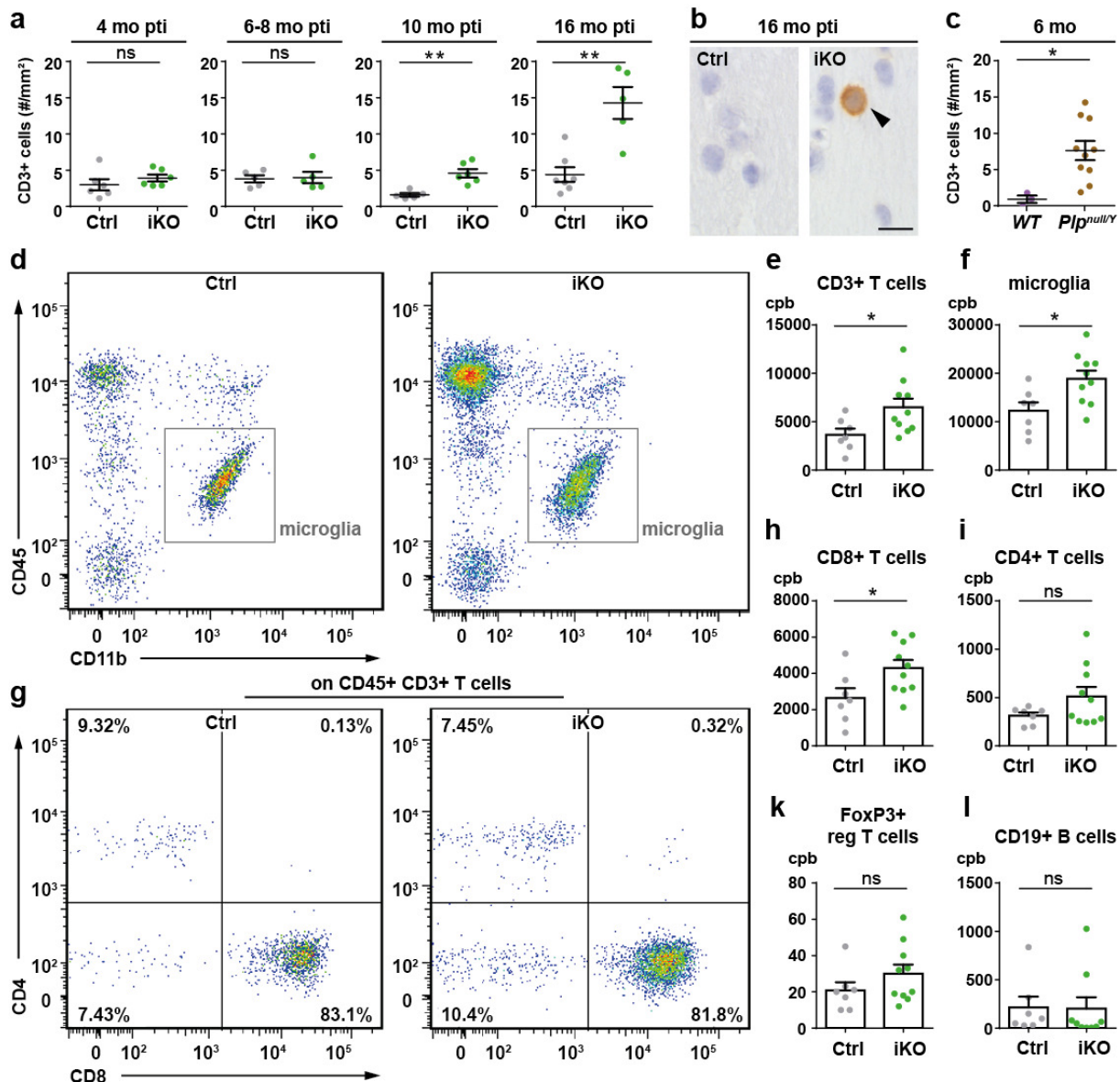
Figure 21: Density and markers of T cells after tamoxifen-induced *Plp*-deletion
(a) Genotype-dependent quantification of the number of CD3-immunopositive (CD3+) T cells in the fimbria at 4, 6-8, 10 and 16 months pti. Note that at 10 and 16 months pti CD3+ T cell numbers are significantly increased in iKO mice compared to Ctrl mice. **(b)** Representative light microscopic images of the hippocampal fimbria immunolabeled for CD3 to detect T cells in Ctrl mice and iKO mice 16 months pti. Scale bar 10 μm. **(c)** Quantification of CD3+ T cells in the fimbria of 6-months-old *Plp$^{null/Y}$* and wild type mice. Mean with SEM; n=3-10; two-tailed unpaired t-test; p<.05(*), p<.01(**) **(d)** FACS analysis of cells isolated from brains of Ctrl mice and iKO mice 12-17 months pti. Representative CD45 and CD11b flow cytometry dot plots with microglial cells (CD45^{int} CD11b+) depicted in grey boxes. **(e, f)** Quantification of CD3+ T cells **(e)** and CD45^{int} CD11b+ microglial cells **(f)**, which are significantly more frequent in iKO mice compared to Ctrl mice. **(g)** CD8+ T cells are the dominant brain T cell subset and their numbers are significantly increased in iKO mice compared to Ctrl mice **(h)**. Numbers of CD4+ cells **(i)**, FoxP3+ T$_{reg}$ cells **(k)** and B cells **(l)** are not significantly changed in iKO mice compared to Ctrl mice. mo=months; pti=post tamoxifen injection; Ctrl=Control (*Plp$^{flox/Y}$*); iKO=induced conditional knockout (*Plp$^{flox/Y}$*Plp^{CreERT2}*); FACS=Fluorescence-activated cell sorting; cpb=cells per brain; CD=Cluster of differentiation; CD3=Cluster of differentiation 3 (marker for T cells); Mean with SEM; n=7-10 two-tailed unpaired t-test; p<.05 (*).

To sum up, our analysis showed that upon deletion of *Plp* in adult mice, axonal spheroids develop not only in the optic nerve (**Figure 18 h**), but also in the fimbria (**Figure 19**). Additionally, we quantified microgliosis, astrogliosis and the numbers of T cells and found that all of these were significantly increased over time upon adult deletion of *Plp*. We thus confirmed with a further technique that not only in the optic nerve (**Figure 18**) but also in a white matter tract of the brain, i.e. the fimbria (**Figure 19, 20, 21**), the full spectrum of neuropathological disease develops, as described in SPG2-modeling *Plp*$^{null/Y}$ mice (de Monasterio-Schrader et al., 2013) and *Plp*$^{null/Y}$*Cnp*$^{Cre/WT}$ mice described in chapter 6.1. (Luders et al., 2017). Thus, our iKO mice can be considered a model for SPG2. This model shows that PLP is crucial for axonal integrity in the adult mouse. Furthermore, we gained insight on the time course of neuropathological events after adult deletion of *Plp*. We observed a significantly increased number of axonal spheroids, microglia and astrocytes in the fimbria of iKO mice compared to Ctrl mice as early as 6-8 months pti (**Figure 19**). T cell numbers in the fimbria were significantly increased two months later (10 months pti). Moreover, we found that CD8+ T cell numbers were significantly increased, whereas the numbers of CD4+ T cells and T_{reg} cells were not significantly altered.

7. Discussion

Correct interaction between neurons and glial cells is crucial for normal functioning of the nervous system. Accumulating evidence for neuronal expression of *Plp* (see **Table 1**) has led to the hypothesis that neuronal dysfunctions in SPG2 patients and respective mouse models may be caused by lack of neuronal *Plp* expression rather than a lack of PLP from oligodendrocytes (Fulton et al., 2011; Jacobs et al., 2003; Sarret et al., 2010). By establishing and analyzing cell type-specific *Plp* knockout mice, we determined that the cause of neuropathological features typical for SPG2 is the lack of PLP from oligodendrocytes and thereby support the concept that oligodendroglial support is crucial for axonal maintenance. Furthermore, we investigated the order of pathological events, including axonopathy and neuroinflammation, upon tamoxifen-induced deletion of *Plp* and conclude that axonopathy initially develops independent from infiltration of T cells in this model. Interestingly, axonal spheroids and gliosis were already detected when the PLP level in CNS myelin was reduced to about 50% compared to Ctrl mice.

7.1. Support for the concept of glia-dependent axonal integrity

The main pathologic feature in SPG2 patients and the corresponding $Plp^{null/Y}$ mouse model is the length-dependent degeneration of axons (de Monasterio-Schrader et al., 2013; Edgar et al., 2004b; Garbern et al., 2002; Griffiths et al., 1998; Gruenenfelder et al., 2011; Petit et al., 2014). Although widely regarded as an oligodendrocyte specific protein, a number of studies have reported expression of *Plp* in a subset of neurons and suggested that the neuronal loss or dysfunction of PLP may be the primary cause for axonal degeneration in SPG2 or other PLP-related disorders (Fulton et al., 2011; Jacobs et al., 2003; Sarret et al., 2010); see **Table 1**. To test this hypothesis, we have specifically deleted *Plp* in oligodendrocytes and neurons by cell type-specific Cre-mediated recombination of the *Plp* gene. We observed that neuronal *Plp* expression appers to be dispensable for axonal integrity, whereas recombination of the *Plp* gene in oligodendrocytes causes the full spectrum of pathology observed in $Plp^{null/Y}$ mice (de Monasterio-Schrader et al., 2013), including axonal spheroids, microgliosis, astrogliosis and infiltration of T cells. We have thus created a novel cell-type specific model for SPG2 and our results support the concept that oligodendroglial support is essential for axonal integrity. Conversely, neuronal *Plp* expression appears to be dispensable for a healthy nervous system.

It is thus very likely that axonal pathology is also caused by the failure of oligodendrocytes to properly support axons in SPG35 and SPG44, in which expression of the causative genes *FA2H* and *GJC2*/*CX47* is restricted to the oligodendroglial lineage in the CNS according to (Zhang et al., 2014) (**Figure 1**). In other forms of HSP the causative genes are not resticted to oligodendrocytes but expressed in several cell types including neurons. Respective proteins are implicated

in functions such as membrane-trafficking or microtubule-associated transport (Salinas et al., 2008). These functions are probably disturbed in neurons and it is likely that impairment of axonal transport leads to axonal degeneration in SPG2. This is likely as especially long axons are affected (Edgar et al., 2004b; Garbern et al., 2002) and long axons are most likely to degenerate upon transport defects (Nave, 2010).Transport defects may emerge due to dysfunctions in neurons themselves, but they may also emerge due to impaired glia-axonal interaction (Funfschilling et al., 2012; Nave, 2010). Thus, it cannot be ruled out that dysfunction of oligodendrocytes or other glial cells also plays a role in the emergence and progression of further HSP types than previously assumed. This becomes even more likely when considering that oligodendrocytes have recently been implicated in classical neurodegenerative diseases such as Rett syndrome (Nguyen et al., 2013), amyotrophic lateral sclerosis (Kang et al., 2013) and Down syndrome (Olmos-Serrano et al., 2016). Analysis of models with cell type-specific mutations would be required to determine the exact contributions of individual cell types to the pathobiology of any neurodegenerative disorder.

7.2. Why may PLP-deficient oligodendrocytes fail to support axons

We have shown that depletion of PLP in oligodendrocytes leads to axonal pathology as observed in $Plp^{null/Y}$ mice and SPG2 patients (Garbern et al., 2002; Griffiths et al., 1998). However, the mechanisms how Plp gene mutations lead to axonal pathology have only been partly resolved. There are some changes in the biogenesis, ultrastructure and composition of PLP-deficient myelin, which we – as far as investigated – also observed in PLP-deficient mice in this study. Thus, the Plp gene may influence axonal survival indirectly, for example by abnormal formation of myelin sheaths. Cytosolic channels and enlarged inner tongues, which we quantified for the first time in a PLP-deficient mouse model, support the concept that trophic support by oligodendrocytes may be altered in PLP-deficient mice.

7.2.1. Ultrastructural changes in PLP-deficient myelin

Moderate structural abnormalities, i.e. condensed intraperiod lines are observed in compact myelin devoid of PLP in mice (Klugmann et al., 1997; Mobius et al., 2008) and rats (Duncan et al., 1987) and PLP is thus viewed as a "molecular strut" to stabilize compact myelin at the intraperiod lines. PLP helps to enrich cholesterol in the compact myelin, by associating with it in the secretory pathway. PLP-deficient mice display less cholesterol, but yet enough to form compact myelin, as the cholesterol-sequestering function of PLP can be partly compensated by another proteolipid M6B (Werner et al., 2013). Further changes in the molecular composition of myelin deficient of PLP include for example a reduction of septins and the virtual absence of the nicotinamide adenine dinucleotide (NAD+)-dependent deacetylase

sirtuin 2 (SIRT2) (Werner et al., 2007). Septins form longitudinal filaments in the adaxonal compartment of mature CNS myelin and thereby stabilize the compact myelin and prevent the formation of myelin outfoldings (Patzig et al., 2016a), another structural feature of $Plp^{null/Y}$ mice, which also developed after tamoxifen-induced deletion of Plp in this study. Yet, it is unclear if and how alterations in the intraperiod line, cholesterol content or outfdoldings would lead to axonal degeneration. Implications of SIRT2 will be adressed in chapter 7.2.2. *In vitro* experiments furthermore suggested that products of the Plp gene may modulate oligodendrocyte-dependent axonal survival directly (Boucher et al., 2002).

7.2.2. A potential role of the deacetylase SIRT2?

Sirtuin enzymes are expressed by different tissues and cell types and are involved in various biological processes including aging, inflammation, apoptosis and cellular metabolism (Michan and Sinclair, 2007; Yang et al., 2000). In the CNS SIRT2 is expressed by various cell types, including oligodendrocytes, where it has been observed in the cytoplasm, in compacted and non-compacted myelin by cryo-immuno electron microscopy (Li et al., 2007; Werner et al., 2007). Since the deacetylase SIRT2 was the only protein virutally absent in the myelin proteome of $Plp^{null/Y}$ mice, it was suggested that PLP may exert a supportive function for axons via SIRT2 (Werner et al., 2007). The function of SIRT2 is yet not understood, possible targets include transcription factors, alpha-tubulin, Glycogen synthase kinase 3 and histones (Bao et al., 2014; North et al., 2003; Sarikhani et al., 2018; Snider et al., 2013; Vaquero et al., 2006; Wang et al., 2007; Wang and Tong, 2009). Similar to $Plp^{null/Y}$ mice, in which myelin is virtually devoid of SIRT2 (Werner et al., 2007) we also observed a decrease of SIRT2 in myelin by immunobloting experiments upon adult deletion of PLP. It is surprising that both isoforms of SIRT2 appear reduced in our model (at least at 16 months pti) since only isoform v2 is enriched in myelin (Werner et al., 2007). In $Plp^{null/Y}$ mice only isoform v2 was virtually absent, and v1 was unaltered in abundance. Furthermore, it was surprising that the decrease of SIRT2 appeared relatively late, i.e. at 16 months pti. PLP is required for the transport of SIRT2 into the myelin compartment (Werner et al., 2013; Zhu et al., 2012) and the turnover of SIRT2 is even faster than the turnover of PLP (Toyama et al., 2013). Maybe the transport of SIRT2 into the myelin compartment only breaks down after PLP falls below a certain a "threshold". Hypothetically, if a vesicular pool of PLP is responsible for transporting SIRT2 into compact myelin, this should be exhausted quickly upon Plp-deletion. If there is a "cirulating pool" of PLP, i.e. vesicles with PLP budded from the compact myelin are send out to sequester SIRT2, the idea of a PLP "threshold" needed for transport of SIRT2 into compact myelin would be more plausible. Altogether the observation that decrease of SIRT2 was only evident months after the onset of axonal degeneration implies that PLP exerts its protective function for axons independent from SIRT2 in agreement with unpublished genetic studies (Kusch et al., unpublished studies).

7.2.3. Potential adhesive function of PLP may be lost

In high pressure frozen optic nerves of PLP-deficient mice (10 months pti), we observed a high number of myelin profiles with lamellae splitting. PLP is not a classical adhesion protein, yet adhesive properties of PLP are under debate. So far, mild adhesive properties of PLP have been observed at least *in vitro* (Bakhti et al., 2013; Bizzozero et al., 2001; Bizzozero and Howard, 2002), but *in-vivo* proof has remained problematic due to aretefacts of conventional aldehyde fixation (Mobius et al., 2008). Conventional fixation of samples for electron microscopy is based on fixation with aldehydes, which stabilizes tissue by connecting proteins with each other. Since in $Plp^{null/Y}$ mice, the most abundant compact myelin protein PLP is lacking, aldehyde fixation cannot stabilize the tissue of $Plp^{null/Y}$ mice to the same extent as in wildtype mice, which makes lamellae prone to split. Lamellae splitting in conventional aldehyde fixed optic nerves of $Plp^{null/Y}$ mice has thus rather been attributed to non-optimal fixation of the tissue due to the lack of PLP protein in the myelin (Mobius et al., 2008). To circumvent this problem protocols to improve ultrastructual preservation of myelin by cryofixation, i.e. high pressure freezing and freeze substitution, have been developed - reviewed by (Mobius, 2009). By rapidly freezing tissue, cross-linking of proteins is not needed; only actual adhesive properties within the tissue play a role for its preservation. Upon careful tissue handling, split myelin lamellae were not obvious in high pressure frozen optic nerves of $Plp^{null/Y}$ mice in (Mobius, 2009). In our analyisis, we observed a higher number of myelin profiles with lamellae splitting in PLP-deficient mice. This is probably due to a reduced adhesion of lamellae in the PLP-deficient mice, which results in easy splitting upon not quite optimal handling. In this study we provide the first quantification of lamellae splitting and cytosolic channels in myelin on high pressure frozen optic nerves of PLP-deficient mice. Our results suggest that lamellae splitting may indeed indicate an adhesive function of PLP *in vivo*, as suggested from *in vitro* experiments (Bakhti et al., 2013; Bizzozero et al., 2001; Bizzozero and Howard, 2002). The lack of an adhesive PLP function may be responsible for the presence of more cytosolic channels through PLP-deficient myelin.

7.2.4. Indications for impaired trophic support

Besides splitting of lamellae, we also observed cytosolic channels in the compact myelin sheath and more enlarged inner tongue processes in high pressure frozen optic nerves of iKO mice (10 months pti). The inner tongue is the most distal process of the oligodendrocyte. Together with the non-compacted adaxonal and abaxonal myelin compartment and paranodal loops it forms a cytoplasm-filled continuum with the olidogendrocyte soma (Ransom et al., 1991) and may provide a compartment for direct communication between axon and oligodendrocyte. Cytosolic channels may provide a cytoplasmic route through the compact myelin sheath, mainly during development. They are stabilized by CNP, which counteracts membrane compaction

by MBP (Snaidero and Simons, 2017) and a large fraction of them disappears by postnatal day 21 (Snaidero et al., 2014). Recently, cytosolic channels have been illustrated in high pressure frozen optic nerves of adult $Plp^{null/Y}$ mice (Mobius et al., 2016). The channels have probably not been so well visible in tissue of $Plp^{null/Y}$ mice by previous conventional aldehyde fixation. In our analysis, cytosolic channels were not always distinguishable from lamellae splitting and often both features appeared together in the same myelin sheath, so both features were quantified together. As a result, our analysis does not provide ultimate proof but suggests that formation of cytosolic channels may be increased in PLP-deficient mice. They occurred in different sizes and were sometimes filled with organelles. It may be possible that they occur in PLP-deficient mice due to the lack of an adhesive function of PLP (chapter 7.2.3.). In the PNS cytoplasmic channels, i.e. Schmidt-Lantermann incisures, probably provide transport routes for vesicles and molecules through compact myelin, e.g. to the adaxonal myelin layer (Nave and Werner, 2014). Similarly, cytoplasm-rich channels in the CNS may connect the oligodendroglial cell body with the inner adaxonal tongue of myelin. It is likely that in the CNS the presence of cytosolic channels affects the intracellular transport routes between oligodendroglial cell body and the inner tongue of myelin and thus the transport of small metabolites that are exchanged between oligodendrocytes and axons, thereby providing trophic support (Frühbeis et al., 2013; Funfschilling et al., 2012; Lee et al., 2012; Nave, 2010; Nave and Werner, 2014; Snaidero et al., 2017). In this study, we also quantified for the first time the number of enlarged cytoplasm-filled inner tongues in a PLP-deficient mouse model. Our observation that enlarged inner tongues were were more numerous in PLP-deficient mice, may be an indication for impaired import or export of molecules at the glia-axonal contract site in PLP-deficient mice. Together, higher abundance of cytoplasmic channels and enlarged inner tongues may reflect an altered transport or exchange of molecules to trophically support axons at the internode.

7.2.5. Lack of trophic support may cause axonal degeneration

In order to maintain the ionic potential needed for transmission of action potentials along axons ($Na^+ + K^+$) ATPases, which are present along the entire internodal membrane (McGrail et al., 1991; Young et al., 2008), exchange Na^+ and K^+ ions and thereby consume ATP. It is unlikely that ATP is produced by glycolysis along the entire length of an axon. Since glycolyic enzymes move by slow anterograde axonal transport (Brady and Lasek, 1981; Oblinger et al., 1988), they would probably be completely degraded by the time it would take them to reach the distal end of a 1 m long axon for example (Nave, 2010). In order to reach their high energy demands, axons probably rely on energy supply, yet the surface of myelinated axons is largely isolated from metabolic exchange with the extracellular milieu. Metabolic coupling of oligodendrocytes and axons may be a mechanism to counteract the isolation of myelinated axonal stretches to the extracellular milieu (Funfschilling et al., 2012; Lee

et al., 2012; Nave, 2010; Nave and Werner, 2014). According to the model in (Funfschilling et al., 2012) oligodendrocytes import glucose through glucose 1 transporters (GLUT1) and possibly via astrocytes, and metabolize it by glycolysis. The produced lactate/ pyruvate may be transported to the myelinated axon via monocarboxylic acid transporters (MCT1, MCT2) and this can be used for energy production, i.e. ATP in axonal mitochondria. (Lee et al., 2012) support this concept by demonstrating that disruption of the oligodendrocytic MCT1 transporter leads to axonal damage and neuron loss.

Another way how oligodendrocytes may directly support axons could be a signal-mediated transfer of exosomes from oligodendrocytes to neurons. (Frühbeis et al., 2013) show that oligodendrocytes secrete exosomes upon stimulation by the neurotransmitter glutamate. These exosomes carry specific protein and RNA cargo and can be retrieved by neurons in vivo. Since the viability of neurons cultured under stressed conditions is improved when they are supplied with oligodendroglial exosomes, the study suggests that oligodendroglial exosomes contribute to neuronal integrity.

Impaired trophic support by oligodendrocytes may lead to reduced ATP levels in myelinated axons (Trevisiol et al., 2017), damage axonal mitochondria (Yin et al., 2016) and impair fast anterograde and retrograde axonal transport, which requires ATP (Gibbs et al., 2015). Impaired axonal transport in $Plp^{null/Y}$ mice (Edgar et al., 2004b) may ultimately lead to accumulation of organelles and vesicles similar to a "traffic jam" so that axonal spheroids are formed (Garbern et al., 2002; Griffiths et al., 1998; Gruenenfelder et al., 2011).

7.2.6. How trophic support by PLP-depleted oligodendrocytes is impaired remains to be determined

Impaired metabolic axonal support by PLP-depleted oligodendrocytes may lead to the formation of axonal spheroids. Yet, it is unclear whether and how exactly increased numbers of cytosolic channels and enlarged inner tongues in oligodendrocytes relate to impaired metabolic support by oligodendrocytes. Increased numbers of cytosolic channels and enlarged inner tongues may result from a "traffic jam" of metabolites, which cannot be properly passed on to axons via MCT1 and MCT2 transporters. Increased numbers of cytosolic channels and enlarged inner tongues may also be indicative of increased transport of trophic molecules within myelin, which could be an attempt of oligodendrocytes to compensate impaired axonal energy homeostasis. Also the abundance of MCT1 is increased in $Plp^{null/Y}$ mice (Kathrin Kusch, unpublished data), indicating that transport of metabolites may be impaired. Yet it is unclear, why and how axonal energy homeostasis may be impaired in $Plp^{null/Y}$ mice. Our study implies that axonal energy homeostasis is not impaired due to potential lack of PLP from neurons, since we observed that lack of

PLP from neurons alone does not cause neuropathology. Hypothetically, the myelin sheath may become leaky to ions due to the lack of PLP and thus axons may have a higher ATP demand to keep up their resting potential. Thus, oligodendrocytes may try to compensate for this higher energy demand by increasing the number of cytosolic channels, the size of their inner tongues and the number of MCT1 transporters. Yet, the exact mechanisms how trophic support may be impaired in $Plp^{null/Y}$ mice is not resolved.

7.3. PLP is needed for axonal maintenance in the adult mouse

It may be hypothesized that in $Plp^{null/Y}$ mice the maturation of myelin is impaired, and that impaired axonal support may result from incompletely matured myelin or maybe even a developmental impairment of oligodendrocytes. PLP-deficiency has consequences to oligodendrocyte progenitor cells (OPC), i.e. an impairment of OPC migration (Harlow et al., 2015) and length and orientation of their processes (Harlow et al., 2014) has been observed during remyelination. PLP is not essential for the formation of myelin in general (Klugmann et al., 1997) but some small diameter axons fail to be myelinated in PLP-deficient mice (de Monasterio-Schrader et al., 2013; Yool et al., 2001), thus PLP-deficiency may already have some consequences early, i.e. on migration of OPCs and myelination of small caliber axons. Furthermore, ultrastrucutral changes and changes in protein composition (chapter 7.2.1.) may result from impaired myelin maturation due to the lack of PLP. However, we observed that the same axonal pathology, neuroinflammation and ultrastructural changes of myelin observed in $Plp^{null/Y}$ mice developed after we deleted Plp at the age of 8 weeks, i.e. after successful formation of myelin. This suggests that PLP is not only needed for development and establishment of mature myelin, but also serves a function for long term maintenance in adult mice.

7.4. Does instable myelin favor the emergence of axonal sproutings?

In high pressure frozen optic nerves, we observed some myelin profiles with additional axonal segments, to which we refered to as axonal sproutings. We do not know their function or exact three-dimensinal structure. We think of these sproutings as "fingers" that may be emerging from the initially myelinated axon and extend below its myelin sheath. We did not observe a significant difference, but since there may be a trend to this feature being more abundant in iKO mice. It is tempting to hypothesize that unstable myelin may favor the emergence of these sproutings and that these may contribute to a metabolic imbalance. But so far this is speculative and more detailed analysis and quantification of further mouse models with potentially unstable myelin, e.g. $Plp^{null/Y}$ mice (Klugmann et al., 1997), Cnp^{null} mice (Lappe-Siefke et al., 2003), Mag^{null} mice (Li et al., 1994) and shiverer mice lacking MBP

(Rosenbluth, 1980) would need to be done to investigate this hypothsis. 3D electron microscopy would allow to determine the actual shape of these sproutings. Alternatively, rather than "finger-like" extensions from one axon, an alternative hypothesis may be that several axons are myelinated by one myelin sheath. In this study, we note axonal sproutings as an interesting observation with potential for future evaluation.

7.5. Implications of neuroinflammation

Besides axonal pathology, neuroinflammation, i.e. gliosis and increased numbers of T cells have also been observed in PMD models (Groh et al., 2016; Ip et al., 2006; Ip et al., 2012) and SPG2-modeling $Plp^{null/Y}$ mice (de Monasterio-Schrader et al., 2013) and $Plp^{null/Y}*Cnp^{Cre/WT}$ mice analyzed in chapter 6.1 (Luders et al., 2017). Yet, the precise molecular trigger as well as the exact role of neuroinflammation in SPG2/PMD disorders are not well understood. Immune cells may be modulated by axonal pathology as well as by oligodendroglial molecules (Zeis et al., 2016). Axonal damage and microglial activation may occur in association with but also independent from increased numbers of T cells (Ransohoff and Brown, 2012; Waisman et al., 2015). Gliosis may also occur independent of evident axonal pathology and *vice versa* low-grade gliosis is not necessarily detrimental to axons or myelin, as seen in mice lacking the myelin protein tetraspanin-2 (de Monasterio-Schrader et al., 2013). In order to better understand a potential contribution of neuroinflammation to the axonopathy in SPG2, we observed the emergence of pathology over time upon deletion of *Plp* in adult mice by tamoxifen injection.

7.5.1. Microgliosis and astrogliosis accompany the initial formation of axonal spheroids

When we deleted *Plp* at the age of 8 weeks by tamoxifen injection and analyzed the emergence of pathology over time, we found significantly more axonal spheroids, microgliosis and astrogliosis by 6-8 months pti. The number of T cells was not increased at this time point, but increased two months later, i.e. by 10 months pti. This suggests that astrocytes and microglia, but not T cells may be involved in the initial formation of axonal spheroids. We cannot distinguish whether the increase of microglia and astroglia is a consequence of axonal pathology or whether they take an active part in this process. Microglia may damage axons, by releasing glutamate, TNF-alpha, nitrogen species or reactive oxygen species, which are highly neurotoxic (Gonzalez and Pacheco, 2014), yet they may also have neuroprotective effects for example against excitotoxicity (Mitrasinovic et al., 2005). Microglia may activate astrocytes (Liddelow and Barres, 2017) and there is astrocyte-dependent recruitment or activation of microglia in the diseased brain (Jo et al., 2017; Skripuletz et al., 2013), so the role of microglia and astrocytes for formation of axonal spheroids remains so far elusive in our model.

7.5.2. T cells do not explain neuropathology to its full extent

The observation that a significant number of axonal spheroids, as well as astrogliosis and microgliosis were apparent before the numbers of T cells increased, suggests that T cells are initially not responsible for axonal damage but develop as a secondary pathology. Also in $Plp^{null/Y}*PLP^{L30R}$ and $Plp^{null/Y}*PLP^{R137W}$ transgenic mice crossed to $Rag1^{null/null}$ mice for depletion of T and B cells, axonal spheroids were ameliorated, but still observed at a significantly higher level than in wildtype mice (Groh et al., 2016), which also indicated that T cells do not explain axonal pathology to its full extent. Likewise, in $Plp^{transgenic-overexpressor}$ mice crossed to $Rag1^{null/null}$ mice for depletion of T and B cells, axonal pathology was strongly reduced, but not completely abolished (Groh et al., 2016; Ip et al., 2006; Ip et al., 2012). Overall this suggests that in our iKO mice as well as in $Plp^{transgenic-overexpressor}$ mice and $Plp^{null/Y}*PLP^{L30R}$ and $Plp^{null/Y}*PLP^{R137W}$ transgenic mice, there is a mechanism leading to axonal spheroids that is independent from the infiltration of T cells. Such a mechanism may, for example, be the lack of metabolic support from dysfunctional oligodendrocytes, as discussed above (chapter 7.2.) yet the exact mechanism is not fully understood.

7.5.3. T cells may amplify neuropathology as a secondary effect

At the time when T cell numbers started to increase in iKO mice (10 months pti) also a strong increase of axonal spheroids was observed, indicating that the infiltration of T cells may amplify axonal pathology. Studies of (Groh et al., 2016; Ip et al., 2006; Ip et al., 2012) imply a very strong implication of T cells for axonal pathology in PMD models. Signs of axonal pathology as well as demyelination were strongly alleviated when the PMD modeling $Plp^{transgenic-overexpressor}$ mice were crossed to $Rag1^{null/null}$ mice to genetically deplete T and B cells (Ip et al., 2006). Depletion of T and B cells also ameliorated axonal transport in the same model (Ip et al., 2012). Likewise, crossing $Plp^{null/Y}*PLP^{L30R}$ and $Plp^{null/Y}*PLP^{R137W}$ transgenic mice to $Rag1^{null/null}$ mice to genetically deplete T and B cells, resulted in reduced numbers of axonal spheroids, as well as ameliorated retrograde axonal transport, reduced demyelination, neuronal loss and brain atrophy (Groh et al., 2016). In contrast, all these features were aggravated when the impact of the adaptive immune system was amplified by crossing $Plp^{null/Y}*PLP^{L30R}$ and $Plp^{null/Y}*PLP^{R137W}$ transgenic mice to $Pd1^{null/null}$ mice, indicating that T cells play an important role for the patholgy in these models (Groh et al., 2016). It needs to be highlighted that the pathology of $Plp^{transgenic-overexpressor}$ mice and the $Plp^{null/Y}*PLP^{L30R}$ and $Plp^{null/Y}*PLP^{R137W}$ transgenic mice is more severe than in PLP-depleted mice in our study and also involves demyelination. Therefore, T cells may influence axonal pathology by different mechanisms and to a different extent in different models. According to our data, T cells may also amplify axonopathy in PLP-deficient mice as a secondary effect.

7.5.4. Which T cell type is involved in the pathology of SPG2

In order to distinguish between different T cell types, we subjected brain cells from iKO mice and Ctrl mice to FACS analysis. We found that the number of CD8+ T cells was significantly increased in the brains of iKO mice 12-17 months pti, whereas there was no significant difference of CD4+ or T_{reg} cells. CD8+ T cells are important components of the immune defense. They can selectively kill infected or damaged cells (Lord et al., 2003) and are also referred to as cytotoxic T cells (Sobottka et al., 2009) or T effector cells (Groh and Martini, 2017). CD4+ T cells infiltrate the CNS in many neurodegenerative disorders and may influence neuronal damage (Gonzalez and Pacheco, 2014). T_{reg} cells are a subtype of CD4+ T cells. They can suppress the function and the proliferation of conventional CD4+ and CD8+ T cells (Mancusi et al., 2018) and thereby may exert a neuroprotective effect. Our observation that only the numbers of CD8+ T cells, but not of CD4+ cells and T_{reg} cells, are significantly increased in iKO mice, also matches observations in a study regarding the role of T cells in $Plp^{transgenic\text{-}overexpressor}$ mice modeling PMD (Ip et al., 2006). T cells were ablated from $Plp^{transgenic\text{-}overexpressor}$ mice by crossing them with $Rag1^{null/null}$ mice. In these $Plp^{transgenic\text{-}overexpressor} * Rag1^{null/null}$ mice the phenotype of $Plp^{transgenic\text{-}overexpressor}$ mice was ameliorated, i.e. there were fewer demyelinated axons and fewer signs of axonal degeneration. Bone marrow transplantation of CD8+ but not CD4+ Tcells reverted the ameliorating effect of T cell ablation. Thus, CD8+ T cells promote neurodegeneration in $Plp^{transgenic\text{-}overexpressor}$ mice, and they can do so in the absence of CD4+ T cells. Similarly, in our PLP-depleted mice, CD8+ T cells may exert a secondary effect by amplifying neuropathology.

7.5.5. How could CD8+ T cells damage axons?

There are different hypotheses how CD8+ T cells may lead to axonal damage. In $Plp^{transgenic\text{-}overexpressor}$ mice immunofluorescence staining showed that CD8+ T cells are directly attached to MHC class I+ oligodendrocytes, suggesting that CD8+ T cells target and damage mutant oligodendrocytes rather than axons (Ip et al., 2006). Axonal degeneration may arise secondary to myelin loss, resulting in loss of its neuroprotective barrier against NO, toxic radicals or proinflammatory radicals (Ip et al., 2012). However, there is no evident demyelination in $Plp^{null/Y}$ mice (Klugmann et al., 1997) and in PLP-deficient mice in this study. Thus, CD8+ T cells would probably need to exert a potentially harmful function for axons via a different mechanism in our PLP-depleted model and $Plp^{null/Y}$ mice.

Alternatively, T cells may lead to axonal damage by activating macrophages or microglia. Ip et al., 2006 observed fewer macrophage-like cells, i.e. macrophages and microglia in $Plp^{transgenic\text{-}overexpressor}$ mice depleted for T and B cells and the remaining macrophage-like cells contained less myelin debris (reflecting reduced phagocytic potential). This observation supports the concept, that T cells may

mediate axonal damage by activating macrophage-like cells (Brookes et al., 2003), and these may mediate degeneration of axons in myelinated tracts (Hendriks et al., 2005). Microglia may for example damage axons by releasing glutamate, TNF-alpha, nitrogen species or reactive oxygen species, which are highly neurotoxic (Gonzalez and Pacheco, 2014). Activated microglia are already observed before the infiltration of T cells in our model. Thus, infiltrated T cells may further activate microglia or influence their profile to become pro-inflammatory (M1 state). Together, T cells may mediate an effect for axonal pathology via activation of microglia.

CD8+ T cells may also damage axons by performing a cytotoxic attack mediated by perforin and granzyme B. Perforin may form a pore in the membrane of a target cell, and this pore may allow granzyme B to enter and lead to apoptosis of the cell (Lord et al., 2003). CD8+ T cells have been observed directly attached to MHC class I+ oligodendrocytes in $Plp^{transgenic-overexpressor}$ mice (Ip et al., 2006), suggesting that they can target dysfunctional oligodendrocytes. T cells have been associated with juxtaparanodes in $Plp^{transgenic-overexpressor}$ mice (Ip et al., 2012), in which axonal spheroids mostly occur, probably due to impaired axonal transport. Since Ip et al., 2012 demonstrated that impaired axonal transport was ameliorated in $Plp^{transgenic-overexpressor}$ mice when T cells were ablated and also when perforin and granzyme B were deleted from T cells, they suggested two ways, how T cells may influence axonal transport at the paranode: (1) The cytotoxic attack may be directed against oligodendrocytes and alter their subcelluar organisation in such a way that for example transport processes are impaired and they cannot properly support axons anymore. (2) Alternatively, perforin and granzyme B, initially targeting glial cells, may "spill over" to axons. Axonal degeneration may thus be a "collateral bystander damage" of CD8+ T cells targeting oligodendrocytes. Granzyme B may damage axons via interaction with the neuronally expressed mannose-6-phosphate-receptor, which is also located on axons (Hawkes and Kar, 2003) and enter the axoplasm by a perforin-dependent process (Lord et al., 2003). Once in the cytoplasm granzyme B could potentially promote reorganization of microtubules (Adrain et al., 2006) or mitochondrial damage (Sobottka et al., 2009), thereby causing impaired axonal transport.

Since axonal spheroids mainly occur at paranodes/juxtaparanodes of $Plp^{null/Y}$ mice (Edgar et al., 2004b; Griffiths et al., 1998), these are some plausible mechanisms how T cells may lead to the formation of axonal spheroids in $Plp^{null/Y}$ mice and our conditional PLP-deficient mice as well. Yet, our study highlights that the effect of T cells is, if at all, a secondary amplification of axonal pathology in PLP-depleted mice, which at low grade also occurs independent from T cells in other models (Groh et al., 2016; Ip et al., 2006; Ip et al., 2012).

7.6. Implications for therapeutic approaches

At the moment there is no way to stop, slow or reverse the progression of PMD, SPG2 and other HSP. Current treatments are limited to alleviating symptoms to some extend, for example with muscle relaxants such as Baclofen, physiotherapy or walking aids (Fink 2013). When regarding options to treat SPG2/PMD by altering the cellular pathomechanisms, it needs to be considered that these are essentially different in SPG2 and different forms of PMD and that no single therapy concept may work for all patients with SPG2 or PMD. While in SPG2 clinical consequences are caused by a loss of function of the *Plp* gene and respective PLP protein, forms of PMD are caused by either duplications or missense mutations of the *Plp* gene, leading to toxic gain of function effects. Some approaches to counteract the toxic effects of accumulated or misfolded PLP have been to downregulate the toxic *Plp* overexpression on mRNA level with the progesterone antagonist Lonaprisan (Prukop et al., 2014), feeding $Plp^{transgenic-overexpressor}$ mice with a cholesterol-enriched diet, to facilitate incorporation of PLP into myelin membranes (Saher et al., 2012) and treatment with Curcumin (Epplen et al., 2015; Yu et al., 2012). Yet, none of these studies have progressed into clinical trials. Since PMD can result from a number of different PLP mutations, with possibly different disease mechanisms, replacing diseased PMD oligodendrocytes with wildtype or genetically-corrected cells may be an attractive, yet very debatable treatment approach (Osorio et al., 2017). Furthermore, it has been suggested that the role of neuroinflammation for PMD may have been underestimated (Marteyn and Baron-Van Evercooren, 2016) and that existing and well-established immunomodulatory therapies, initially developed for multiple sclerosis and other primarily inflammatory diseases (Bittner and Wiendl, 2016), may emerge as treatment options for genetically caused neurodegenerative disorders involving neuroinflammation, such as PMD (Groh and Martini, 2017).

Our study demonstrates that T cells emerge as a secondary pathology upon *Plp*-deletion, yet we do not know wheather they may, as a secondary effect, amplify axonopathy in PLP-deficient mice, as demonstrated in models for PMD (Groh et al., 2016; Ip et al., 2006; Ip et al., 2012). In order to determine, whether immunomodulation may be a considerable treatment approach for SPG2, as considered for PMD (Groh et al., 2016; Groh and Martini, 2017), it may be investigated whether T cell ablation, for example by crossing $Plp^{null/Y}$ mice with $Rag1^{null/null}$ mice, has an alleviating effect for axonopathy. In order to better understand the role of microglia, which are activated prior to infiltration to T cells in our model, it may be determined whether they express rather markers indicating a pro-inflammatory M1 or pro-regenerative M2 phenotype. Components influencing microglial activation status are being exploited (Subramaniam and Federoff, 2017), thus influencing microglial activation status may potentially be a therapeutic approach to alleviate the progression of SPG2 and PMD.

7.7. Turnover and lateral mobility of PLP

Myelin has been regarded as a static structure in the past. Yet, it is increasingly recognized that there is plasticity within myelin. Motor skill learning (Sampaio-Baptista et al., 2013) or social isolation of mice (Liu et al., 2012) leads to changes in myelin. Also in humans, there is turnover of myelin (Yeung et al., 2014) and practicing a skill, such as juggling, can lead to increase of white matter volume (Scholz et al., 2009). Besides investigating in which order pathological events emerge in our tamoxifen-inducible *Plp* knockout mice, we also made observations regarding the turnover of PLP and DM20 within CNS myelin.

7.7.1 Turnover rate of PLP and differentiation of OPCs

When we recombined the *Plp* gene at the age of 8 weeks by tamoxifen injection, we observed the decline of PLP and DM20 within biochemically purified myelin by immunblotting. Myelin is considered to be very stable, yet a slow turnover of myelin proteins has previously been observed. By ^{15}N isotope feeding to rats (Toyama et al., 2013) determined that starting from 6 weeks of age 18.53% of PLP are not exchanged after a period of 6 months. In our analysis 51% PLP was left in myelin 6 months after tamoxifen-induced *Plp*-deletion. It needs to be considered that the analysis by (Toyama et al., 2013) was performed in a different species, i.e. in the rat, that a different method was applied, and that the analysis in (Toyama et al., 2013) has not been done in purified myelin as in our study. Older studies report a half-life of PLP in rats of about 35 days by radioactive labeling of lipids (Smith, 1968) and 95 days in the mouse by protein based [^{3}H]leucine radioactive labeling (Fischer and Morell, 1974). Due to the application of different models and different techniques the results cannot be directly compared, but all reflect a slow turnover of myelin proteins.

We note that the decline of PLP in our model does not allow to draw conclusions about the turnover of myelin in general, as it may be different for different proteins and lipids within myelin. It also needs to be considered that in PLP-deficient mice myelin is not entirely normal, and thus the decline of PLP may have an influence on myelin turnover per se. Interestingly the decline of PLP and DM20 in myelin of iKO mice followed an exponential curve, and at 16 months pti there were still 43% PLP and 30% DM20 left. It is unclear when and if PLP and DM20 at a later time point would be fully depleted. This may be explained by incomplete recombination of oligodendrocytes and OPCs. For tamoxifen-induced Cre expression we used *Plp*^{CreERT2} mice. (Leone et al., 2003) report a recombination efficiency of the *Plp*^{CreERT2} promoter of 90.9 +/- 2.4% of cells in the corpus callosum and 83.5 +/- 5.7% of cells in the white matter of the cerebellum, thus some oligodendroctes may remain unrecombined. For NG2 positive OPCs they report a recombination efficiency of 74.9 +/- 7.7% (Leone et al., 2003). The frequency of recombination may vary depending on the location of loxP sites (Vooijs et al., 2001). Thus recombination efficiency in our

model may differ to the reporter mouse R26R used in (Leone et al., 2003), yet it is likely that a small number of OPCs and maybe some oligodendrocytes remain unrecombined also in our model and contribute to the level of PLP measured by immunoblotting. This may be explain why the abundance of PLP on immunoblots does not appear to reach zero and also why after a period of 6 months, the PLP level appears higher in our analysis compared to the level in (Toyama et al., 2013). A speculative explanation for the reduced decline over time may also be that feedback mechanisms may lead to a reduced turnover when a protein is not synthesized anymore. Furthermore, the turnover of PLP may be faster in some regions or myelin sheaths than in others, which will be further elaborated in chapter 7.8. All in all, with our applied method we did not dissect how much PLP at a given time point comes from PLP-depleted oligodendrocytes and how much comes from newly differentiated oligodendrocytes. Thus, our curves do not reflect the exact turnover rate of PLP and DM20, but they reflect that over all PLP and DM20 levels are diminished slowly in our model over time. Immunoblotting and cryo-immuno electron microscopy reveal a similar reduction of PLP in the brain and optic nerve, respectively.

7.7.2. Lateral mobility of PLP

As one aspect of PLP turnover, we investigated whether it is possible to determine if PLP is diminished towards the abaxonal or adaxonal side of the myelin sheath by immunogold labeling on cryosections from optic nerves. Experiments from (Snaidero et al., 2014) propose that newly synthesized proteins during active developmental myelin biogenesis are delivered to the inner tongue and defined it as the growth zone, suggesting that PLP decline may first be visible at the inside of the myelin sheath in our model. Surprisingly, however we observed that PLP was reduced evenly across the entire cross section of a myelin internode. We therefore cannot distinguish whether PLP is recycled and renewed on the adaxonal or abaxonal side of the compact myelin sheath. Thus, our study indicates that PLP has a high lateral mobility within the myelin sheath. This could be either due to passive diffusion or active transport of PLP to cover the myelin area with an even abundance. Alternatively, PLP turnover may also be mediated via the paranodal loops.

7.8. Reduced abundance of PLP in myelin causes axonopathy

As determined by neuropathological analysis, iKO mice displayed significantly increased numbers of axonal spheroids by 6-8 months pti. At this time PLP was reduced to about 50% as investigated by immunoblotting experiments. This is remarkable as it suggests that not only lack, but also a diminished abundance of PLP leads to axonal pathology, i.e. axonal spheroids as observed in $Plp^{null/Y}$ mice (Griffiths et al., 1998) accompanied by gliosis. Mouse models overexpressing Plp with different levels, show various degrees of clinical and histopathological severity (Anderson et

al., 1998; Inoue et al., 1996; Readhead et al., 1994). Also *in vitro* experiments have exploited a gradual dose-dependent effect of *Plp* overexpression on the survival of co-cultered neurons (Boucher et al., 2002). While it is also established that loss of PLP leads to axonal degeneration (Griffiths et al., 1998), the finding that a diminished amount of PLP triggers the onset of neuropathological features is a new aspect. Pathology-triggering mechanisms may even have started earlier than increased numbers of axonal spheroids and gliosis were detectable in iKO mice, since they may have taken some time to develop. Thus, even a higer level than 50% PLP in myelin may already lead to axonpathy.

However, it needs to be considered that PLP in a few unrecombined oligodendrocytes and differentiated OPCs may contribute to the amount of PLP measured by immunoblotting experiments (chapter 7.7.1.). Furthermore, the speed of turnover and thus the diminishment of PLP may differ in different regions of the brain and maybe even between individual internodes. The differentiation rate of OPCs (Young et al., 2013) as well as the lifetime of oligodendrocytes (Tripathi et al., 2017; Yeung et al., 2014) differ between brain areas; and so might the turnover of proteins. With our immunoblotting analysis we only determined the average abundance of PLP in myelin across the brain. Hypothetically, the level of PLP may diminish faster in the fimbria, where we measured axonal spheroids, than in other brain regions. It may also decline more rapidly in individual internodes. Thus, axons which are ensheathed by myelin harboring very little or no PLP protein, may degenerate in our model. Further studies are needed to investigate a potential region- or internode-dependent turnover of PLP in CNS myelin.

Together, our study implies that not only overexpression (Anderson et al., 1998; Readhead et al., 1994) or lack (Griffiths et al., 1998; Klugmann et al., 1997) but also reduction of PLP leads to impaired axonal maintenance. Thus, it suggests that the full amount of PLP is needed for proper axonal maintenance. This finding has important implications for therapeutic approaches for PMD that aim at a downregulation of overexpressed *Plp*, for example on mRNA level (Prukop et al., 2014). Indeed, it would also be deleterious to downregulate *Plp* expression too much. Gene therapy/cell replacement strategy is also discussed as a potential treatment option for PMD (Osorio et al., 2017; Woodward, 2008) and it has been recognized that one of the manifold challenges would be to gain *Plp* expression at the right level (Woodward, 2008). Our study supports this notion and adds that axonal maintenance is not only sensitive to increased (Anderson et al., 1998; Readhead et al., 1994) but also to decreased *Plp* expression.

8. Summary

Proper functioning of the central nervous system (CNS) depends on the interplay of neurons with oligodendrocytes, the myelinating cells of the CNS. However, the interactions between oligodendrocytes and their myelinated axons are not well understood. For example, deletion of the most abundant protein of CNS myelin, proteolipid protein (PLP), causes spastic paraplegia type 2 (SPG2), which is characterized by axonal degeneration. In both patients and the corresponding mouse model ($Plp^{null/Y}$ mice), axons degenerate despite only minor structural myelin abnormalities. Since Plp has been considered to be exclusively expressed in the oligodendrocyte lineage, it has been assumed that the primary cause of SPG2 is the lack of PLP from oligodendrocytes. However, several recent studies have detected Plp gene products also in a subset of neurons. Consequently, it has been suggested that the loss of Plp expression in neurons could cause axonal pathology. To clarify the primary cellular origin of SPG2, we established mice with a floxed Plp allele to selectively delete Plp in neurons or oligodendrocytes by recombination with cell-type specific Cre driver lines. Recombination of Plp in excitatory projection neurons did not cause neuropathology, whereas oligodendroglial deletion of Plp caused the complete neurodegenerative spectrum observed in $Plp^{null/Y}$ mice including axonopathy, gliosis and T cell infiltration into the brain. We conclude that the primary cause of SPG2 is the lack of PLP in oligodendrocytes. To better understand the interplay of PLP-deficient oligodendrocytes, axons and T cells, we analyzed the emergence of neuropathological events upon Plp-deletion over time. We therefore interbred mice with a floxed Plp allele with mice harboring a tamoxifen-inducible Cre in oligodendrocytes and induced Plp-deletion by tamoxifen injection in adult mice. We observed a slow decline of PLP in myelin over months, supporting the concept that myelin turnover is very slow. Interestingly, PLP was diminished evenly across the myelin layers, indicating a high lateral mobility of PLP. The entire neurodegenerative spectrum observed in $Plp^{null/Y}$ mice developed over time, including axonopathy, gliosis and T cell infiltration. As axonopathy was already detectable when the abundance of PLP in myelin was reduced to about 50%, we conclude that the normally very high abundance of PLP is required for axonal support. Importantly, axonal spheroids and gliosis were observed prior to elevated numbers of T cells, implying that axonopathy occurs independent from T cells in this model, at least initially. Thus, T cells emerge as secondary pathology and may exert an amplifying effect on neuropathology.

9. References

Adrain, C., Duriez, P.J., Brumatti, G., Delivani, P., and Martin, S.J. (2006). The cytotoxic lymphocyte protease, granzyme B, targets the cytoskeleton and perturbs microtubule polymerization dynamics. The Journal of biological chemistry *281*, 8118-8125.

Aggarwal, S., Snaidero, N., Pahler, G., Frey, S., Sanchez, P., Zweckstetter, M., Janshoff, A., Schneider, A., Weil, M.T., Schaap, I.A.*, et al.* (2013). Myelin membrane assembly is driven by a phase transition of myelin basic proteins into a cohesive protein meshwork. PLoS Biol *11*, e1001577.

Anderson, M.A., Burda, J.E., Ren, Y., Ao, Y., O'Shea, T.M., Kawaguchi, R., Coppola, G., Khakh, B.S., Deming, T.J., and Sofroniew, M.V. (2016). Astrocyte scar formation aids central nervous system axon regeneration. Nature *532*, 195-200.

Anderson, T.J., Schneider, A., Barrie, J.A., Klugmann, M., McCulloch, M.C., Kirkham, D., Kyriakides, E., Nave, K.A., and Griffiths, I.R. (1998). Late-onset neurodegeneration in mice with increased dosage of the proteolipid protein gene. The Journal of comparative neurology *394*, 506-519.

Appel, S.H., Zhao, W., Beers, D.R., and Henkel, J.S. (2011). The microglial-motoneuron dialogue in ALS. Acta myologica : myopathies and cardiomyopathies : official journal of the Mediterranean Society of Myology *30*, 4-8.

Arroyo, E.J., and Scherer, S.S. (2000). On the molecular architecture of myelinated fibers. Histochemistry and cell biology *113*, 1-18.

Bakhti, M., Snaidero, N., Schneider, D., Aggarwal, S., Mobius, W., Janshoff, A., Eckhardt, M., Nave, K.A., and Simons, M. (2013). Loss of electrostatic cell-surface repulsion mediates myelin membrane adhesion and compaction in the central nervous system. Proc Natl Acad Sci U S A *110*, 3143-3148.

Bao, X., Wang, Y., Li, X., Li, X.M., Liu, Z., Yang, T., Wong, C.F., Zhang, J., Hao, Q., and Li, X.D. (2014). Identification of 'erasers' for lysine crotonylated histone marks using a chemical proteomics approach. eLife *3*.

Barkovich, A.J. (2000). Concepts of myelin and myelination in neuroradiology. AJNR American journal of neuroradiology *21*, 1099-1109.

Belvindrah, R., Graus-Porta, D., Goebbels, S., Nave, K.A., and Muller, U. (2007). Beta1 integrins in radial glia but not in migrating neurons are essential for the formation of cell layers in the cerebral cortex. J Neurosci *27*, 13854-13865.

Bittner, S., and Wiendl, H. (2016). Neuroimmunotherapies Targeting T Cells: From Pathophysiology to Therapeutic Applications. Neurotherapeutics : the journal of the American Society for Experimental NeuroTherapeutics *13*, 4-19.

Bizzozero, O.A., Bixler, H.A., Davis, J.D., Espinosa, A., and Messier, A.M. (2001). Chemical deacylation reduces the adhesive properties of proteolipid protein and leads to decompaction of the myelin sheath. J Neurochem *76*, 1129-1141.

Bizzozero, O.A., and Howard, T.A. (2002). Myelin proteolipid protein-induced aggregation of lipid vesicles: efficacy of the various molecular species. Neurochem Res *27*, 1269-1277.

Blackstone, C., O'Kane, C.J., and Reid, E. (2011). Hereditary spastic paraplegias: membrane traffic and the motor pathway. Nat Rev Neurosci *12*, 31-42.

Boggs, J.M. (2006). Myelin basic protein: a multifunctional protein. Cell Mol Life Sci *63*, 1945-1961.

References

Bongarzone, E.R., Campagnoni, C.W., Kampf, K., Jacobs, E.C., Handley, V.W., Schonmann, V., and Campagnoni, A.T. (1999). Identification of a new exon in the myelin proteolipid protein gene encoding novel protein isoforms that are restricted to the somata of oligodendrocytes and neurons. J Neurosci *19*, 8349-8357.

Bormuth, I., Yan, K., Yonemasu, T., Gummert, M., Zhang, M., Wichert, S., Grishina, O., Pieper, A., Zhang, W., Goebbels, S.*, et al.* (2013). Neuronal basic helix-loop-helix proteins Neurod2/6 regulate cortical commissure formation before midline interactions. J Neurosci *33*, 641-651.

Boucher, S.E., Cypher, M.A., Carlock, L.R., and Skoff, R.P. (2002). Proteolipid protein gene modulates viability and phenotype of neurons. J Neurosci *22*, 1772-1783.

Brady, S.T., and Lasek, R.J. (1981). Nerve-specific enolase and creatine phosphokinase in axonal transport: soluble proteins and the axoplasmic matrix. Cell *23*, 515-523.

Brender, T., Wallerstein, D., Sum, J., and Wallerstein, R. (2015). Unusual presentation of pelizaeus-merzbacher disease: female patient with deletion of the proteolipid protein 1 gene. Case reports in genetics *2015*, 453105.

Brinkmann, B.G., Agarwal, A., Sereda, M.W., Garratt, A.N., Muller, T., Wende, H., Stassart, R.M., Nawaz, S., Humml, C., Velanac, V.*, et al.* (2008). Neuregulin-1/ErbB signaling serves distinct functions in myelination of the peripheral and central nervous system. Neuron *59*, 581-595.

Brookes, R.H., Pathan, A.A., McShane, H., Hensmann, M., Price, D.A., and Hill, A.V. (2003). CD8+ T cell-mediated suppression of intracellular Mycobacterium tuberculosis growth in activated human macrophages. European journal of immunology *33*, 3293-3302.

Chiu, I.M., Morimoto, E.T., Goodarzi, H., Liao, J.T., O'Keeffe, S., Phatnani, H.P., Muratet, M., Carroll, M.C., Levy, S., Tavazoie, S.*, et al.* (2013). A neurodegeneration-specific gene-expression signature of acutely isolated microglia from an amyotrophic lateral sclerosis mouse model. Cell reports *4*, 385-401.

Colonna, M., and Butovsky, O. (2017). Microglia Function in the Central Nervous System During Health and Neurodegeneration. Annual review of immunology *35*, 441-468.

Crosby, A.H., and Proukakis, C. (2002). Is the transportation highway the right road for hereditary spastic paraplegia? Am J Hum Genet *71*, 1009-1016.

de Monasterio-Schrader, P., Jahn, O., Tenzer, S., Wichert, S.P., Patzig, J., and Werner, H.B. (2012). Systematic approaches to central nervous system myelin. Cell Mol Life Sci *69*, 2879-2894.

de Monasterio-Schrader, P., Patzig, J., Mobius, W., Barrette, B., Wagner, T.L., Kusch, K., Edgar, J.M., Brophy, P.J., and Werner, H.B. (2013). Uncoupling of neuroinflammation from axonal degeneration in mice lacking the myelin protein tetraspanin-2. Glia *61*, 1832-1847.

Delaunay, D., Heydon, K., Cumano, A., Schwab, M.H., Thomas, J.L., Suter, U., Nave, K.A., Zalc, B., and Spassky, N. (2008). Early neuronal and glial fate restriction of embryonic neural stem cells. J Neurosci *28*, 2551-2562.

Dick, K.J., Al-Mjeni, R., Baskir, W., Koul, R., Simpson, M.A., Patton, M.A., Raeburn, S., and Crosby, A.H. (2008). A novel locus for an autosomal recessive hereditary spastic paraplegia (SPG35) maps to 16q21-q23. Neurology *71*, 248-252.

Doyle, J.P., Dougherty, J.D., Heiman, M., Schmidt, E.F., Stevens, T.R., Ma, G., Bupp, S., Shrestha, P., Shah, R.D., Doughty, M.L.*, et al.* (2008). Application of a translational profiling approach for the comparative analysis of CNS cell types. Cell *135*, 749-762.

Duncan, I.D. (2005). The PLP mutants from mouse to man. J Neurol Sci *228*, 204-205.

Duncan, I.D., Hammang, J.P., and Trapp, B.D. (1987). Abnormal compact myelin in the myelin-deficient rat: absence of proteolipid protein correlates with a defect in the intraperiod line. Proc Natl Acad Sci U S A *84*, 6287-6291.

Edgar, J.M., McLaughlin, M., Barrie, J.A., McCulloch, M.C., Garbern, J., and Griffiths, I.R. (2004a). Age-related axonal and myelin changes in the rumpshaker mutation of the Plp gene. Acta neuropathologica *107*, 331-335.

Edgar, J.M., McLaughlin, M., Werner, H.B., McCulloch, M.C., Barrie, J.A., Brown, A., Faichney, A.B., Snaidero, N., Nave, K.A., and Griffiths, I.R. (2009). Early ultrastructural defects of axons and axon-glia junctions in mice lacking expression of Cnp1. Glia *57*, 1815-1824.

Edgar, J.M., McLaughlin, M., Yool, D., Zhang, S.C., Fowler, J.H., Montague, P., Barrie, J.A., McCulloch, M.C., Duncan, I.D., Garbern, J.*, et al.* (2004b). Oligodendroglial modulation of fast axonal transport in a mouse model of hereditary spastic paraplegia. The Journal of cell biology *166*, 121-131.

Epplen, D.B., Prukop, T., Nientiedt, T., Albrecht, P., Arlt, F.A., Stassart, R.M., Kassmann, C.M., Methner, A., Nave, K.A., Werner, H.B.*, et al.* (2015). Curcumin therapy in a Plp1 transgenic mouse model of Pelizaeus-Merzbacher disease. Annals of clinical and translational neurology *2*, 787-796.

Farley, F.W., Soriano, P., Steffen, L.S., and Dymecki, S.M. (2000). Widespread recombinase expression using FLPeR (flipper) mice. Genesis *28*, 106-110.

Fernandez-Miranda, J.C., Rhoton, A.L., Jr., Alvarez-Linera, J., Kakizawa, Y., Choi, C., and de Oliveira, E.P. (2008). Three-dimensional microsurgical and tractographic anatomy of the white matter of the human brain. Neurosurgery *62*, 989-1026; discussion 1026-1028.

Fink, J.K. (2013). Hereditary spastic paraplegia: clinico-pathologic features and emerging molecular mechanisms. Acta neuropathologica *126*, 307-328.

Fischer, C.A., and Morell, P. (1974). Turnover of proteins in myelin and myelin-like material of mouse brain. Brain research *74*, 51-65.

Fjermestad, K.W., Kanavin, O.J., Naess, E.E., Hoxmark, L.B., and Hummelvoll, G. (2016). Health survey of adults with hereditary spastic paraparesis compared to population study controls. Orphanet journal of rare diseases *11*, 98.

Frühbeis, C., Fröhlich, D., Kuo, W.P., Amphornrat, J., Thilemann, S., Saab, A.S., Kirchhoff, F., Möbius, W., Goebbels, S., Nave, K.A.*, et al.* (2013). Neurotransmitter-triggered transfer of exosomes mediates oligodendrocyte-neuron communication. PLoS Biol *11*, e1001604.

Fulton, D., Paez, P., Spreur, V., Handley, V., Colwell, C.S., Campagnoni, A., and Fisher, R. (2011). Developmental activation of the proteolipid protein promoter transgene in neuronal and oligodendroglial cells of neostriatum in mice. Developmental neuroscience *33*, 170-184.

Funfschilling, U., Supplie, L.M., Mahad, D., Boretius, S., Saab, A.S., Edgar, J., Brinkmann, B.G., Kassmann, C.M., Tzvetanova, I.D., Mobius, W.*, et al.* (2012). Glycolytic oligodendrocytes maintain myelin and long-term axonal integrity. Nature *485*, 517-521.

Garbern, J.Y. (2007). Pelizaeus-Merzbacher disease: Genetic and cellular pathogenesis. Cell Mol Life Sci *64*, 50-65.

Garbern, J.Y., Yool, D.A., Moore, G.J., Wilds, I.B., Faulk, M.W., Klugmann, M., Nave, K.A., Sistermans, E.A., van der Knaap, M.S., Bird, T.D.*, et al.* (2002). Patients lacking the major CNS myelin protein, proteolipid protein 1, develop length-dependent axonal degeneration in the absence of demyelination and inflammation. Brain *125*, 551-561.

References

Garcia-Lopez, P., Garcia-Marin, V., and Freire, M. (2010). Dendritic spines and development: towards a unifying model of spinogenesis--a present day review of Cajal's histological slides and drawings. Neural plasticity *2010*, 769207.

Garcia-Marin, V., Garcia-Lopez, P., and Freire, M. (2007). Cajal's contributions to glia research. Trends in neurosciences *30*, 479-487.

Gibbs, K.L., Greensmith, L., and Schiavo, G. (2015). Regulation of Axonal Transport by Protein Kinases. Trends in biochemical sciences *40*, 597-610.

Goebbels, S., Bormuth, I., Bode, U., Hermanson, O., Schwab, M.H., and Nave, K.A. (2006). Genetic targeting of principal neurons in neocortex and hippocampus of NEX-Cre mice. Genesis *44*, 611-621.

Gong, S., Zheng, C., Doughty, M.L., Losos, K., Didkovsky, N., Schambra, U.B., Nowak, N.J., Joyner, A., Leblanc, G., Hatten, M.E.*, et al.* (2003). A gene expression atlas of the central nervous system based on bacterial artificial chromosomes. Nature *425*, 917-925.

Gonzalez, H., and Pacheco, R. (2014). T-cell-mediated regulation of neuroinflammation involved in neurodegenerative diseases. Journal of neuroinflammation *11*, 201.

Gow, A., Southwood, C.M., Li, J.S., Pariali, M., Riordan, G.P., Brodie, S.E., Danias, J., Bronstein, J.M., Kachar, B., and Lazzarini, R.A. (1999). CNS myelin and sertoli cell tight junction strands are absent in Osp/claudin-11 null mice. Cell *99*, 649-659.

Greenfield, E.A., Reddy, J., Lees, A., Dyer, C.A., Koul, O., Nguyen, K., Bell, S., Kassam, N., Hinojoza, J., Eaton, M.J.*, et al.* (2006). Monoclonal antibodies to distinct regions of human myelin proteolipid protein simultaneously recognize central nervous system myelin and neurons of many vertebrate species. J Neurosci Res *83*, 415-431.

Griffiths, I., Klugmann, M., Anderson, T., Yool, D., Thomson, C., Schwab, M.H., Schneider, A., Zimmermann, F., McCulloch, M., Nadon, N.*, et al.* (1998). Axonal swellings and degeneration in mice lacking the major proteolipid of myelin. Science *280*, 1610-1613.

Groh, J., Friedman, H.C., Orel, N., Ip, C.W., Fischer, S., Spahn, I., Schaffner, E., Horner, M., Stadler, D., Buttmann, M.*, et al.* (2016). Pathogenic inflammation in the CNS of mice carrying human PLP1 mutations. Hum Mol Genet.

Groh, J., and Martini, R. (2017). Neuroinflammation as modifier of genetically caused neurological disorders of the central nervous system: Understanding pathogenesis and chances for treatment. Glia *65*, 1407-1422.

Gruenenfelder, F.I., Thomson, G., Penderis, J., and Edgar, J.M. (2011). Axon-glial interaction in the CNS: what we have learned from mouse models of Pelizaeus-Merzbacher disease. J Anat *219*, 33-43.

Hagemeyer, N., Goebbels, S., Papiol, S., Kastner, A., Hofer, S., Begemann, M., Gerwig, U.C., Boretius, S., Wieser, G.L., Ronnenberg, A.*, et al.* (2012). A myelin gene causative of a catatonia-depression syndrome upon aging. EMBO Mol Med *4*, 528-539.

Harlow, D.E., Saul, K.E., Culp, C.M., Vesely, E.M., and Macklin, W.B. (2014). Expression of proteolipid protein gene in spinal cord stem cells and early oligodendrocyte progenitor cells is dispensable for normal cell migration and myelination. J Neurosci *34*, 1333-1343.

Harlow, D.E., Saul, K.E., Komuro, H., and Macklin, W.B. (2015). Myelin Proteolipid Protein Complexes with alphav Integrin and AMPA Receptors In Vivo and Regulates AMPA-Dependent Oligodendrocyte Progenitor Cell Migration through the Modulation of Cell-Surface GluR2 Expression. J Neurosci *35*, 12018-12032.

Hawkes, C., and Kar, S. (2003). Insulin-like growth factor-II/mannose-6-phosphate receptor: widespread distribution in neurons of the central nervous system including those expressing cholinergic phenotype. The Journal of comparative neurology *458*, 113-127.

Hendriks, J., Teunissen, C., Vries, H., and D Dijkstra, C. (2005). Macrophages and neurodegeneration. Brain Res Brain Res Rev, Vol 48.

Hodgkin, A.L., and Huxley, A.F. (1952). A quantitative description of membrane current and its application to conduction and excitation in nerve. The Journal of physiology *117*, 500-544.

Ikenaka, K., Kagawa, T., and Mikoshiba, K. (1992). Selective expression of DM-20, an alternatively spliced myelin proteolipid protein gene product, in developing nervous system and in nonglial cells. J Neurochem *58*, 2248-2253.

Inoue, K. (2005). PLP1-related inherited dysmyelinating disorders: Pelizaeus-Merzbacher disease and spastic paraplegia type 2. Neurogenetics *6*, 1-16.

Inoue, K. (2017). Cellular Pathology of Pelizaeus-Merzbacher Disease Involving Chaperones Associated with Endoplasmic Reticulum Stress. Frontiers in molecular biosciences *4*, 7.

Inoue, Y., Kagawa, T., Matsumura, Y., Ikenaka, K., and Mikoshiba, K. (1996). Cell death of oligodendrocytes or demyelination induced by overexpression of proteolipid protein depending on expressed gene dosage. Neuroscience research *25*, 161-172.

Ip, C.W., Kroner, A., Bendszus, M., Leder, C., Kobsar, I., Fischer, S., Wiendl, H., Nave, K.A., and Martini, R. (2006). Immune cells contribute to myelin degeneration and axonopathic changes in mice overexpressing proteolipid protein in oligodendrocytes. J Neurosci *26*, 8206-8216.

Ip, C.W., Kroner, A., Groh, J., Huber, M., Klein, D., Spahn, I., Diem, R., Williams, S.K., Nave, K.A., Edgar, J.M.*, et al.* (2012). Neuroinflammation by cytotoxic T-lymphocytes impairs retrograde axonal transport in an oligodendrocyte mutant mouse. PLoS One *7*, e42554.

Jacobs, E.C., Bongarzone, E.R., Campagnoni, C.W., and Campagnoni, A.T. (2004). Embryonic expression of the soma-restricted products of the myelin proteolipid gene in motor neurons and muscle. Neurochem Res *29*, 997-1002.

Jacobs, E.C., Bongarzone, E.R., Campagnoni, C.W., Kampf, K., and Campagnoni, A.T. (2003). Soma-restricted products of the myelin proteolipid gene are expressed primarily in neurons in the developing mouse nervous system. Developmental neuroscience *25*, 96-104.

Jahn, O., Tenzer, S., and Werner, H.B. (2009). Myelin proteomics: molecular anatomy of an insulating sheath. Mol Neurobiol *40*, 55-72.

Jo, M., Kim, J.H., Song, G.J., Seo, M., Hwang, E.M., and Suk, K. (2017). Astrocytic Orosomucoid-2 Modulates Microglial Activation and Neuroinflammation. J Neurosci *37*, 2878-2894.

Kang, S.H., Li, Y., Fukaya, M., Lorenzini, I., Cleveland, D.W., Ostrow, L.W., Rothstein, J.D., and Bergles, D.E. (2013). Degeneration and impaired regeneration of gray matter oligodendrocytes in amyotrophic lateral sclerosis. Nat Neurosci *16*, 571-579.

Klugmann, M., Schwab, M.H., Puhlhofer, A., Schneider, A., Zimmermann, F., Griffiths, I.R., and Nave, K.A. (1997). Assembly of CNS myelin in the absence of proteolipid protein. Neuron *18*, 59-70.

Laemmli, U.K. (1970). Cleavage of structural proteins during the assembly of the head of bacteriophage T4. Nature *227*, 680-685.

Lagumersindez-Denis, N., Wrzos, C., Mack, M., Winkler, A., van der Meer, F., Reinert, M.C., Hollasch, H., Flach, A., Bruhl, H., Cullen, E.*, et al.* (2017). Differential contribution of immune

References

effector mechanisms to cortical demyelination in multiple sclerosis. Acta neuropathologica *134*, 15-34.

Lappe-Siefke, C., Goebbels, S., Gravel, M., Nicksch, E., Lee, J., Braun, P.E., Griffiths, I.R., and Nave, K.A. (2003). Disruption of Cnp1 uncouples oligodendroglial functions in axonal support and myelination. Nat Genet *33*, 366-374.

Larocca, J.N., and Norton, W.T. (2007). Isolation of myelin. Current protocols in cell biology *Chapter 3*, Unit3 25.

Lee, Y., Morrison, B.M., Li, Y., Lengacher, S., Farah, M.H., Hoffman, P.N., Liu, Y., Tsingalia, A., Jin, L., Zhang, P.W.*, et al.* (2012). Oligodendroglia metabolically support axons and contribute to neurodegeneration. Nature *487*, 443-448.

Lein, E.S., Hawrylycz, M.J., Ao, N., Ayres, M., Bensinger, A., Bernard, A., Boe, A.F., Boguski, M.S., Brockway, K.S., Byrnes, E.J.*, et al.* (2007). Genome-wide atlas of gene expression in the adult mouse brain. Nature *445*, 168-176.

Leone, D.P., Genoud, S., Atanasoski, S., Grausenburger, R., Berger, P., Metzger, D., Macklin, W.B., Chambon, P., and Suter, U. (2003). Tamoxifen-inducible glia-specific Cre mice for somatic mutagenesis in oligodendrocytes and Schwann cells. Molecular and cellular neurosciences *22*, 430-440.

Li, C., Tropak, M.B., Gerlai, R., Clapoff, S., Abramow-Newerly, W., Trapp, B., Peterson, A., and Roder, J. (1994). Myelination in the absence of myelin-associated glycoprotein. Nature *369*, 747-750.

Li, G., Fang, L., Fernandez, G., and Pleasure, S.J. (2013). The ventral hippocampus is the embryonic origin for adult neural stem cells in the dentate gyrus. Neuron *78*, 658-672.

Li, W., Zhang, B., Tang, J., Cao, Q., Wu, Y., Wu, C., Guo, J., Ling, E.A., and Liang, F. (2007). Sirtuin 2, a mammalian homolog of yeast silent information regulator-2 longevity regulator, is an oligodendroglial protein that decelerates cell differentiation through deacetylating alpha-tubulin. J Neurosci *27*, 2606-2616.

Liddelow, S.A., and Barres, B.A. (2017). Reactive Astrocytes: Production, Function, and Therapeutic Potential. Immunity *46*, 957-967.

Liddelow, S.A., Guttenplan, K.A., Clarke, L.E., Bennett, F.C., Bohlen, C.J., Schirmer, L., Bennett, M.L., Munch, A.E., Chung, W.S., Peterson, T.C.*, et al.* (2017). Neurotoxic reactive astrocytes are induced by activated microglia. Nature *541*, 481-487.

Liou, W., Geuze, H.J., and Slot, J.W. (1996). Improving structural integrity of cryosections for immunogold labeling. Histochemistry and cell biology *106*, 41-58.

Liu, J., Dietz, K., DeLoyht, J.M., Pedre, X., Kelkar, D., Kaur, J., Vialou, V., Lobo, M.K., Dietz, D.M., Nestler, E.J.*, et al.* (2012). Impaired adult myelination in the prefrontal cortex of socially isolated mice. Nat Neurosci *15*, 1621-1623.

Lopez-Munoz, F., Boya, J., and Alamo, C. (2006). Neuron theory, the cornerstone of neuroscience, on the centenary of the Nobel Prize award to Santiago Ramon y Cajal. Brain research bulletin *70*, 391-405.

Lord, S.J., Rajotte, R.V., Korbutt, G.S., and Bleackley, R.C. (2003). Granzyme B: a natural born killer. Immunological reviews *193*, 31-38.

Lowry, O.H., Rosebrough, N.J., Farr, A.L., and Randall, R.J. (1951). Protein measurement with the Folin phenol reagent. The Journal of biological chemistry *193*, 265-275.

Luders, K.A., Patzig, J., Simons, M., Nave, K.A., and Werner, H.B. (2017). Genetic dissection of oligodendroglial and neuronal Plp1 function in a novel mouse model of spastic paraplegia type 2. Glia *65*, 1762-1776.

Macklin, W.B., Campagnoni, C.W., Deininger, P.L., and Gardinier, M.V. (1987). Structure and expression of the mouse myelin proteolipid protein gene. J Neurosci Res *18*, 383-394.

Mancusi, A., Piccinelli, S., Velardi, A., and Pierini, A. (2018). The Effect of TNF-alpha on Regulatory T Cell Function in Graft-versus-Host Disease. Frontiers in immunology *9*, 356.

Marteyn, A., and Baron-Van Evercooren, A. (2016). Is involvement of inflammation underestimated in Pelizaeus-Merzbacher disease? J Neurosci Res *94*, 1572-1578.

Mayer, J.A., Griffiths, I.R., Goldman, J.E., Smith, C.M., Cooksey, E., Radcliff, A.B., and Duncan, I.D. (2015). Modeling the natural history of Pelizaeus-Merzbacher disease. Neurobiol Dis *75*, 115-130.

McGrail, K.M., Phillips, J.M., and Sweadner, K.J. (1991). Immunofluorescent localization of three Na,K-ATPase isozymes in the rat central nervous system: both neurons and glia can express more than one Na,K-ATPase. J Neurosci *11*, 381-391.

McLaughlin, M., Karim, S.A., Montague, P., Barrie, J.A., Kirkham, D., Griffiths, I.R., and Edgar, J.M. (2007). Genetic background influences UPR but not PLP processing in the rumpshaker model of PMD/SPG2. Neurochem Res *32*, 167-176.

Michalski, J.P., Anderson, C., Beauvais, A., De Repentigny, Y., and Kothary, R. (2011). The proteolipid protein promoter drives expression outside of the oligodendrocyte lineage during embryonic and early postnatal development. PLoS One *6*, e19772.

Michan, S., and Sinclair, D. (2007). Sirtuins in mammals: insights into their biological function. The Biochemical journal *404*, 1-13.

Miller, M.J., Haxhiu, M.A., Georgiadis, P., Gudz, T.I., Kangas, C.D., and Macklin, W.B. (2003). Proteolipid protein gene mutation induces altered ventilatory response to hypoxia in the myelin-deficient rat. J Neurosci *23*, 2265-2273.

Miller, M.J., Kangas, C.D., and Macklin, W.B. (2009). Neuronal expression of the proteolipid protein gene in the medulla of the mouse. J Neurosci Res *87*, 2842-2853.

Mitrasinovic, O.M., Grattan, A., Robinson, C.C., Lapustea, N.B., Poon, C., Ryan, H., Phong, C., and Murphy, G.M., Jr. (2005). Microglia overexpressing the macrophage colony-stimulating factor receptor are neuroprotective in a microglial-hippocampal organotypic coculture system. J Neurosci *25*, 4442-4451.

Mobius, W. (2009). Cryopreparation of biological specimens for immunoelectron microscopy. Annals of anatomy = Anatomischer Anzeiger : official organ of the Anatomische Gesellschaft *191*, 231-247.

Mobius, W., Cooper, B., Kaufmann, W.A., Imig, C., Ruhwedel, T., Snaidero, N., Saab, A.S., and Varoqueaux, F. (2010). Electron microscopy of the mouse central nervous system. Methods in cell biology *96*, 475-512.

Mobius, W., Nave, K.A., and Werner, H.B. (2016). Electron microscopy of myelin: Structure preservation by high-pressure freezing. Brain research *1641*, 92-100.

Mobius, W., Patzig, J., Nave, K.A., and Werner, H.B. (2008). Phylogeny of proteolipid proteins: divergence, constraints, and the evolution of novel functions in myelination and neuroprotection. Neuron glia biology *4*, 111-127.

References

Mullis, K., Faloona, F., Scharf, S., Saiki, R., Horn, G., and Erlich, H. (1986). Specific enzymatic amplification of DNA in vitro: the polymerase chain reaction. Cold Spring Harbor symposia on quantitative biology *51 Pt 1*, 263-273.

Navarrete, M., and Araque, A. (2014). The Cajal school and the physiological role of astrocytes: a way of thinking. Frontiers in Neuroanatomy *8*.

Nave, K.A. (2010). Myelination and the trophic support of long axons. Nat Rev Neurosci *11*, 275-283.

Nave, K.A., Lai, C., Bloom, F.E., and Milner, R.J. (1987). Splice site selection in the proteolipid protein (PLP) gene transcript and primary structure of the DM-20 protein of central nervous system myelin. Proc Natl Acad Sci U S A *84*, 5665-5669.

Nave, K.A., and Werner, H.B. (2014). Myelination of the nervous system: mechanisms and functions. Annu Rev Cell Dev Biol *30*, 503-533.

Nawaz, S., Schweitzer, J., Jahn, O., and Werner, H.B. (2013). Molecular evolution of myelin basic protein, an abundant structural myelin component. Glia *61*, 1364-1377.

Nguyen, M.V., Felice, C.A., Du, F., Covey, M.V., Robinson, J.K., Mandel, G., and Ballas, N. (2013). Oligodendrocyte lineage cells contribute unique features to Rett syndrome neuropathology. J Neurosci *33*, 18764-18774.

North, B.J., Marshall, B.L., Borra, M.T., Denu, J.M., and Verdin, E. (2003). The human Sir2 ortholog, SIRT2, is an NAD+-dependent tubulin deacetylase. Molecular cell *11*, 437-444.

Norton, W.T., and Poduslo, S.E. (1973). Myelination in rat brain: changes in myelin composition during brain maturation. J Neurochem *21*, 759-773.

Oblinger, M.M., Foe, L.G., Kwiatkowska, D., and Kemp, R.G. (1988). Phosphofructokinase in the rat nervous system: regional differences in activity and characteristics of axonal transport. J Neurosci Res *21*, 25-34.

Olmos-Serrano, J.L., Kang, H.J., Tyler, W.A., Silbereis, J.C., Cheng, F., Zhu, Y., Pletikos, M., Jankovic-Rapan, L., Cramer, N.P., Galdzicki, Z.*, et al.* (2016). Down Syndrome Developmental Brain Transcriptome Reveals Defective Oligodendrocyte Differentiation and Myelination. Neuron *89*, 1208-1222.

Orthmann-Murphy, J.L., Salsano, E., Abrams, C.K., Bizzi, A., Uziel, G., Freidin, M.M., Lamantea, E., Zeviani, M., Scherer, S.S., and Pareyson, D. (2009). Hereditary spastic paraplegia is a novel phenotype for GJA12/GJC2 mutations. Brain *132*, 426-438.

Osorio, M.J., Rowitch, D.H., Tesar, P., Wernig, M., Windrem, M.S., and Goldman, S.A. (2017). Concise Review: Stem Cell-Based Treatment of Pelizaeus-Merzbacher Disease. Stem cells *35*, 311-315.

Parpura, V., Heneka, M.T., Montana, V., Oliet, S.H., Schousboe, A., Haydon, P.G., Stout, R.F., Jr., Spray, D.C., Reichenbach, A., Pannicke, T.*, et al.* (2012). Glial cells in (patho)physiology. J Neurochem *121*, 4-27.

Patzig, J., Erwig, M.S., Tenzer, S., Kusch, K., Dibaj, P., Mobius, W., Goebbels, S., Schaeren-Wiemers, N., Nave, K.A., and Werner, H.B. (2016a). Septin/anillin filaments scaffold central nervous system myelin to accelerate nerve conduction. eLife *5*.

Patzig, J., Kusch, K., Fledrich, R., Eichel, M.A., Luders, K.A., Mobius, W., Sereda, M.W., Nave, K.A., Martini, R., and Werner, H.B. (2016b). Proteolipid protein modulates preservation of peripheral axons and premature death when myelin protein zero is lacking. Glia *64*, 155-174.

Peterson, G.L. (1979). Review of the Folin phenol protein quantitation method of Lowry, Rosebrough, Farr and Randall. Analytical biochemistry *100*, 201-220.

Petit, B., Giraudet, F., Bechon, C., Bardin, L., Avan, P., Boespflug-Tanguy, O., and Begou, M. (2014). Mice with a deletion of the major central myelin protein exhibit hypersensitivity to noxious thermal stimuli: involvement of central sensitization. Neurobiol Dis *65*, 55-68.

Poliak, S., and Peles, E. (2003). The local differentiation of myelinated axons at nodes of Ranvier. Nat Rev Neurosci *4*, 968-980.

Popot, J.L., Pham Dinh, D., and Dautigny, A. (1991). Major Myelin proteolipid: the 4-alpha-helix topology. The Journal of membrane biology *120*, 233-246.

Prukop, T., Epplen, D.B., Nientiedt, T., Wichert, S.P., Fledrich, R., Stassart, R.M., Rossner, M.J., Edgar, J.M., Werner, H.B., Nave, K.A.*, et al.* (2014). Progesterone antagonist therapy in a pelizaeus-merzbacher mouse model. Am J Hum Genet *94*, 533-546.

Quarles, R.H. (2002). Myelin sheaths: glycoproteins involved in their formation, maintenance and degeneration. Cell Mol Life Sci *59*, 1851-1871.

Ransohoff, R.M., and Brown, M.A. (2012). Innate immunity in the central nervous system. J Clin Invest *122*, 1164-1171.

Ransom, B.R., Butt, A.M., and Black, J.A. (1991). Ultrastructural identification of HRP-injected oligodendrocytes in the intact rat optic nerve. Glia *4*, 37-45.

Readhead, C., Schneider, A., Griffiths, I., and Nave, K.A. (1994). Premature arrest of myelin formation in transgenic mice with increased proteolipid protein gene dosage. Neuron *12*, 583-595.

Reynolds, E.S. (1963). The use of lead citrate at high pH as an electron-opaque stain in electron microscopy. The Journal of cell biology *17*, 208-212.

Rosenbluth, J. (1980). Central myelin in the mouse mutant shiverer. The Journal of comparative neurology *194*, 639-648.

Rosenbluth, J., Nave, K.A., Mierzwa, A., and Schiff, R. (2006). Subtle myelin defects in PLP-null mice. Glia *54*, 172-182.

Roth, J., Bendayan, M., and Orci, L. (1978). Ultrastructural localization of intracellular antigens by the use of protein A-gold complex. The journal of histochemistry and cytochemistry : official journal of the Histochemistry Society *26*, 1074-1081.

Rowitch, D.H., and Kriegstein, A.R. (2010). Developmental genetics of vertebrate glial–cell specification. Nature *468*, 214.

Saher, G., Rudolphi, F., Corthals, K., Ruhwedel, T., Schmidt, K.F., Lowel, S., Dibaj, P., Barrette, B., Mobius, W., and Nave, K.A. (2012). Therapy of Pelizaeus-Merzbacher disease in mice by feeding a cholesterol-enriched diet. Nat Med *18*, 1130-1135.

Saiki, R.K., Gelfand, D.H., Stoffel, S., Scharf, S.J., Higuchi, R., Horn, G.T., Mullis, K.B., and Erlich, H.A. (1988). Primer-directed enzymatic amplification of DNA with a thermostable DNA polymerase. Science *239*, 487-491.

Salinas, S., Proukakis, C., Crosby, A., and Warner, T.T. (2008). Hereditary spastic paraplegia: clinical features and pathogenetic mechanisms. The Lancet Neurology *7*, 1127-1138.

Sampaio-Baptista, C., Khrapitchev, A.A., Foxley, S., Schlagheck, T., Scholz, J., Jbabdi, S., DeLuca, G.C., Miller, K.L., Taylor, A., Thomas, N.*, et al.* (2013). Motor skill learning induces changes in white matter microstructure and myelination. J Neurosci *33*, 19499-19503.

References

Sarikhani, M., Mishra, S., Maity, S., Kotyada, C., Wolfgeher, D., Gupta, M.P., Singh, M., and Sundaresan, N.R. (2018). SIRT2 deacetylase regulates the activity of GSK3 isoforms independent of inhibitory phosphorylation. eLife *7*.

Sarret, C., Combes, P., Micheau, P., Gelot, A., Boespflug-Tanguy, O., and Vaurs-Barriere, C. (2010). Novel neuronal proteolipid protein isoforms encoded by the human myelin proteolipid protein 1 gene. Neuroscience *166*, 522-538.

Sasaki, A. (2016). Microglia and brain macrophages: An update. Neuropathology : official journal of the Japanese Society of Neuropathology.

Saugier-Veber, P., Munnich, A., Bonneau, D., Rozet, J.M., Le Merrer, M., Gil, R., and Boespflug-Tanguy, O. (1994). X-linked spastic paraplegia and Pelizaeus-Merzbacher disease are allelic disorders at the proteolipid protein locus. Nat Genet *6*, 257-262.

Schneider, A., Montague, P., Griffiths, I., Fanarraga, M., Kennedy, P., Brophy, P., and Nave, K.A. (1992). Uncoupling of hypomyelination and glial cell death by a mutation in the proteolipid protein gene. Nature *358*, 758-761.

Scholz, J., Klein, M.C., Behrens, T.E., and Johansen-Berg, H. (2009). Training induces changes in white-matter architecture. Nat Neurosci *12*, 1370-1371.

Schwab, M.H., Druffel-Augustin, S., Gass, P., Jung, M., Klugmann, M., Bartholomae, A., Rossner, M.J., and Nave, K.A. (1998). Neuronal basic helix-loop-helix proteins (NEX, neuroD, NDRF): spatiotemporal expression and targeted disruption of the NEX gene in transgenic mice. J Neurosci *18*, 1408-1418.

Seitelberger, F. (1995). Neuropathology and genetics of Pelizaeus-Merzbacher disease. Brain pathology *5*, 267-273.

Simons, M., Kramer, E.M., Macchi, P., Rathke-Hartlieb, S., Trotter, J., Nave, K.A., and Schulz, J.B. (2002). Overexpression of the myelin proteolipid protein leads to accumulation of cholesterol and proteolipid protein in endosomes/lysosomes: implications for Pelizaeus-Merzbacher disease. The Journal of cell biology *157*, 327-336.

Simons, M., Kramer, E.M., Thiele, C., Stoffel, W., and Trotter, J. (2000). Assembly of myelin by association of proteolipid protein with cholesterol- and galactosylceramide-rich membrane domains. The Journal of cell biology *151*, 143-154.

Skripuletz, T., Hackstette, D., Bauer, K., Gudi, V., Pul, R., Voss, E., Berger, K., Kipp, M., Baumgartner, W., and Stangel, M. (2013). Astrocytes regulate myelin clearance through recruitment of microglia during cuprizone-induced demyelination. Brain *136*, 147-167.

Slot, J.W., and Geuze, H.J. (1985). A new method of preparing gold probes for multiple-labeling cytochemistry. European journal of cell biology *38*, 87-93.

Smith, M.E. (1968). The turnover of myelin in the adult rat. Biochim Biophys Acta *164*, 285-293.

Snaidero, N., Mobius, W., Czopka, T., Hekking, L.H., Mathisen, C., Verkleij, D., Goebbels, S., Edgar, J., Merkler, D., Lyons, D.A.*, et al.* (2014). Myelin membrane wrapping of CNS axons by PI(3,4,5)P3-dependent polarized growth at the inner tongue. Cell *156*, 277-290.

Snaidero, N., and Simons, M. (2017). The logistics of myelin biogenesis in the central nervous system. Glia *65*, 1021-1031.

Snaidero, N., Velte, C., Myllykoski, M., Raasakka, A., Ignatev, A., Werner, H.B., Erwig, M.S., Mobius, W., Kursula, P., Nave, K.A.*, et al.* (2017). Antagonistic Functions of MBP and CNP Establish Cytosolic Channels in CNS Myelin. Cell reports *18*, 314-323.

Snider, N.T., Leonard, J.M., Kwan, R., Griggs, N.W., Rui, L., and Omary, M.B. (2013). Glucose and SIRT2 reciprocally mediate the regulation of keratin 8 by lysine acetylation. The Journal of cell biology *200*, 241-247.

Sobottka, B., Harrer, M.D., Ziegler, U., Fischer, K., Wiendl, H., Hunig, T., Becher, B., and Goebels, N. (2009). Collateral bystander damage by myelin-directed CD8+ T cells causes axonal loss. The American journal of pathology *175*, 1160-1166.

Subramaniam, S.R., and Federoff, H.J. (2017). Targeting Microglial Activation States as a Therapeutic Avenue in Parkinson's Disease. Frontiers in aging neuroscience *9*, 176.

Tasdemir-Yilmaz, O.E., and Freeman, M.R. (2014). Astrocytes engage unique molecular programs to engulf pruned neuronal debris from distinct subsets of neurons. Genes & development *28*, 20-33.

Tokuyasu, K.T. (1973). A technique for ultracryotomy of cell suspensions and tissues. The Journal of cell biology *57*, 551-565.

Towbin, H., Staehelin, T., and Gordon, J. (1979). Electrophoretic transfer of proteins from polyacrylamide gels to nitrocellulose sheets: procedure and some applications. Proc Natl Acad Sci U S A *76*, 4350-4354.

Toyama, B.H., Savas, J.N., Park, S.K., Harris, M.S., Ingolia, N.T., Yates, J.R., 3rd, and Hetzer, M.W. (2013). Identification of long-lived proteins reveals exceptional stability of essential cellular structures. Cell *154*, 971-982.

Trevisiol, A., Saab, A.S., Winkler, U., Marx, G., Imamura, H., Mobius, W., Kusch, K., Nave, K.A., and Hirrlinger, J. (2017). Monitoring ATP dynamics in electrically active white matter tracts. eLife *6*.

Tripathi, R.B., Jackiewicz, M., McKenzie, I.A., Kougioumtzidou, E., Grist, M., and Richardson, W.D. (2017). Remarkable Stability of Myelinating Oligodendrocytes in Mice. Cell reports *21*, 316-323.

Tuason, M.C., Rastikerdar, A., Kuhlmann, T., Goujet-Zalc, C., Zalc, B., Dib, S., Friedman, H., and Peterson, A. (2008). Separate proteolipid protein/DM20 enhancers serve different lineages and stages of development. J Neurosci *28*, 6895-6903.

Vaquero, A., Scher, M.B., Lee, D.H., Sutton, A., Cheng, H.L., Alt, F.W., Serrano, L., Sternglanz, R., and Reinberg, D. (2006). SirT2 is a histone deacetylase with preference for histone H4 Lys 16 during mitosis. Genes & development *20*, 1256-1261.

von Bartheld, C.S., Bahney, J., and Herculano-Houzel, S. (2016). The search for true numbers of neurons and glial cells in the human brain: A review of 150 years of cell counting. The Journal of comparative neurology *524*, 3865-3895.

Vooijs, M., Jonkers, J., and Berns, A. (2001). A highly efficient ligand-regulated Cre recombinase mouse line shows that LoxP recombination is position dependent. EMBO reports *2*, 292-297.

Waisman, A., Liblau, R.S., and Becher, B. (2015). Innate and adaptive immune responses in the CNS. The Lancet Neurology *14*, 945-955.

Wang, F., Nguyen, M., Qin, F.X., and Tong, Q. (2007). SIRT2 deacetylates FOXO3a in response to oxidative stress and caloric restriction. Aging cell *6*, 505-514.

Wang, F., and Tong, Q. (2009). SIRT2 suppresses adipocyte differentiation by deacetylating FOXO1 and enhancing FOXO1's repressive interaction with PPARgamma. Molecular biology of the cell *20*, 801-808.

References

Waxman, S.G. (1980). Determinants of conduction velocity in myelinated nerve fibers. Muscle & nerve *3*, 141-150.

Weil, M.T., Mobius, W., Winkler, A., Ruhwedel, T., Wrzos, C., Romanelli, E., Bennett, J.L., Enz, L., Goebels, N., Nave, K.A., *et al.* (2016). Loss of Myelin Basic Protein Function Triggers Myelin Breakdown in Models of Demyelinating Diseases. Cell reports *16*, 314-322.

Weimbs, T., and Stoffel, W. (1992). Proteolipid protein (PLP) of CNS myelin: positions of free, disulfide-bonded, and fatty acid thioester-linked cysteine residues and implications for the membrane topology of PLP. Biochemistry *31*, 12289-12296.

Werner, H.B., Kramer-Albers, E.M., Strenzke, N., Saher, G., Tenzer, S., Ohno-Iwashita, Y., De Monasterio-Schrader, P., Mobius, W., Moser, T., Griffiths, I.R*., et al.* (2013). A critical role for the cholesterol-associated proteolipids PLP and M6B in myelination of the central nervous system. Glia *61*, 567-586.

Werner, H.B., Kuhlmann, K., Shen, S., Uecker, M., Schardt, A., Dimova, K., Orfaniotou, F., Dhaunchak, A., Brinkmann, B.G., Möbius, W*., et al.* (2007). Proteolipid protein is required for transport of sirtuin 2 into CNS myelin. J Neurosci *27*, 7717-7730.

Wes, P.D., Holtman, I.R., Boddeke, E.W., Moller, T., and Eggen, B.J. (2016). Next generation transcriptomics and genomics elucidate biological complexity of microglia in health and disease. Glia *64*, 197-213.

Woodward, K.J. (2008). The molecular and cellular defects underlying Pelizaeus-Merzbacher disease. Expert reviews in molecular medicine *10*, e14.

Wu, S.X., Goebbels, S., Nakamura, K., Nakamura, K., Kometani, K., Minato, N., Kaneko, T., Nave, K.A., and Tamamaki, N. (2005). Pyramidal neurons of upper cortical layers generated by NEX-positive progenitor cells in the subventricular zone. Proc Natl Acad Sci U S A *102*, 17172-17177.

Yang, Y.H., Chen, Y.H., Zhang, C.Y., Nimmakayalu, M.A., Ward, D.C., and Weissman, S. (2000). Cloning and characterization of two mouse genes with homology to the yeast Sir2 gene. Genomics *69*, 355-369.

Yeung, M.S., Zdunek, S., Bergmann, O., Bernard, S., Salehpour, M., Alkass, K., Perl, S., Tisdale, J., Possnert, G., Brundin, L*., et al.* (2014). Dynamics of oligodendrocyte generation and myelination in the human brain. Cell *159*, 766-774.

Yin, X., Kidd, G.J., Ohno, N., Perkins, G.A., Ellisman, M.H., Bastian, C., Brunet, S., Baltan, S., and Trapp, B.D. (2016). Proteolipid protein-deficient myelin promotes axonal mitochondrial dysfunction via altered metabolic coupling. The Journal of cell biology *215*, 531-542.

Yool, D.A., Klugmann, M., McLaughlin, M., Vouyiouklis, D.A., Dimou, L., Barrie, J.A., McCulloch, M.C., Nave, K.A., and Griffiths, I.R. (2001). Myelin proteolipid proteins promote the interaction of oligodendrocytes and axons. J Neurosci Res *63*, 151-164.

Young, E.A., Fowler, C.D., Kidd, G.J., Chang, A., Rudick, R., Fisher, E., and Trapp, B.D. (2008). Imaging correlates of decreased axonal Na+/K+ ATPase in chronic multiple sclerosis lesions. Annals of neurology *63*, 428-435.

Young, K.M., Psachoulia, K., Tripathi, R.B., Dunn, S.J., Cossell, L., Attwell, D., Tohyama, K., and Richardson, W.D. (2013). Oligodendrocyte dynamics in the healthy adult CNS: evidence for myelin remodeling. Neuron *77*, 873-885.

Yu, L.H., Morimura, T., Numata, Y., Yamamoto, R., Inoue, N., Antalfy, B., Goto, Y., Deguchi, K., Osaka, H., and Inoue, K. (2012). Effect of curcumin in a mouse model of Pelizaeus-Merzbacher disease. Molecular genetics and metabolism *106*, 108-114.

Zeis, T., Enz, L., and Schaeren-Wiemers, N. (2016). The immunomodulatory oligodendrocyte. Brain research *1641*, 139-148.

Zeisel, A., Munoz-Manchado, A.B., Codeluppi, S., Lonnerberg, P., La Manno, G., Jureus, A., Marques, S., Munguba, H., He, L., Betsholtz, C*., et al.* (2015). Brain structure. Cell types in the mouse cortex and hippocampus revealed by single-cell RNA-seq. Science *347*, 1138-1142.

Zhang, Y., Chen, K., Sloan, S.A., Bennett, M.L., Scholze, A.R., O'Keeffe, S., Phatnani, H.P., Guarnieri, P., Caneda, C., Ruderisch, N*., et al.* (2014). An RNA-sequencing transcriptome and splicing database of glia, neurons, and vascular cells of the cerebral cortex. J Neurosci *34*, 11929-11947.

Zhu, H., Zhao, L., Wang, E., Dimova, N., Liu, G., Feng, Y., and Cambi, F. (2012). The QKI-PLP pathway controls SIRT2 abundance in CNS myelin. Glia *60*, 69-82.

Zuchero, J.B., and Barres, B.A. (2015). Glia in mammalian development and disease. Development *142*, 3805-3809.

Publications

Lüders, K.A., Patzig, J., Simons, M., Nave, K.A., and Werner, H.B. (2017). Genetic dissection of oligodendroglial and neuronal *Plp1* function in a novel mouse model of spastic parapegia type 2. Glia *65*, 1762-1776.

Patzig, J., Kusch, K., Fledrich, R., Eichel, M.A., **Lüders, K.A.**, Möbius, W., Sereda, M.W., Nave, K.A., Martini, R., and Werner, H.B. (2016). Proteolipid protein modulates preservation of peripheral axons and premature death when myelin protein zero is lacking. Glia *64*, 155-174.

Kunst, M., Pförtner, R., **Aschenbrenner, K.**, and Heinrich, R. (2011). Neurochemical architecture of the central complex related to its function in the control of grasshopper acoustic communication. PLoS One *6*, e25613.